



DEVELOPMENT OF A LASER PROBE FOR ELECTRON TEMPERATURE

H. Sadjian and D. A. Rogers
Environmental Sciences Laboratory
General Electric Company

April 1971

Approved for public release; distribution unlimited.

ARNOLD ENGINEERING DEVELOPMENT CENTER
AIR FORCE SYSTEMS COMMAND
ARNOLD AIR FORCE STATION, TENNESSEE

PROPERTY OF U S AIR FORCE
ALSO LIBRARY
F40600-71-C-0002

NOTICES

When U. S. Government drawings specifications, or other data are used for any purpose other than a definitely related Government procurement operation, the Government thereby incurs no responsibility nor any obligation whatsoever, and the fact that the Government may have formulated, furnished, or in any way supplied the said drawings, specifications, or other data, is not to be regarded by implication or otherwise, or in any manner licensing the holder or any other person or corporation, or conveying any rights or permission to manufacture, use, or sell any patented invention that may in any way be related thereto.

Qualified users may obtain copies of this report from the Defense Documentation Center.

References to named commercial products in this report are not to be considered in any sense as an endorsement of the product by the United States Air Force or the Government.

DEVELOPMENT OF A LASER
PROBE FOR ELECTRON TEMPERATURE

H. Sadjian and D. A. Rogers
Environmental Sciences Laboratory
General Electric Company

Approved for public release; distribution unlimited.

FOREWORD

The work reported herein was sponsored by the Arnold Engineering Development Center under Air Force Contract No. F40600-68-C-0003 entitled "The Development of a Laser Probe for Electron Temperature," Program Element 62201F, Project 8952, Task 01.

The developmental efforts and experimental evaluation of the laser probe were performed by the Environmental Sciences Laboratory, (previously Space Sciences Laboratory, MSD), Re-Entry and Environmental Systems Division of the General Electric Company.

The authors wish to acknowledge the very significant contributions and efforts of the following individuals: Mr. Benjamin Bellinger for the construction of the detector system and for operation of the free jet facility; Mr. Donald DeDominicis for the design of the detector system; Mr. George Grassò for the design of the mirror goniometer; Mr. Gennaro Catalano for development of the free jet facility; Mr. Mark Jaffe and Miss Betty Miller for programming and performing the numerical analyses to make the experimental data meaningful; Mr. Clarence J. Harris for providing the use of the shock tunnel facility and for his guidance in the interpretation of the shock tunnel data; Mr. Emmanuel Stelman for construction of the electronics portion of the detector; and Mr. Nick Diaconis, Manager of the Environmental Facilities Laboratory, without whose encouragement and support this work could not have been completed.

The reproducibles used in the reproduction of this report were supplied by the authors.

This technical report has been reviewed and is approved.

Marshall K. Kingery
Research and Development
Division
Directorate of Technology

Harry L. Maynard
Colonel, USAF
Director of Technology

ABSTRACT

2

Thomson scattering radiation has been measured in terms of electron concentration and temperature in a free jet facility and a shock tunnel using a 1/2 joule, Q-switched ruby laser. A detector system is described which attenuates the primary ruby wavelength by 10^5 , discriminates between orthogonal polarization states, analyzes the radiation spectrally and provides a measure of radiation background. The scattering volume was approximately $3 \times 10^{-4} \text{ cm}^3$ for the jet facility and approximately $2 \times 10^{-3} \text{ cm}^3$ for the shock tunnel. A temperature range of 3000 to 8000°K and an electron concentration range 5×10^{14} to $5 \times 10^{15} \text{ cm}^{-3}$ was measured. A unique method of measuring electron temperature is described using a passive system utilizing a retardation plate.

CONTENTS

<u>SECTION</u>	<u>PAGE</u>
I. Introduction	1
II. Detector System	2
A. General Description	2
B. Mirror System and Retardation Plate	4
C. Calibration of Detector System	4
D. Electronics and Read Out	6
III. Thomson Scattering Experiments	17
A. Air Arc Experiments	17
B. Shock Tunnel Experiments	23
Appendix I. Calculation of Working Equations	45
Appendix II. Engineering Design Data For Detector	47
Appendix III. Computer Program Listing and Results	61
Appendix IV. Error Statement	72
Appendix V. Reproduction of Paper by C. J. Harris	75
References	89

LIST OF ILLUSTRATIONS

<u>FIG</u>		<u>PAGE</u>
1	Optical Schematic of Detector System	9
2	Spectrograms Taken Through Detector System	10
3	Spectrogram Taken Through (Sine) ² Channel	11
4	Spectral Transmission Curve for (Sine) ² Channel	12
5	Spectral Transmission Curve for (Cosine) ² Channel	13
6	Calibration Curve for Electron Temperature	14
7	Block Diagram of Signal Handling System	15
8	Laser and Electronic Circuit Characteristics	16
9	Gerdien Free Jet Arc	28
10	Schematic Tandem Gerdien Arc Heater	29
11	Schematic of Gerdien Free Jet	30
12, 13, 14	Typical Oscillograms From Arc Jet Runs	31
15	Oscillogram of Arc Background	32
16	Portion of Fastax Movies of Arc Jet	33
	TABLE I	34
17	MHD Augmented High Density Shock Tunnel	35
18	Experimental Arrangement For Probe	36
19	Photograph of Laser Probe Experimental Set-Up	37

<u>FIG.</u>		<u>PAGE</u>
20	Photograph of Laser Probe Experimental Set-Up	38
21, 22, 23	Typical Oscillograms During Tunnel Pre-Test	39
24	Calibration Curve For Tunnel Electron Temperature	40
25	Calibration Curve For Tunnel Ne	41
26, 27, 28	Oscillograms From Tunnel Test #304	42
29, 30, 31	Oscillograms From Tunnel Test #305	43

SECTION I

INTRODUCTION

The present work is an extension of the laser probe program initiated under an AEDC contract No. A. F. 40(600)-1147. In the previous work a detector system was built which permitted the determination of electron density within a small scattering volume. The desirability of measuring both electron concentration and temperature simultaneously provided the motivation for the present work.

The original intent of the program was to measure, during a laser pulse, the radiated line shape. This was to be accomplished by electro-optical tuning through a Fabry-Perot interferometer; however, our early experiments indicated that this approach was not feasible and a suitable alternate scheme was required. The scheme finally used which best fit the goals of the contract was a passive system in which line shape, reflecting electron temperature, could be obtained by inference from the ratio of two separate portions of the line shape. In addition, the detector system had to retain the attenuation characteristics of the primary wavelength of the original detector and discriminate between the radiation background and scattered laser radiation.

The detector system was evaluated in both an arc environment and a shock tunnel environment in which simultaneous measurements of electron temperature and concentration were made. Although the arc results could not be used to validate the probe due to high impurity levels, the shock tunnel measurements gave good agreement with equilibrium theory. Unfortunately enough tunnel measurements could not be made, due to funding limitation, to build up a statistical backlog of measurements for proper evaluation.

SECTION II

DETECTOR SYSTEM

A. General Description

The detector system is basically a differential photometer which discriminates the incoming radiation in terms of polarization and wavelength and at the same time attenuates the primary wavelength to about 5 orders of magnitude. The optical diagram is depicted in FIG 1. The imaging lens forms a 1:1 stigmatic image of the scattering volume on the entrance slit of the detector. The slit is a commercial Hilger bilateral variable slit housing with shutter and Hartmann diaphragm. The collimating lens in the detector housing collimates the radiation onto the pair of spectral mirrors set at about 70° to the radiation. The spectral mirrors are commercially available interference filters without blocking filters with a transmission of about 80% and a band pass of about 5 Å centered at 6943 Å. The spectral mirrors are mounted in a precision goniometer (see Appendix for details) which can be controlled by a knob from outside the detector housing. The primary wavelength (6943 Å) is attenuated by the spectral mirrors (10 traversals between the mirrors) by about 5 orders of magnitude while passing radiation 5 Å away from 6943 Å with a high optical efficiency ($\sim 75\%$). The field lens serves to image the entrance slit onto the photomultipliers and to collect all the light coming from the mirrors (in passing through the spectral mirrors the beam expands to about 1 inch diameter). A broad band filter ~ 100 Å and 80% transmission limits the radiation passed by the system. The Wallaston prism (1 inch diameter, $22\frac{1}{2}^\circ$ divergence) separates the incoming radiation into two polarized beams. The horizontal beam (parallel to the plane of observation) is used to measure the background radiation by photomultiplier #3 (PM #3) and does not contain the scattered radiation due to the laser light. The vertical polarization containing $1/2$ of the plasma background and the Thomson scattered radiation passes through a 100λ (6943) retardation plate followed by a second Wollaston prism. The effect of the retardation plate and second Wollaston is to wavelength modulate the incoming radiation as $(\sin)^2$ and $(\cos)^2$ which falls on PM #2 and PM #1 respectively. All the lens surfaces were anti-reflection coated to give an overall optical efficiency of 70%.

In operation, the detector attenuates the primary wavelength, passes approximately 100 Å of the radiation, presents one-half of the radiation to PM #3 not containing Thomson scattered light, the remaining portion being modulated as $(\cos)^2$ and $(\sin)^2$ and presented to PM's #1 and #2 respectively. For the purpose of determining electron concentration and tempera-

ture, the sum of PM #1 and PM #2 is a measure of the concentration and the ratio of PM #1 and PM #2 is a measure of the electron temperature. PM #3 is used to measure the magnitude of the plasma background which can be subtracted from PM's #1 and #2.

To facilitate the alignment of the detector system with the scattering volume, a He/Ne gas laser was built into the detector assembly. The plug-in mirror in front of the field lens is used to direct the laser beam back through the spectral mirrors, collimator and entrance slit where it is focused in space by the imaging lens.

B. Mirror System and Retardation Plate

The spectral mirrors ($1/2'' \times 2''$) are regular interference filters without the blocking filters. These are mounted in a precision goniometer which is controlled by a knob outside the detector. The mirrors were designed to give minimum reflectivity (maximum transmission) for 6943 Å at about 70° angle of incidence. The mirrors were tuned initially by passing light from a tungsten lamp through the mirror system and observing the resultant radiation through a 2 meter B&L spectrogram. The angle was adjusted until there was maximum attenuation for 6943 Å. In addition, the mirror holders have adjustments for separation between mirrors to control the number of reflections between the mirrors. In the final configuration the separation was about 1" giving 10 reflections between the mirror pair. The spectral sensitivity of the mirror pair due to finite size of the entrance slit is about 262 Å/radian. Assuming a slit width of 50 μ (used in these experiments) and a collimator focal length of 16 mm amounts to $\pm 1.5 \times 10^{-3}$ radians or ± 0.4 Å. This corresponds to the approximate line width of the burst mode of the laser.

In addition to tuning the spectral mirrors, the retardation plate was tuned in a similar manner. The retardation plate is a quartz birefringence plate approximately 0.75 cm thick and 1.5 cm diameter. Using a tungsten lamp the retardation plate was rotated until nulls were obtained visually through the spectrograph. Observations were made on both the $(\cosine)^2$ channel and the $(\sin)^2$ channel. FIG. 2 shows 3 spectrograms representing the resultant radiation on the plane of the PM's. The top spectrogram shows the resultant radiation after passing through the spectral mirrors. The second shows the wavelength modulation in the $(\cosine)^2$ channel and the third the $(\sin)^2$ channel. The lines are due to a reference neon lamp. These spectrograms were taken without the broad band filter in place. FIG 3 is a spectrogram of the resultant radiation through the $(\sin)^2$ channel with the filter in place.

C. Calibration of Detector System

In order to successfully use the detector system it was necessary to provide 5 separate calibrations as follows:

- (1) attenuation of 6943 A
- (2) Transmission curves of the three separate channels
- (3) Absolute sensitivities of the three photomultipliers
- (4) Overall efficiency of the three channels
- (5) Response of the detector system to differing line shapes corresponding to varying electron temperatures

The attenuation measurements were performed as follows:

The laser, operating in the burst mode, was directed to a glass plate at an angle of incidence of about 15° . The light is reflected into the detector system with the detector lens focused on the glass plate. The energy incident on the glass plate and reflected from the glass plate was measured with the Lear-Siegler energy monitor. Approximately 50 millijoules was directed into the detector system. The spectral mirrors were adjusted to obtain minimum response using successive firings of the laser. Due to the inability to operate the laser in the Q-switched mode it was anticipated that the attenuation would not be near theoretical ($\sim 10^{-7}$) due to the excessive line width ($\sim .3$ to $.4\text{A}$). Measurements were made varying the slit width of the detector system to obtain a measure of the line width. At 20μ , the attenuation is less than 10^{-5} and decreases with increasing slit width to about 10^{-3} . To test the hypothesis that the large line width is reducing the attenuation, several measurements were made with the laser operating near threshold (reduced line width). It is found that the attenuation coefficient increased by a factor of 10. In the final testing of the detector system (in an air arc) using a Q-switched laser the measured attenuation was less than 10^{-5} . It was also determined that due to scattering within the detector system, in spite of extensive baffling, is on the order of 10^{-6} . These tests were conducted during several hundred firings to obtain statistical sampling of the attenuation coefficient due to the changing line shape of each firing of the laser.

The second calibration was obtained with the Heath scanning monochromator purchased for this purpose. The detector system was focused on the exit slit of the monochromator which was fed with a tungsten ribbon lamp. The transmission curves (relative) was obtained for the three channels representing background light, \sin^2 modulated and \cos^2 modulated light. Again these tests were conducted several times to obtain a statistical average (FIGS 4 and 5).

The absolute sensitivities were obtained in the following manner. The internal mirror which normally directs the internal gas laser through the spectral mirrors to the external lens of the detector was reversed so that the laser beam is directed back to the photomultipliers. With one of the photomultipliers removed, the exit beam was measured with a calibrated EG&G lite-mike. A calibrated attenuator for 6328A (operating wavelength of the laser) was then placed in the optical path. The photomultiplier was then replaced and its current measured. It was not necessary to repeat this for the other photomultipliers as a relative calibration was made by replacing each tube in turn in the same channel slot with the detector system fed with a tungsten ribbon filament lamp. The absolute calibration for the three tubes resulted in the following.

$$\text{PM \#1 (cos}^2 \text{ channel)} = 5.40 \times 10^{15} \text{ } \phi/\text{cl @ 1200 volts}$$

$$\text{PM \#2 (sin}^2 \text{ channel)} = 6.66 \times 10^{15} \text{ } \phi/\text{cl @ 1200 volts}$$

$$\text{PM \#3 (background channel)} = 2.29 \times 10^{16} \text{ } \phi/\text{cl @ 1200 volts}$$

where ϕ is photons at 6943 and cl is coulombs of charge. In addition, a relative calibration of the three tubes was made at 1000, 1100, 1250 and 1300 volts cathode supply.

In order to measure the overall efficiency of the three separate channels, a calibrated blackbody source operating at 900°C was used. With the blackbody source focused on the slit of the detector, the outputs of the three channels were obtained and translated into photons/sec-A. Using the relative transmission curves obtained previously, the curves were integrated (graphically) to obtain the integrated band pass for each channel with the results:

$$\text{Channel \#1} = 59\text{A}$$

$$\text{Channel \#2} = 45\text{A}$$

$$\text{Channel \#3} = 80.5\text{A}$$

Using these results, the apparent energy to the detector system was obtained and then ratioed to the measured outputs with the following results:

$$\text{Channel \#1} = 48.6\%$$

$$\text{Channel \#2} = 70.9\%$$

$$\text{Channel \#3} = 60.7\%$$

These percentages represent the peak of their respective transmission curves. The low figure of Channel #1 is due to the composite of the rising \cos^2 cycle and the declining slope due to the spectral mirrors. Experimentally, the sum of channels #1 and #2 equals #3 indicating very little overall loss of light. The overall efficiency (sum of all three channels) was measured at 61%. As the interference filter at the peak transmission of the system is about 80%, this indicates an overall efficiency of 75%. As the retardation plate and one lens is not coated in the system combined with the 10 reflections from the spectral mirrors, this figure is close to what is expected ($\sim 80\%$).

In order to determine the response of channels #1 and #2 to changing line shape (electron temperature) it was necessary to compute the theoretical profiles for equilibrium air conditions and integrate the theoretical profiles over the experimentally determined transmission curves to obtain the ratio response in terms of electron temperature. The method used for computation of the theoretical profiles was described in our previous report and will not be repeated here. For the air arc experiments the resultant calibration curve for electron temperature is shown in FIG 6. As indicated before, the electron concentration is determined by the sum of Channels #1 and #2 after subtraction of background. The method used will be described under the section on air arc experiments.

For the shock tunnel experiments where equilibrium cannot be assumed, it was necessary to compute the ratio of Channels #1 and #2 as function of T_e , α and N_e where α is the $1/KD$ with $K = \frac{4\pi}{\lambda} \sin \theta/2$ and D the Debye length (see previous report).

D. Electronics and Read Out

The signal data handling system design was based on the desire to provide maximum flexibility and to fully utilize the received scattered laser light signal. A block diagram of the data handling system is shown in FIG 7. The three photomultipliers are RCA Type 4526 tubes, selected for quantum efficiency of at least 7% at the ruby laser wavelength. PM's #1 and #2 receive the Thomson scattered laser light as well as any plasma background light which is passed by the detector optical system. PM #3 sees only background light and is used to provide a measurement of this background which can be used to subtract out the background component from the other PM outputs.

The gate generator is a tunnel diode junction transistor level detector which provides a constant amplitude gate output for a time about fifty nanoseconds longer than the duration of the laser pulse in order to allow for the electron transit time delay in the PM's. The input to the gate generator is provided by the Laser Energy Monitor whose silicon photodiode generates a signal each time the laser pulses. Emitter followers couple the gate to each of the gated integrators.

PM #1 and PM #2 outputs are each returned to ground through a fast recovery hot-carrier diode (Hewlett-Packard 5082-2800 series) and a fifty ohm resistor which shunt the integrating capacitor at the input to an FET amplifier. When the laser fires, a gate pulse is developed across the fifty ohm resistor to reverse bias the diode and divert the PM output into the integrating capacitor. This signal is amplified by about 30 db and coupled into an FET storage amplifier for presentation on the display oscilloscope. The storage amplifier is of a summing type such that the PM signals obtained during each laser pulse are totalized. The storage time constant is about ten milliseconds in order to minimize the decay between pulses. This circuit was necessitated by the nature of the laser, which multiple-pulsed even when Q-switched. The output signal for a typical multiple laser pulse is shown in FIG 8 which also shows the laser energy monitor output and resultant gate for a single pulse.

Unfortunately, while this data handling system is sound in principle and behaved well when tested using a steady background signal, it proved inadequate when subjected to the rapid fluctuations of intensity of the arc plasma in the facility used to evaluate the laser probe. These fluctuations prevented the establishment of a quiescent voltage level at the amplifier input and caused sufficient zero shift in the storage amplifier output to make meaningful measurements virtually impossible. While a solution to these problems is undoubtedly attainable by redesign of the integrator and use of a sample and hold circuit in place of the simple storage circuit, this was unnecessary for the purpose of this program. Problems with the laser led to the use of a different one which did not multiply Q-switch, thus eliminating the need for the summing storage circuit. Use of shorter coupling time constants in the amplifier minimized the effects of the arc fluctuations and allowed for direct display of the amplified PM output signal.

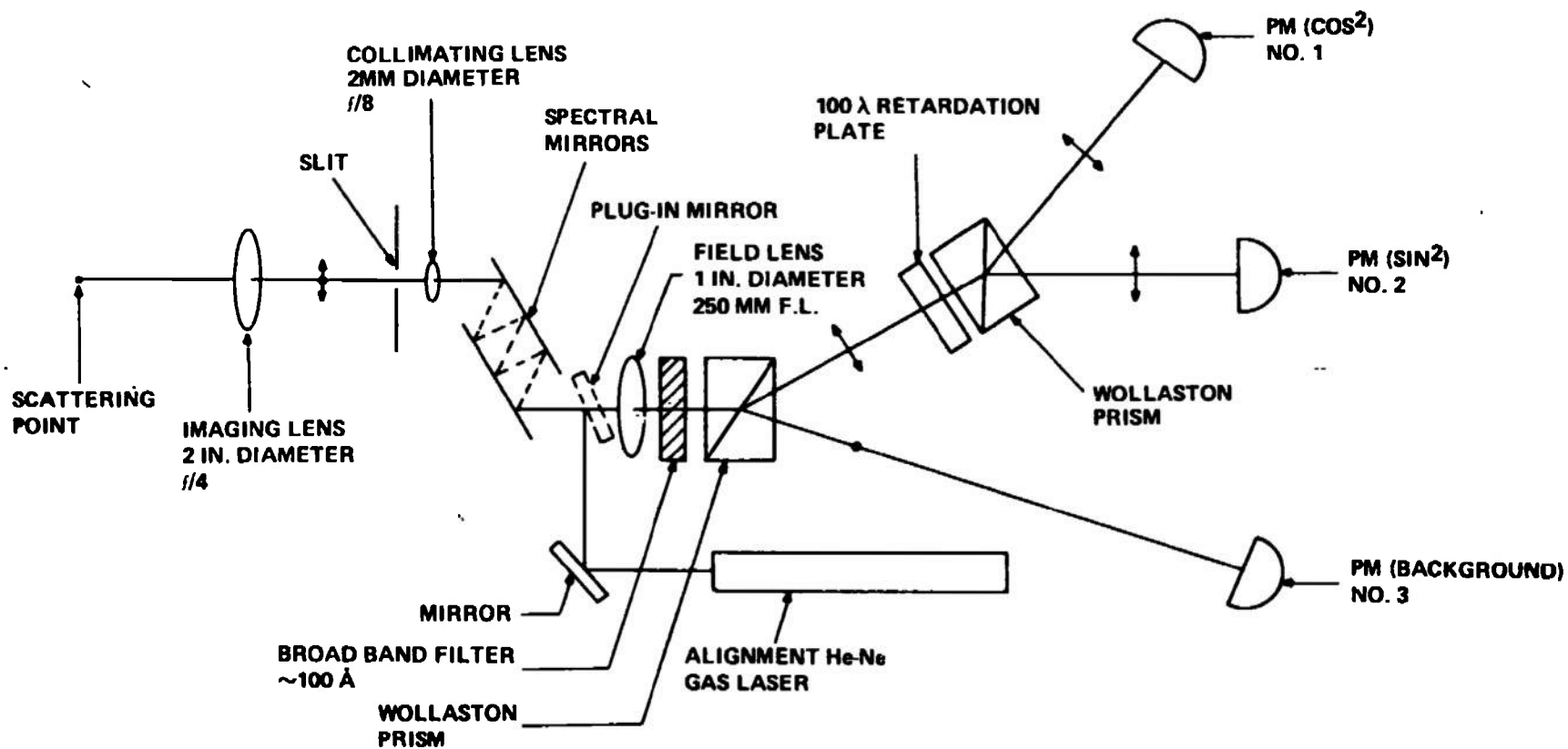


FIGURE 1. OPTICAL SCHEMATIC OF DETECTOR SYSTEM

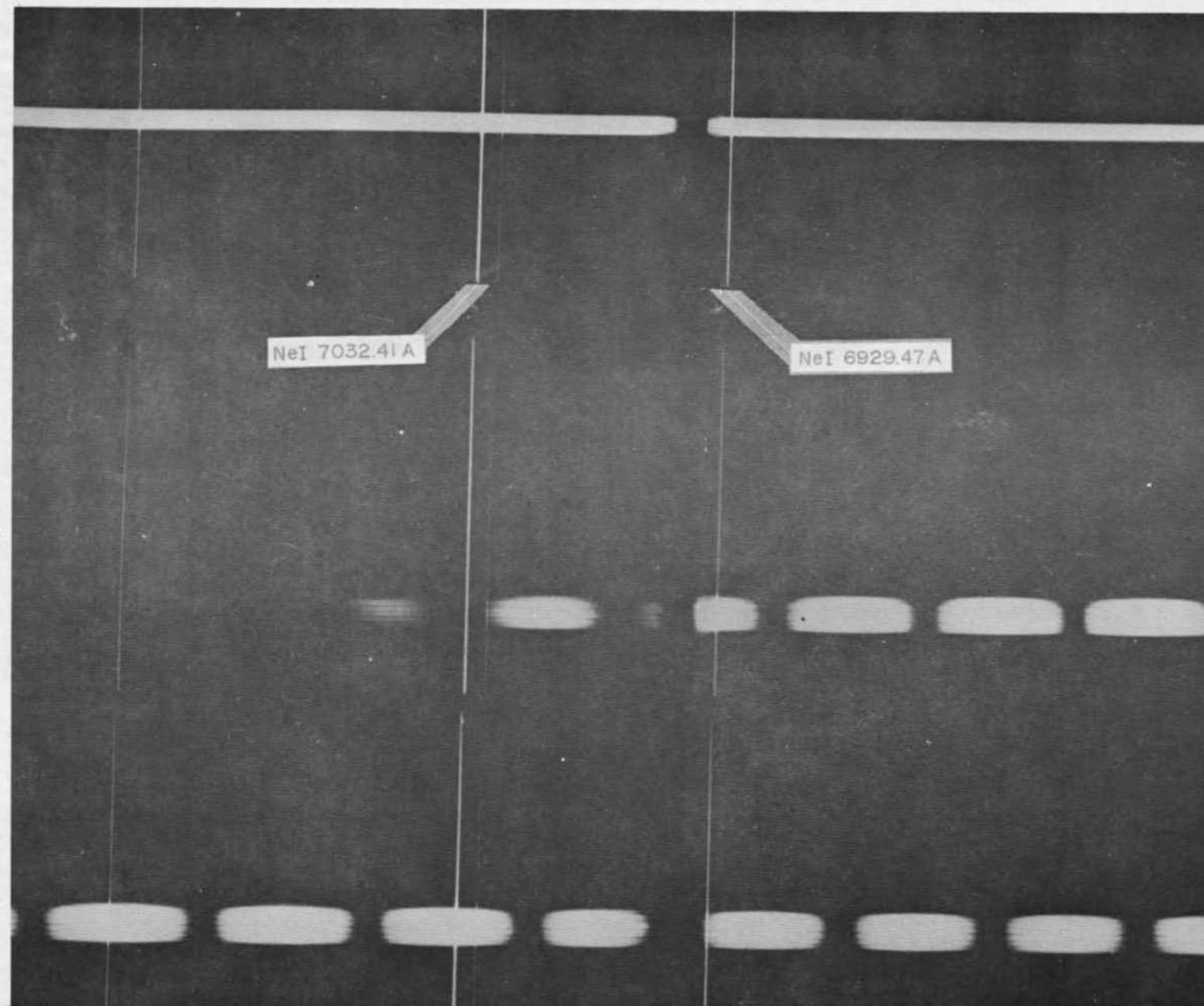


FIGURE 2. SPECTROGRAMS TAKEN THROUGH DETECTOR SYSTEM (SEE TEXT)

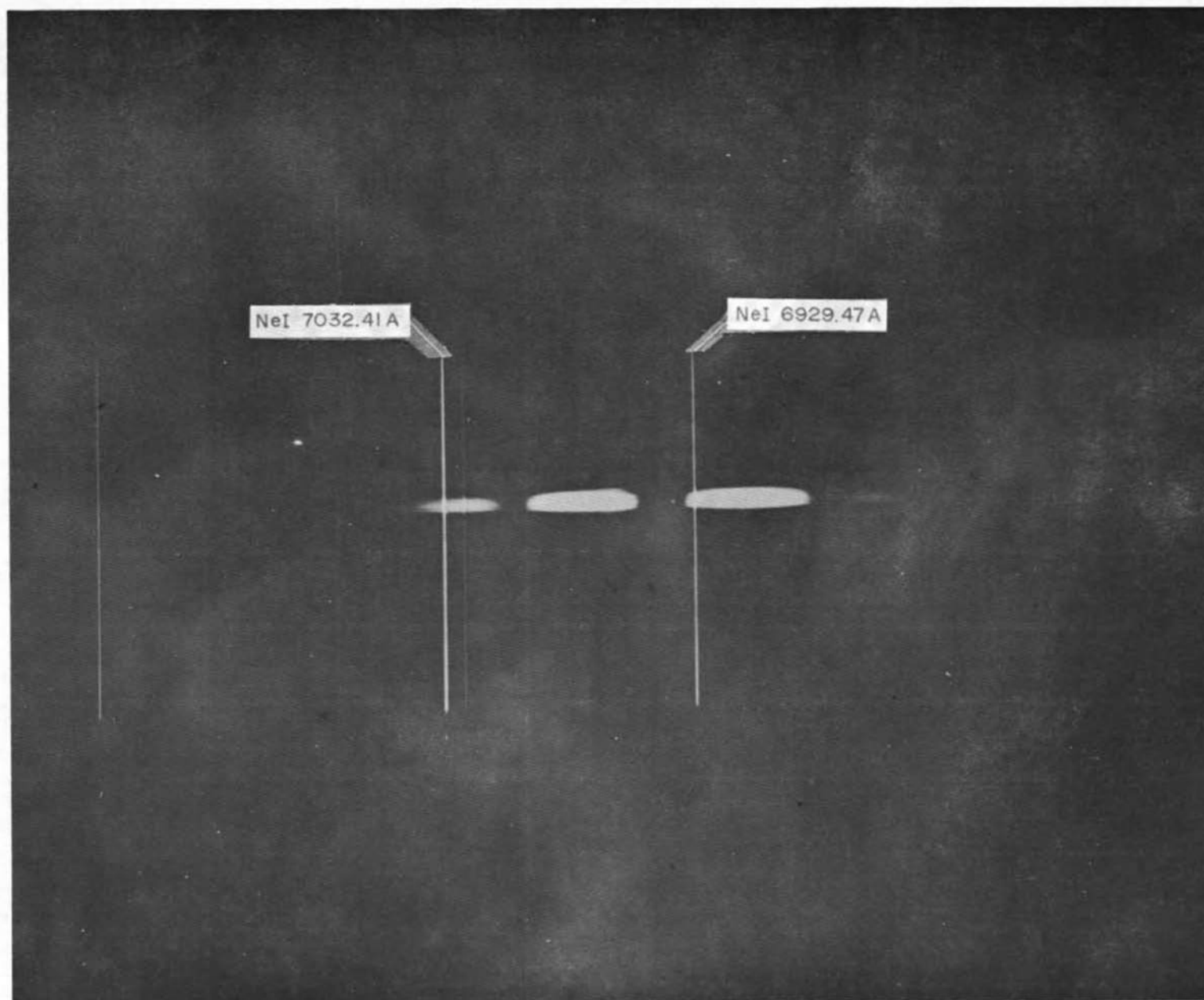


FIGURE 3. SPECTROGRAM TAKEN THROUGH $(\text{SINE})^2$ CHANNEL

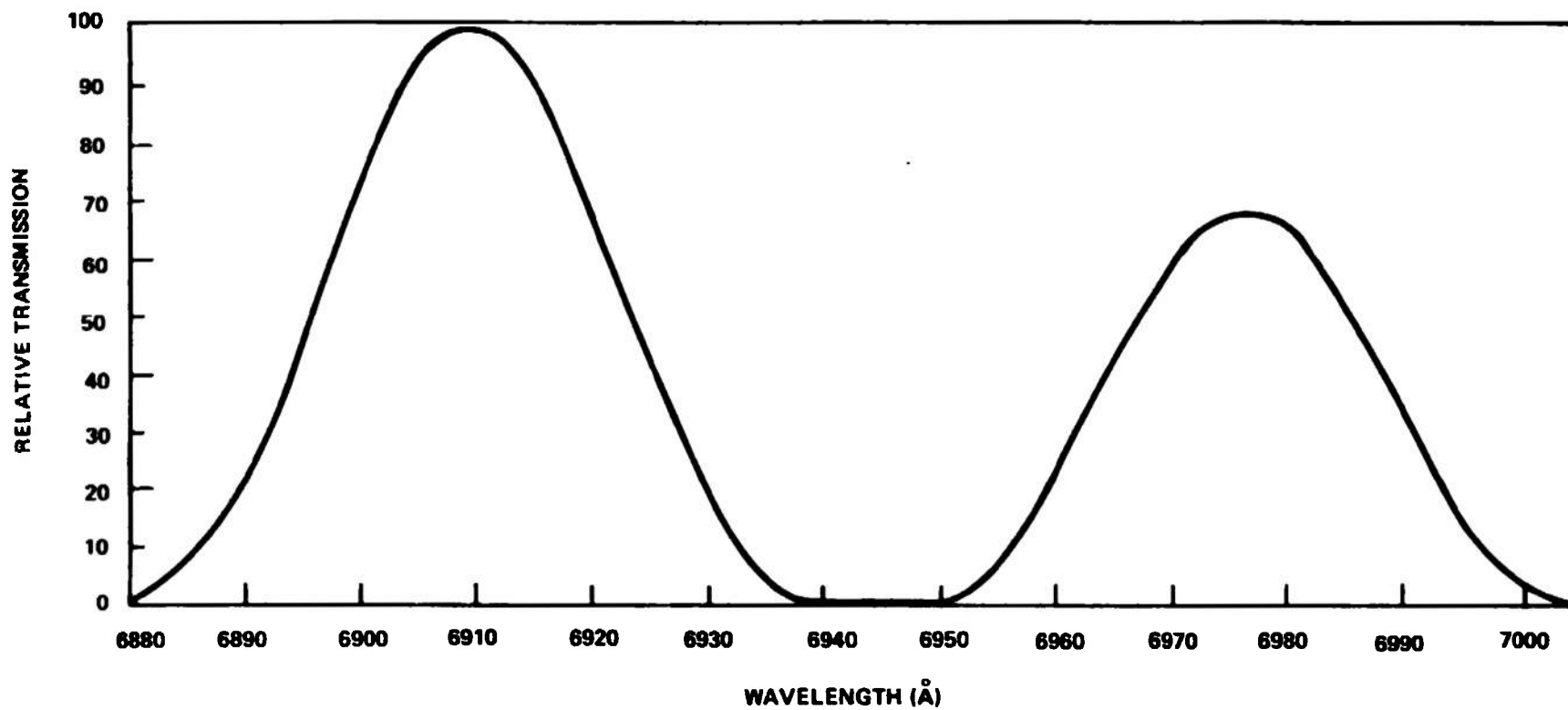


FIGURE 4. SPECTRAL TRANSMISSION CURVE FOR $(\text{SINE})^2$ CHANNEL

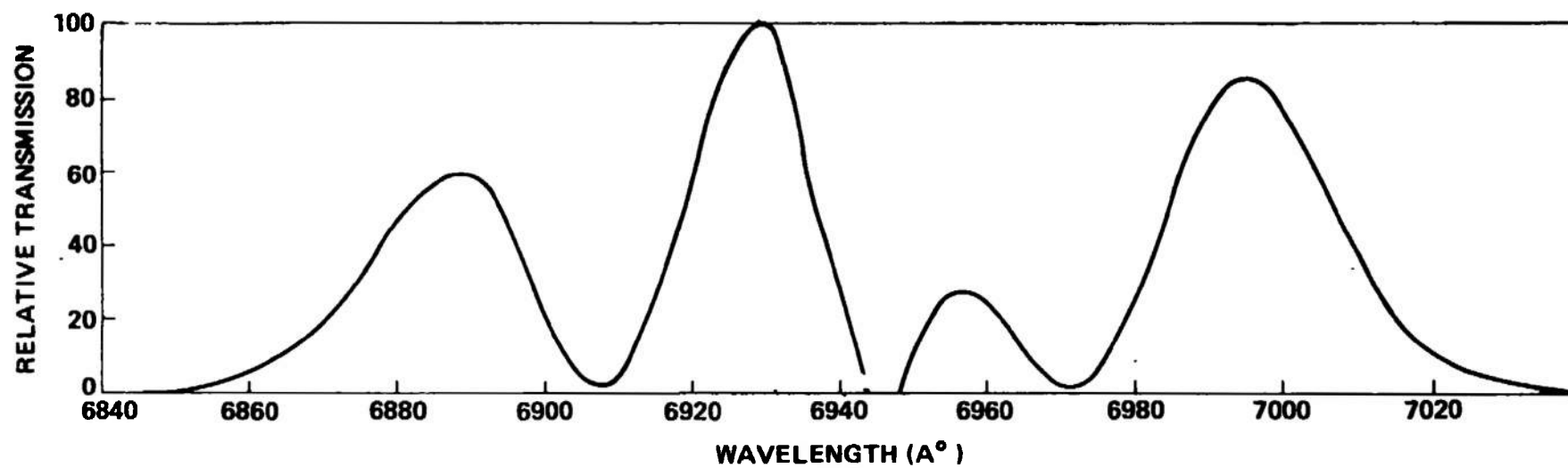


FIGURE 5. SPECTRAL TRANSMISSION CURVE FOR $(\cosine)^2$ CHANNEL

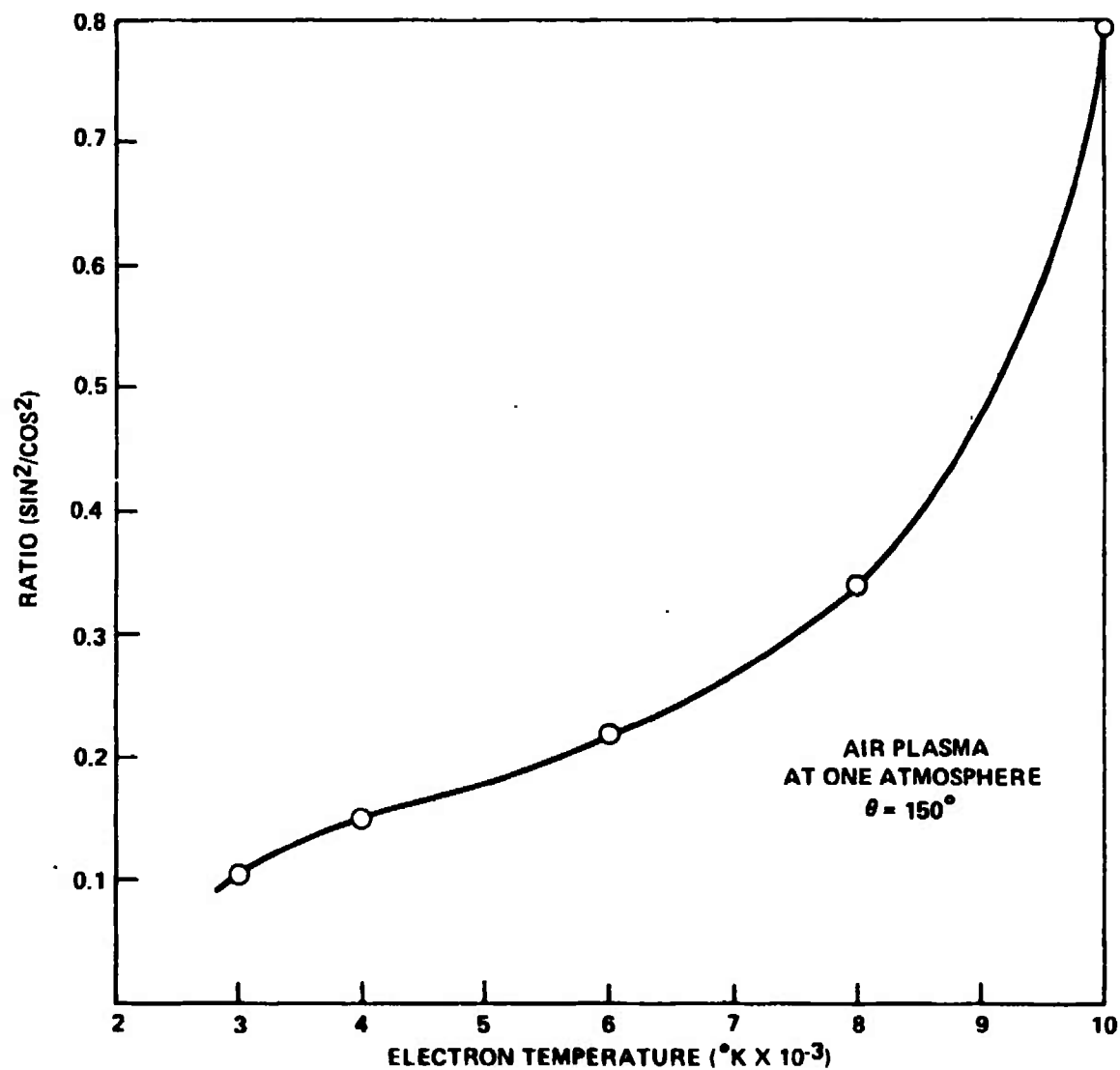


FIGURE 6. CALIBRATION CURVE FOR ELECTRON TEMPERATURE

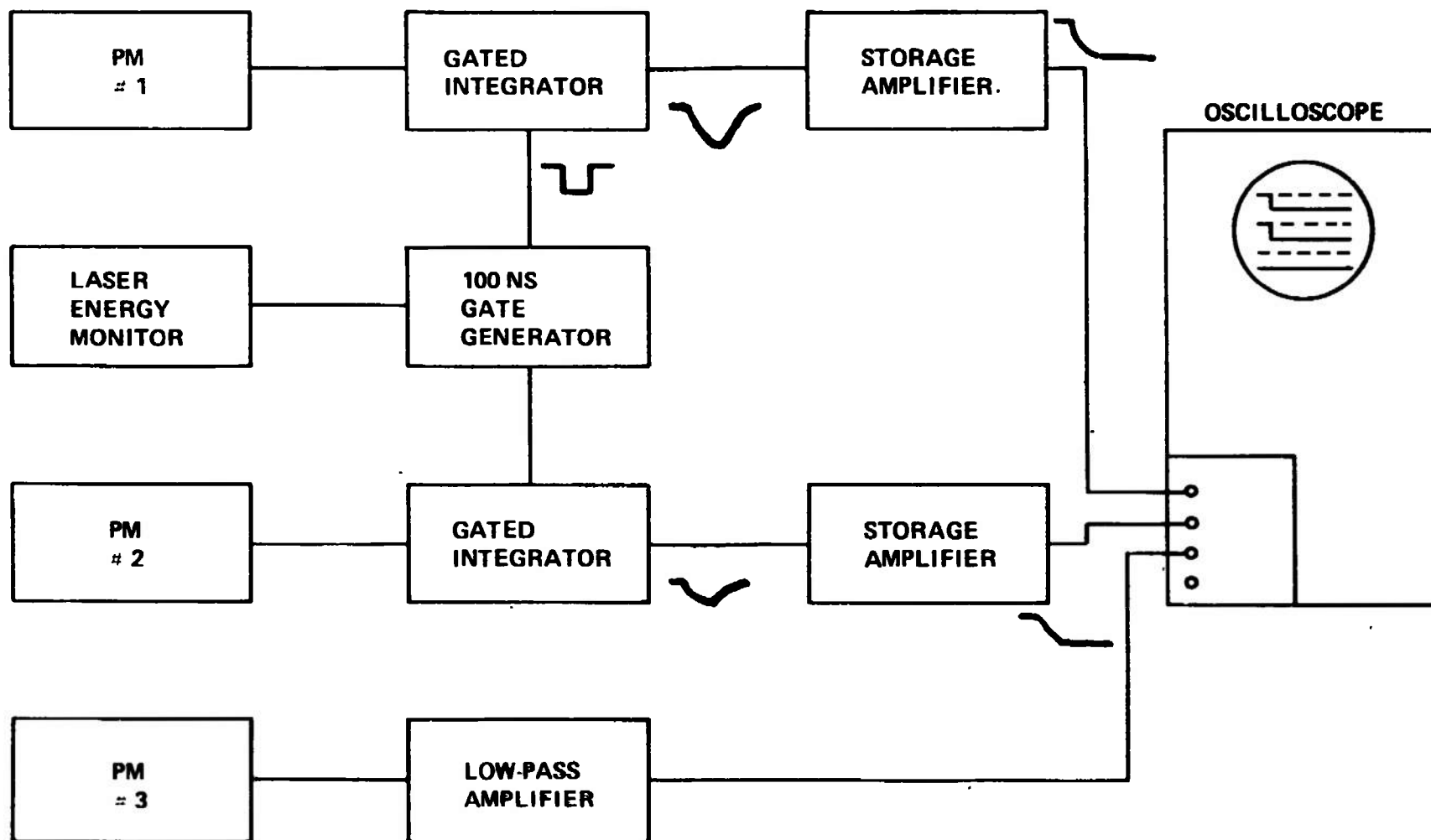
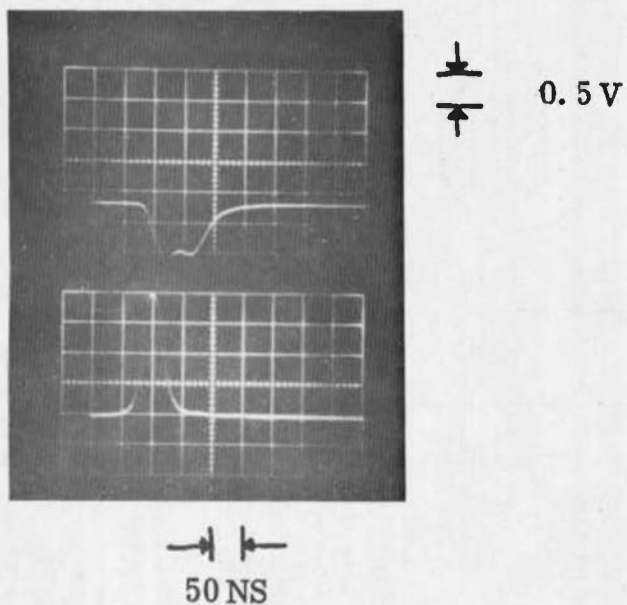
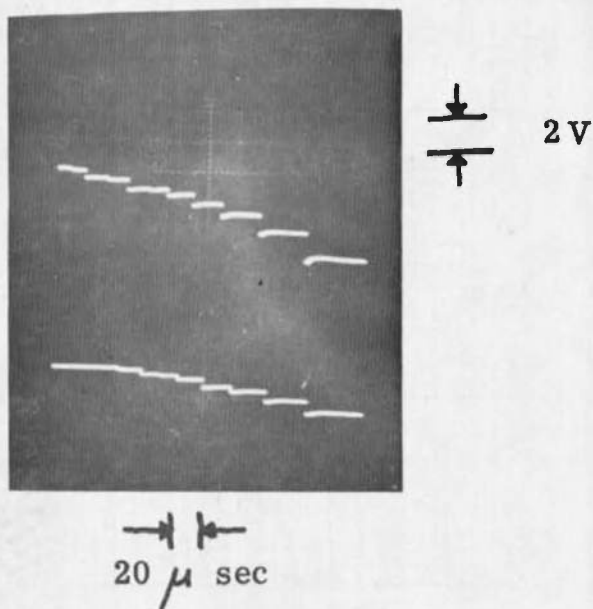


FIGURE 7. BLOCK DIAGRAM OF SIGNAL HANDLING SYSTEM



TOP: GATE GENERATOR OUTPUT

BOTTOM: LASER INTENSITY MONITOR OUTPUT



STORAGE AMPLIFIER OUTPUT

TOP: 0.275 JOULES OUTPUT LASER

BOTTOM: 0.145 JOULES OUTPUT LASER

FIGURE 8. LASER AND ELECTRONICS CIRCUIT CHARACTERISTICS

SECTION III

THOMSON SCATTERING EXPERIMENT

A. Air Arc Experiments

The experimental arrangement was similar to the previous work except the arc generator was a free burning jet and the detector axis was oriented 150° to the laser beam. The electric vector of the laser beam (plane of polarization) was oriented perpendicular to the plane of observation.

1. Gerdien Free Jet Generator

The Gerdien Free Jet arc facility (FIG 9) is one of a family of plasma arcs available at GE-RESO which is based upon the constructed arc principle. This principle is shown schematically in FIG 10. The sketch shown is that of a tandem unit. It is composed of five chambers, two electrode chambers, two vortex chambers, and a plenum. Gas enters the vortex chambers tangentially, some of which passes into the rear electrode chamber, the remaining portion passing into the plenum. That portion which enters the electrode chamber entrains whatever material may evolve from the electrode and the gas carries this with it as it is exhausted overboard. The gas entering the plenum is heated as it passes through the constrictor and again in the plenum where it mixes with the portion of heated gas entering from the opposite side. In a tunnel operation the plenum gas is expanded to lower pressure through a nozzle while in free jet operation the gas expands only subsonically.

The Gerdien Free Jet operates basically on the same principle with some modification (FIG 11). Only one side of this unit is as shown in FIG 10; the other electrode is cylindrical and the arc column exiting from the constrictor actually arcs to the cylindrical wall. By using an external field the arc attachment point to the metal surface is continually moved about the periphery thereby maintaining its integrity. The gas then passes through this second electrode and exits from a subsonic nozzle.

Power is supplied to the facility from a 500 KW DC mercury rectifier unit. Electrical ballast is used in series with the arc to vary arc power. This is provided by variable length of water cooled stainless steel pipe. Although ballast can be changed over a range of ohmage values, it cannot be varied while the arc is in operation.

For the present study test flows were established over a range of arc operating conditions. Maximum arc power was 250 KW, with maximum current being 1100 amps. While a number of different nozzles geometries were used, all the data were generated in subsonic flows; observations were made of the exit flow from an orifice which was 1/8" to 3/8" in diameter depending upon the particular test. These spectrographic measurements were obtained at a distance of 12 mm above the nozzle exit.

2. Laser System

The laser system used for these experiments was a Lear-Siegler LS-140-Q ruby system consisting of a laser head, energy storage bank and control unit.

The laser head is an air cooled (fan) dual-elliptical cavity pumped by linear flash lamps. The ruby rod lies along the common focus of the two ellipses. The Q-switch module consists of uranyl glass separately pumped by a linear flash lamp. One end of the optical circuit is terminated by a resonant reflector with the output end of the ruby rod flat and unelevated.

The system employs three energy storage units rated at 200 MFD at 4000 volts delivering 1600 joules each. Consequently, the system can be charged to 4800 joules. The system can be manually or at 1 pulse/minute.

For both the arc and tunnel experiments, the laser was operated at about 0.7 joules on the Q-switched mode with a pulse width of 30 nanoseconds.

A Lear-Siegler laser energy monitor (M1-2) was used in conjunction with the laser. This is a sampling device in which beam splitters are used to sample a portion of the laser light as it passes through the monitor. Light from the beam splitter illuminates a diffuse spherical reflector which is viewed by a high speed silicon photodiode through a set of optical attenuators. A holding feature of the electrometer readout current permits readings to be made directly in joules within thirty seconds after firing. In addition, the instantaneous power can be read on an oscilloscope. Both the power and energy measurements are considered to be accurate to $\pm 10\%$.

In the Q-switched mode, the beam was elliptical in shape with a divergence of 2.5 by 4 milliradians. The spectral line width was less than 0.1A. In addition to the main laser beam, the laser head produced a highly diverging beam of scattered light which required some baffling in front of the focusing lens in spite of the high attenuation in the detector system. A glass lens, 2" diameter a 16" focal length was used to focus the beam into the arc jet. The lens formed a spot approximately 2 x 3 mm.

3. Alignment Procedure

As mentioned above, a gas He/Ne laser was incorporated into the detector system to facilitate alignment of the detector with the laser. A piece of carbon paper was placed on the jet exit orifice and the laser fired leaving a hole in the carbon paper. The ruby laser was adjusted until the beam was at the desired height — approximately 12 mm above the exit orifice. The gas laser in the detector system was turned on and the plug-in mirror inserted. The focused beam formed by the gas laser was used to adjust the detector to the mark or hole left on the carbon paper by the ruby laser beam. In this manner it was possible to align the detector to within 0.1 mm of the ruby beam. After alignment, the plug-in mirror was removed and the detector closed. Periodically, the alignment was checked.

4. Experimental Procedure

Due to the fact that both electron temperature and concentration measurements are made during a single firing of the laser, it was not necessary to calibrate the arc provided the assumption of equilibrium and clean flow can be made. The philosophy of this work was that no matter how erratic the arc behaved, the simultaneous measurement of temperature and concentration should reflect equilibrium values and hence validate the probe measurements.

With the air flow off, spurious scattering was found to be orders of magnitude greater than the expected signal. This was attributed to Mie scattering in apparently dirty air. Consequently the level of spurious scattering could not be obtained during arc runs to subtract from the Thomson signal. The assumption was made the spurious scattering did not contribute appreciably to the Thomson signal. Occasionally, a large signal would be obtained indicating a particle or particle cloud was struck and the results disregarded.

Periodically a check was made on the experimental data for distinguishing features of Thomson scattering:

1. Synchronization with the laser pulse
2. Polarization in the same sense as the input polarization
3. Misalignment of the detector with the laser beam to insure that the recorded signal is not some anomaly of the plasma.

After the arc was initiated, the laser was fired after the arc stabilized (~ 3 sec). The outputs of PM's #1, #2 and #3 were recorded on scopes (see electronics section). FIGS 12, 13, 14 show some typical oscillograms obtained during an arc run from PM's #1 and #2. All runs were made with the PM voltage at -1200 volts, the entrance slit of the detector at 50μ and a slit height of 1 mm. The average energy of the laser was recorded for each run with the energy monitor, varying between 0.4 to 0.7 joules. The initial delay evidenced in the oscillogram is due to the transit time through the optics and the PM's as the trace was initiated from the energy monitor.

5. Data Reduction and Results

In order to relate the observed voltage signals from PM's #1 and #2 into electron concentration, it was found more expedient (rather than working from a normalized calibration curve) to derive a working equation. This is derived in the appendix with the results,

$$N_e = \frac{\phi_T \text{ (measured)}}{J \text{ (measured)}} 3.60 \times 10^{10} \text{ (cm}^{-3}\text{)} \quad (1)$$

where ϕ_T is the sum of photons received by PM's 1 and 2 and J is the energy measured in joules. The electron temperature was obtained by ratioing PM's 1 and 2 after converting to photons using the calibration curve FIG 6 .

The initial experiments utilizing the free jet showed the existence of large high frequency fluctuations in the intensity level of the plasma radiation. This resulted in unacceptably large fluctuations in the voltage at the input to the gated integrator. These were amplified and coupled to the output causing a base-line shift which made accurate measurement of the gated integrator output during the laser pulse difficult. The amplifier circuits were therefore modified to have a 20 KHZ low frequency cut-off. This reduced the effect of the arc fluctuations to an acceptable level. FIG 15 is a typical oscillogram of the arc background fluctuations obtained from PM #3 (background channel). The sweep is $50\mu\text{sec/cm}$ and amplitude is 2 V/DIV. The output of PM #3 was coupled into a $1 \text{ M}\Omega$ resistor paralleled by a 120 PF capacitor.

Approximately 150 air arc tests were made in an effort to validate the instrument response. Initially, using copper and carbon electrodes for the arc, measurements of electron concentration and temperature yielded inconsistent results. The ratio response which is a measure of electron temperature did not correlate with the total response which is a measure of electron concentration. The results were also not reproducible yielding a range of temperatures and concentrations. The results also indicated that there is still some interference from solid particles in the arc jet.

The arc configuration was changed to both carbon electrodes which produces a higher temperature jet. With the laser probe aligned approximately 12 mm above the exit orifice of the jet, runs were made in which only the electrical ballast to the arc was changed. As the ballast was lowered, the instrument registered higher temperatures as expected; however, at the lowest ballast conditions an unexpected decrease in temperature was observed (Table I). Due to the uncertainties experienced with the arc jet, it was decided to perform a spectrographic profile of the jet at the position of the laser scattering experiments.

A 2 meter B&L spectrograph in conjunction with a dove prism was used to characterize the arc jet. The dove prism was necessary to invert the jet image such that the spectrographic slit cut radially across the jet at 12 mm from the exit orifice. The initial spectrogram showed atomic copper lines, calcium atomic and ion lines (impurities) and atomic lines of nitrogen and oxygen in addition to bands systems of CN and C₂. Using a calibrated tungsten strip an absolute calibration was made. The copper lines reflected a temperature of 5000°K. By using the ratio of the atomic to ionic lines of calcium, which is sensitive to temperature and electron concentration, an electron concentration of 10^{14} cm^{-3} was measured. The equilibrium value is 6.4×10^{13} indicating that impurities may be increasing the concentration over equilibrated air. This deviation was not enough to account for the large deviation measured with the electron probe (a factor of 10 over equilibrium conditions). In addition, there is some doubt as to the radiating regions of both calcium and copper (i. e. if calcium is radiating from a different volume than the copper then the above results would be inconclusive). Consequently, an absolute line intensity measurement was made on the nitrogen atomic line at 7424Å. In addition using a standard inversion technique⁽¹⁾, it was possible to obtain the radial temperature profile of the arc jet. This is a lengthy procedure and subject to many errors; however, the results obtained can sometimes be useful. It was found that from the edge of the nitrogen radiating region (approximately 7 mm from the center of the arc jet) to the center, the temperature ranged from 7100°K to 8000°K. This is rather a flat profile and quite unexpected for a jet of this type as a higher temperature gradient would be expected. This would seem to suggest that the jet column is swinging from side to side in some manner which would tend to reduce the observed temperature gradient. If this be the case, it would also explain the large variation of results obtained with the laser probe as during a typical firing of the laser, the scattering takes place at different locations in the arc jet.

To resolve the large variation of electron concentration and temperature obtained, high speed movies of the arc jet were taken with a Dynafax camera. This camera takes pictures of $1\ \mu$ second duration and about $40\ \mu$ seconds apart. Movies were taken at about the same time that the laser is fired after the arc is initiated (~ 3 sec). The movies showed sharp local variations of luminosity from frame to frame (FIG 16). In some cases a given point in the jet column shows no luminosity while at later times shows maximum luminosity (complete blackening of the film). As the luminosity observed is probably due to the CN molecule emission an attempt was made to obtain high speed movies of the jet using an oxygen filter (7947A) with the camera. This proved unsuccessful as the luminosity was not sufficient to expose the infrared film, even at reduced exposure times.

As the laser probe results were obtained with a sampling time of about 50 nanoseconds while the dynafax pictures were of $1\ \mu$ second duration, it would be difficult to obtain any correlation between the two. In addition, as the luminosity of the CN molecule is not necessarily linearly related to electron temperature or concentration we were not able to reach any conclusion as to the validity of the laser probe results. Further, to obtain enough of a statistical sampling to correlate the results with the spectrographic results would require thousands of runs which is not feasible. Consequently, at this stage of the program, it appears that validation of the laser probe is not possible in the arc jet source being used. Validation would require a more stable and uniform source than is currently available.

Although we were confident that the probe results are accurate (based on our previous calibrations), our inability to validate the results dictated that we discontinue our testing in the present source. Consequently, the laser probe was set up in our High Enthalpy shock tunnel which is described in part B.

6. Discussion of Results of Table I

Although Fastax movies of the arc jet indicated that at the time of the laser firing, the position of the jet with respect to the laser and detector can vary giving a range of temperature and concentrations, it was noted at about 6000°K , the electron concentration indicated an air equilibrium value. At lower temperatures it would appear that impurities control the electron temperature which is reflected in the very high electron concentrations. At the lowest ballast (highest current density) it also appears that so much material is drawn off from the electrodes that the plasma temperature is again controlled by the impurity level. Between 6000 and 7000°K the results seem to indicate that both air electrons and impurity electrons contribute to the temperature which is reflected in the higher than equilibrium values for concentration.

B. Shock Tunnel Experiments

1. High Enthalpy Shock Tunnel Facility

This facility has a high performance electrical discharge heated-helium driver. The driver is 4 1/2 feet in length and normally is operated with an electrically insulated sleeve having a 2 1/2 inches I.D. The sleeve has an inner coating of bonded RTV rubber, which provides the electrical insulation required. Operation is off of a 768 KJ capacitor bank with a maximum voltage ratio of 40 KV. The driver tube, made of stainless steel, is 17 feet long and has a 2 inches I.D. In the current study, the facility was operated as a shock tunnel in the reflected mode. A converging-diverging conical nozzle was located at the downstream end of the tube. This nozzle has a 1°50' half-angle. Measurements were taken at the 3.6 area ratio station where the nozzle diameter was 0.38". A sketch of the facility is given in FIG 17. Here an MHD accelerator is located at the downstream end of the driven tube instead of the conical nozzle. A dump tank is downstream of the nozzle or accelerator section. In these experiments, the MHD accelerator was not used.

2. Experimental Arrangement

The experimental arrangement used in the high enthalpy shock tunnel is depicted in FIG 18. The detector was orientated 173° to the laser beam with the plane of polarization perpendicular to the plane of observation. Due to the excessive scattering of the laser beam from the entrance window, it was necessary to provide a light dump composed of a carbon block with a tapered hole. The surface reflection from the focusing lens provided enough laser light for an EG&G lite-mike which was used to indicate the time of the laser pulse. It was also found necessary to provide a 1-meter long collimator tube composed of 1 cm diameter aperture every 1" along the collimator tube. This was dictated by the widely divergence scattered beam originating within the laser cavity. The Lear-Siegler energy monitor was used to provide the energy measurements of the laser beam.

Due to the angle at which scattering was observed, the scattering volume was an ellipse cylinder 1 mm x 12 mm x 50 μ . The experimental results were obtained at a point approximately 7 mm downstream of the flow from the exit nozzle. FIGS 26 and 27 are photographs of the experimental set-up.

3. Experimental Procedure

Initially, the detector was aligned to the laser beam using the procedure outlined in the arc tests. The tunnel was pumped down and the laser was fired to indicate the level of spurious scattering. Only the $(\cosine)^2$ channel indicated any spurious scattering. The level of spurious scattering was constant to the normalized laser output indicating only apparatus scattering rather than Mie scattering. During the pre-test runs the Lite-Mike was calibrated in terms of its output against the energy monitor. Typical oscillograms taken during a pre-test are shown in FIGS 21, 22, 23. FIG 21 shows the output of PM #1 at $20 \mu\text{sec}/\text{CM}$ and $5 \text{ V}/\text{CM}$. FIG 22 shows the output of PM #2 at $50 \mu\text{sec}/\text{CM}$ and $5 \text{ V}/\text{CM}$ and FIG 23 shows the output of PM #3 (top trace) at $1 \text{ V}/\text{CM}$ and $50 \mu\text{sec}/\text{CM}$ and the output of the Lite-Mike (bottom trace) at $100 \text{ MV}/\text{CM}$ and $50 \mu\text{sec}/\text{CM}$.

During the tests conducted on the high enthalpy shock tunnel flow, a pressure gage in the driven tube wall was used to provide a master trigger signal from which the triggering of all scopes and of the laser flash lamps was obtained through appropriate delays. Two oscilloscopes were used to display the outputs of sidewall pressure gages further downstream whose signals were displayed in pairs on each scope to provide a measure of shock wave velocity. A third scope was used to display the reflected region pressure as a check on the state of the test flow at the time of laser Q-switching. Oscilloscope #5 displayed the output of PM #3 and of the EG&G. Lite-Mike energy monitor as a check on background light and energy in each laser pulse. Scopes #6 and #7 displayed the amplified outputs of PM's #2 and #1, respectively.

In general, the Q-switching of the laser occurred about 900 microseconds after triggering of the flash lamps. Therefore, a delay of about 100 microseconds after the main trigger would assure laser Q-switching during established test gas flow in the nozzle.

4. Data Reduction and Results

In order to translate the PM outputs into electron temperature and concentration, it was necessary to reprogram the line shape equation for $\theta = 173^\circ$. As constant pressure cannot be assumed in this case as it was in the free jet, the program consisted of solving the line shape equation for constant α and a range of temperatures from 4000°K to 8000°K and computing the response of each channel. As a given $\alpha + T_e$ with θ constant define an N_e , it was possible to plot N_e , T_e , and α against ρ the ratio of the (sine)² channel to the (cosine)² channel. This is reproduced in FIG 24. To show that the sum of channels #1 and #2 are independent of α within the temperature range, the results of the computer program provided a plot of N_e , α , response of #1, #2 and the sum of #1 and #2 against ρ/joule . This is reproduced in FIG 25. The program listing and the results of the program is reproduced in the Appendix.

In order to facilitate the determination of the electron concentration a working equation similar to the arc runs was derived from the geometry of the arrangement. The calculations are relegated to the Appendix with the result,

$$N_e = 6.80 \times 10^9 \frac{\rho \text{ measured sum}}{\text{Joule (measured)}}$$

With the determination of N_e and measured ratio it was then possible to determine the electron temperature from FIG 24 independent of knowing the pressure or state of equilibrium. For each run the value of the constant apparatus scattering was subtracted from the observed output before the computation was made. The N_e computation can be made from calibration curves in FIG 25 or from the above equation.

Due to limitation of funds only two tunnel runs could be made. The oscillograms from one of them, Test 304 is shown in FIGS 26, 27 and 28. In FIG 26 the upper trace shows the varying response from PM #3 and the bottom trace the output from the energy monitor. As can be seen, the laser Q-switched twice. The first pulse produced enough scattering to show up in PM #3. FIG 27 indicates that PM #1 saturated (~ 10 volts), consequently, a determination of T_e and N_e could not be made. However,

it is instructive to compute at what level PM #3 would show a laser signal. With a resistive load of $100\text{ K}\Omega$ the change in current during the laser pulse was 4×10^{-6} amps. With a sensitivity of $2.3 \times 10^{16} \text{ } \phi/\text{C1}$ this corresponds to $9.2 \times 10^{10} \text{ } \phi/\text{sec}$. Assuming a laser pulse duration of 30×10^{-9} secs., PM #3 received 2800 ϕ . The energy of the pulse was 0.44 joules and hence the output from PM #3 represents = 6400 ϕ/joule . With a transmission of 0.61 for this channel this corresponds to $\sim 10,550 \text{ } \phi/\text{joule}$ at the entrance to the detector within the band-pass. The output from PM #2 (FIG 35) indicates an energy input of $\sim 108,000 \text{ } \phi/\text{joule}$ using a similar analysis. Due to the fact that PM #1 contains some constant spurious scattering plus Thomson signal, the output of PM #1 was calculated for the conditions of the run at the time of the laser pulse (i. e. $T_e = 6600^\circ\text{K}$ and $N_e = 5 \times 10^{15}$). Calculating the expected return for PM #1 and adding the amount of spurious scattering as calculated from the energy monitor, the input to PM #1 at the entrance to the detector amounted to 300,000 ϕ/joule . As PM #3 records the sum of PM's #1 and #2, this indicates that PM #3 sees approximately 2.5% of the Thomson signal. This is not unexpected as the Wollaston prism separating the two polarization states is not anti-reflection coated and Fresnel reflection from the prism finds its way into PM #3. This is not particularly objectionable as PM's #1 and #2 were calibrated in the presence of the surface reflection.

As the laser Q-switched twice, it was possible to obtain a result on the second pulse (with less energy) as neither PM #1 or PM #2 were saturated. The second pulse in PM #2 is not visible in the reproduction. Inserting the appropriate values the total return to PM's #1 and #2 was 44,000 ϕ . From the working equation we obtain $N_e = 2.8 \times 10^{15}$. The ratio of #2/#1 was 0.600 and hence from FIG 31 we obtain $T_e = 6000^\circ\text{K}$. An error statement is discussed in the Appendix.

In FIGS 29, 30, 31 the outputs are reproduced for Test #305. In this case the laser Q-switched three times. The first pulse again saturated PM #1. The second pulse indicated particle scattering as the ratio obtained was about 10:1 (no PM #2 output). Only pulse number 3 could be used for analyses. For this pulse PM #1 recorded 43,500 ϕ and PM #2 31,900 ϕ . The ratio 0.732 and the N_e obtained from the working equation indicated an $T_e = 6500^\circ\text{K}$ and $N_e = 5.7 \times 10^{15}$ were indicated. The comparison of these results with the value measured from pressure and velocity measurements are indicated below:

Test #304

Ne (Laser) → 6000°K
Ne (Actual) → 6000°K
Te (Laser) → $2.8 \times 10^{15}(\text{cm}^{-3})$
Te (Actual) → $3 \times 10^{15}(\text{cm}^{-3})$

Test #305

6500°K
6530°K
 $5.7 \times 10^{15}(\text{cm}^{-3})$
 $5.5 \times 10^{15}(\text{cm}^{-3})$

Although two results are not an indication of the validity of the probe, the value of these probe results are described in a paper of C. J. Harris of the Environmental Sciences Laboratory staff which is reproduced in the Appendix.

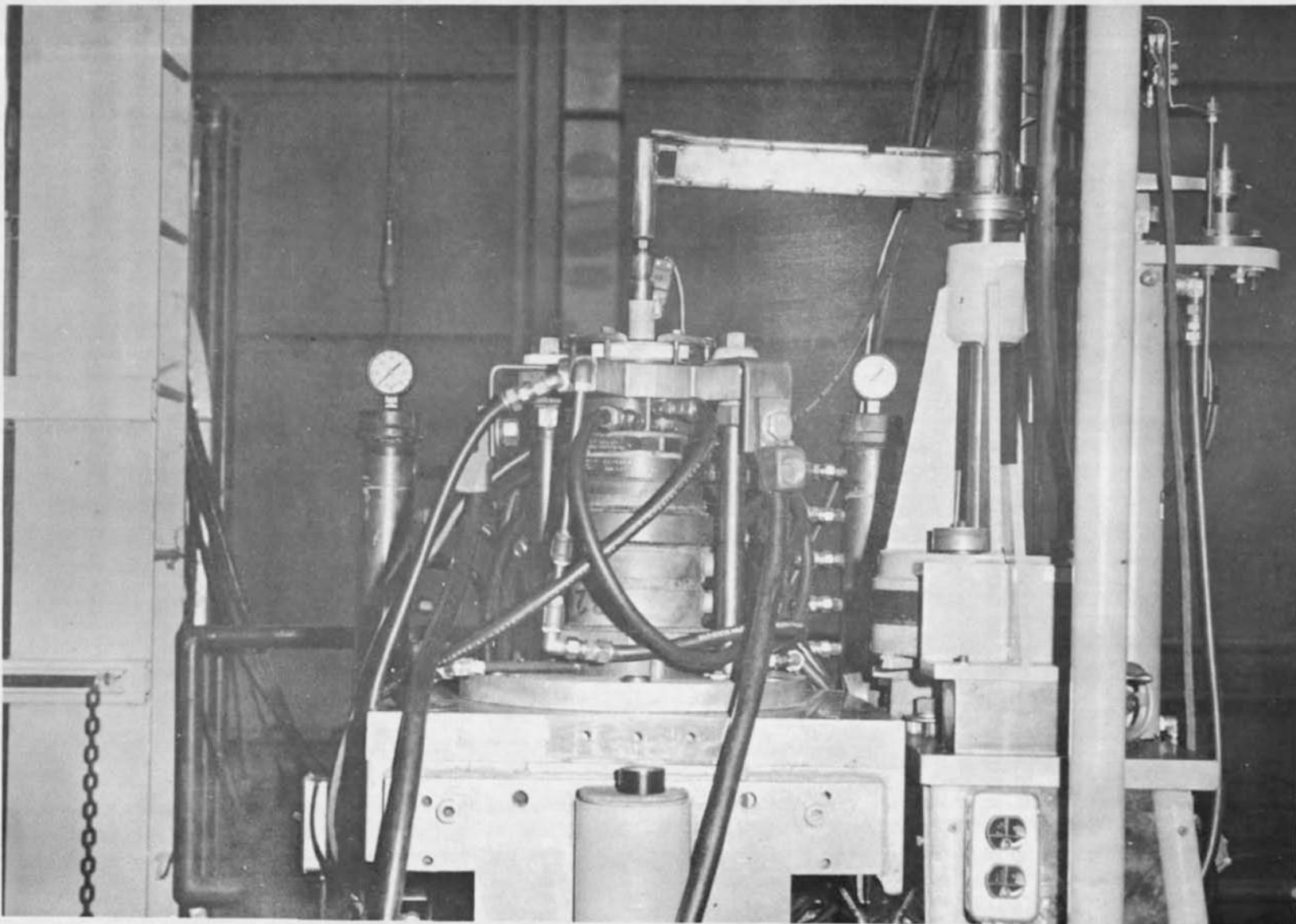


FIGURE 9. GERDIEN FREE JET FACILITY

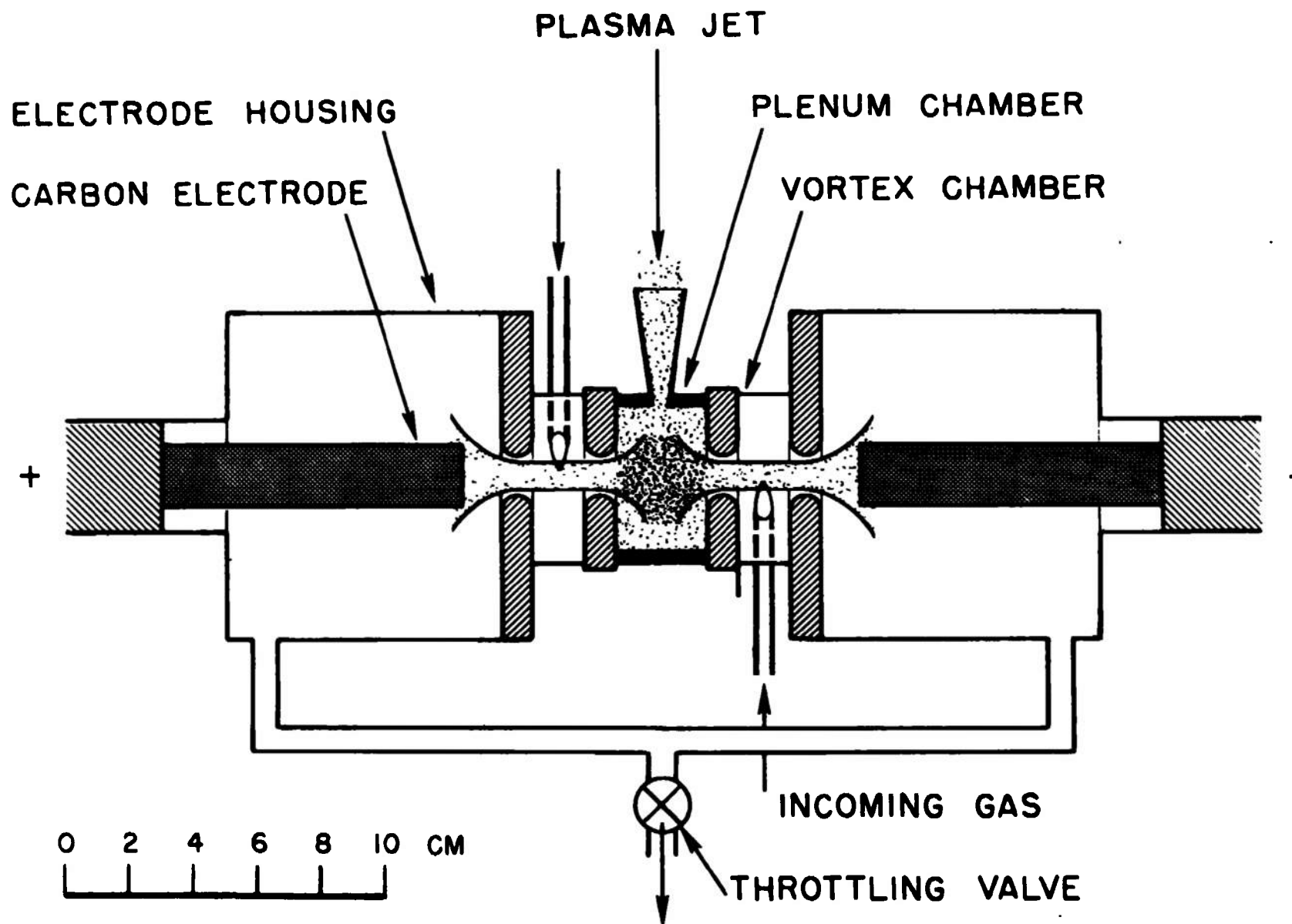


FIGURE 10. SCHEMATIC TANDEM GERDIEN ARC HEATER

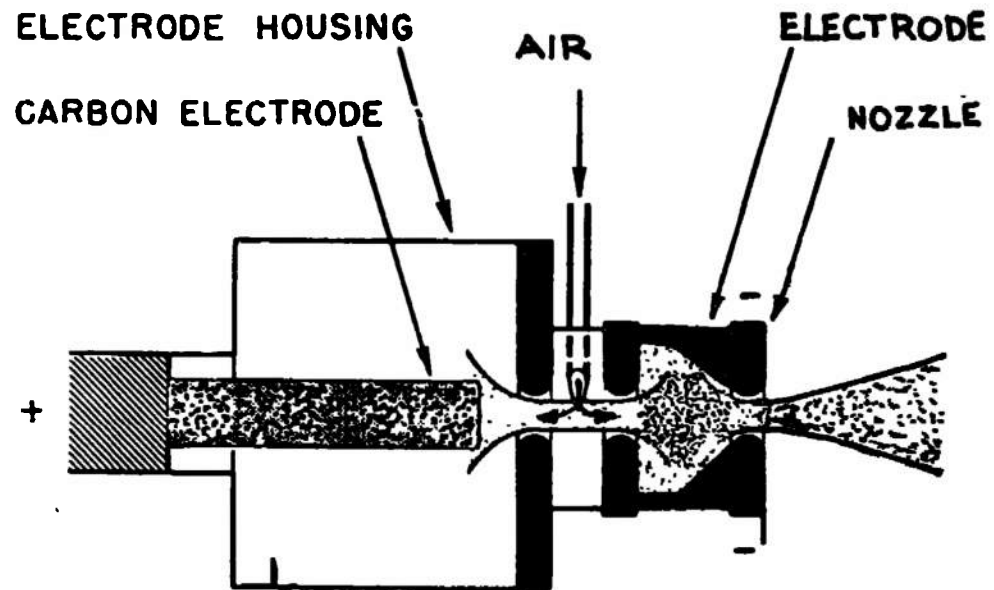
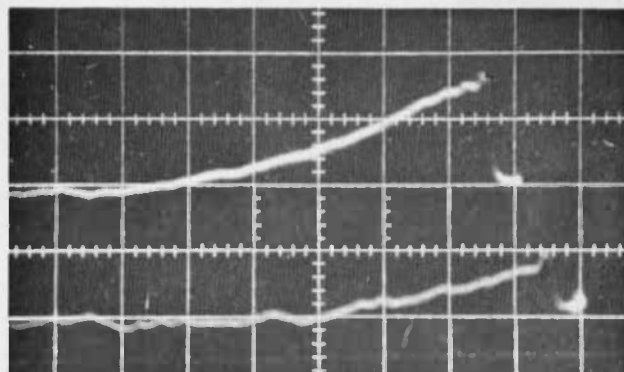


FIGURE 11. SCHEMATIC OF GERDIEN FREE JET

FIGURE 12

RUN #133

0.52 J



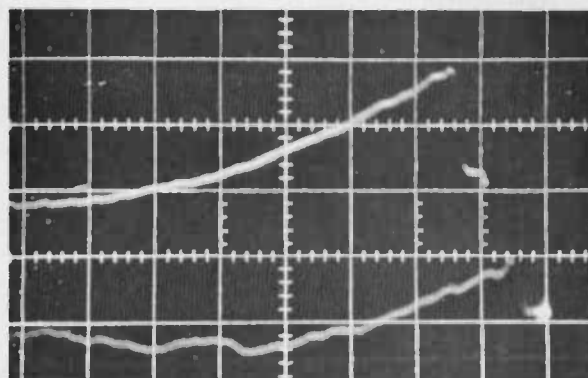
↓
↑
0.5 V

→ ←
0.5 sec

FIGURE 13

RUN #134

0.47 J



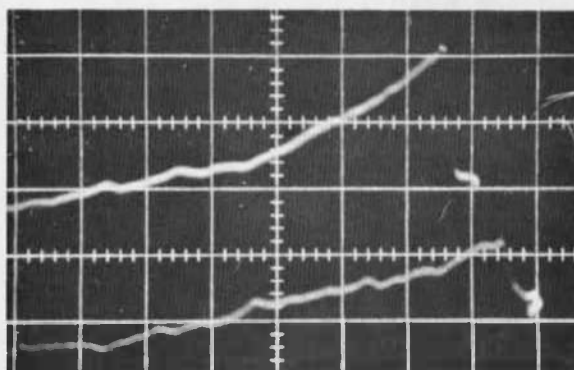
← PM #1

← PM #2

FIGURE 14

RUN #135

0.45 J



↓
↑
0.2 V

TYPICAL OSCILLOGRAMS FROM ARC JET RUNS

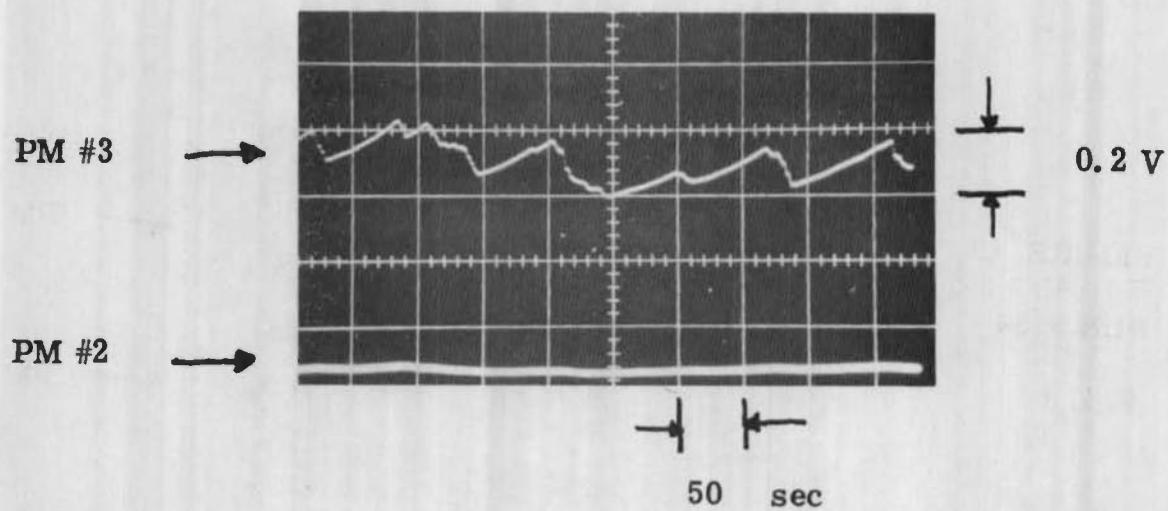


FIGURE 15. OSCILLOGRAM OF ARC BACKGROUND

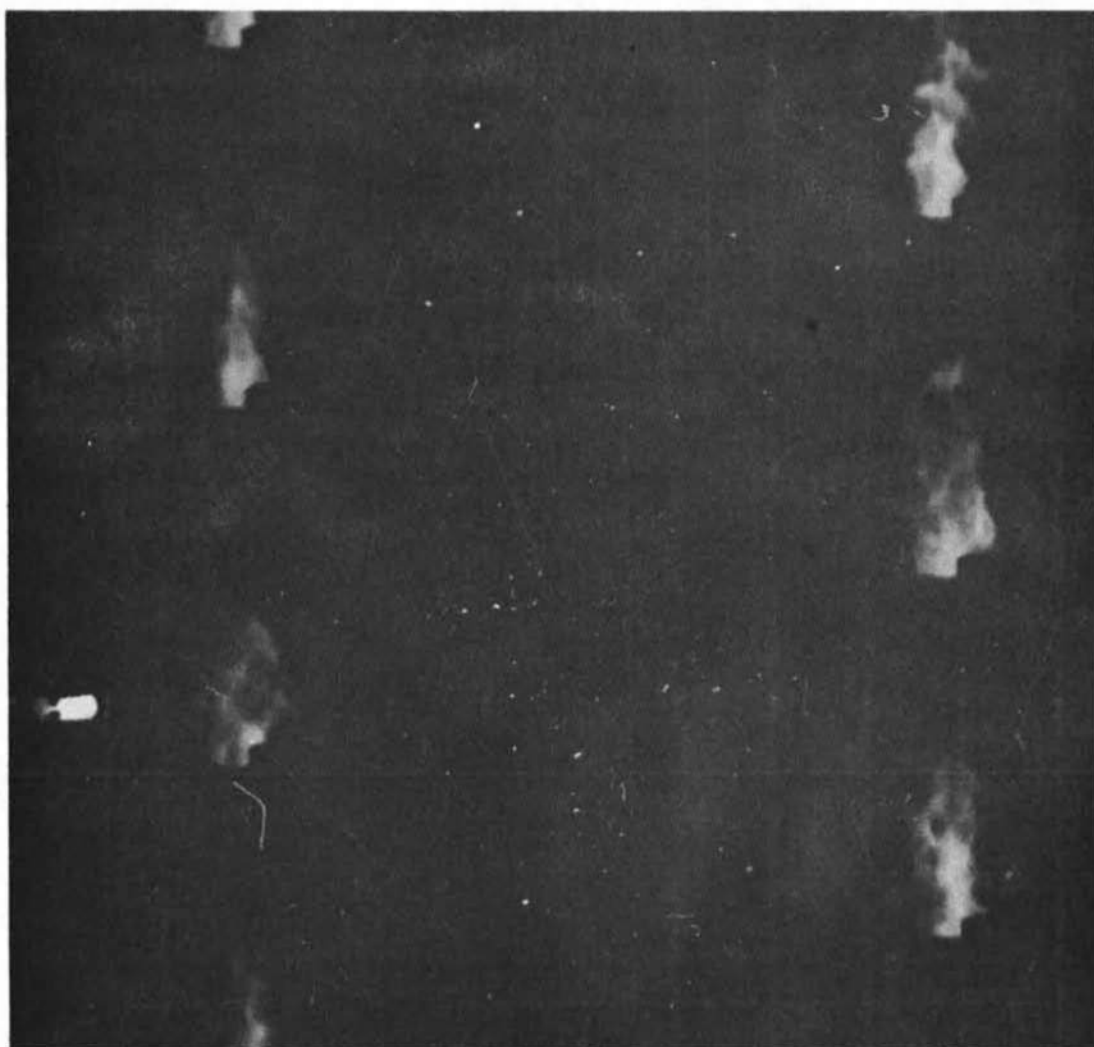


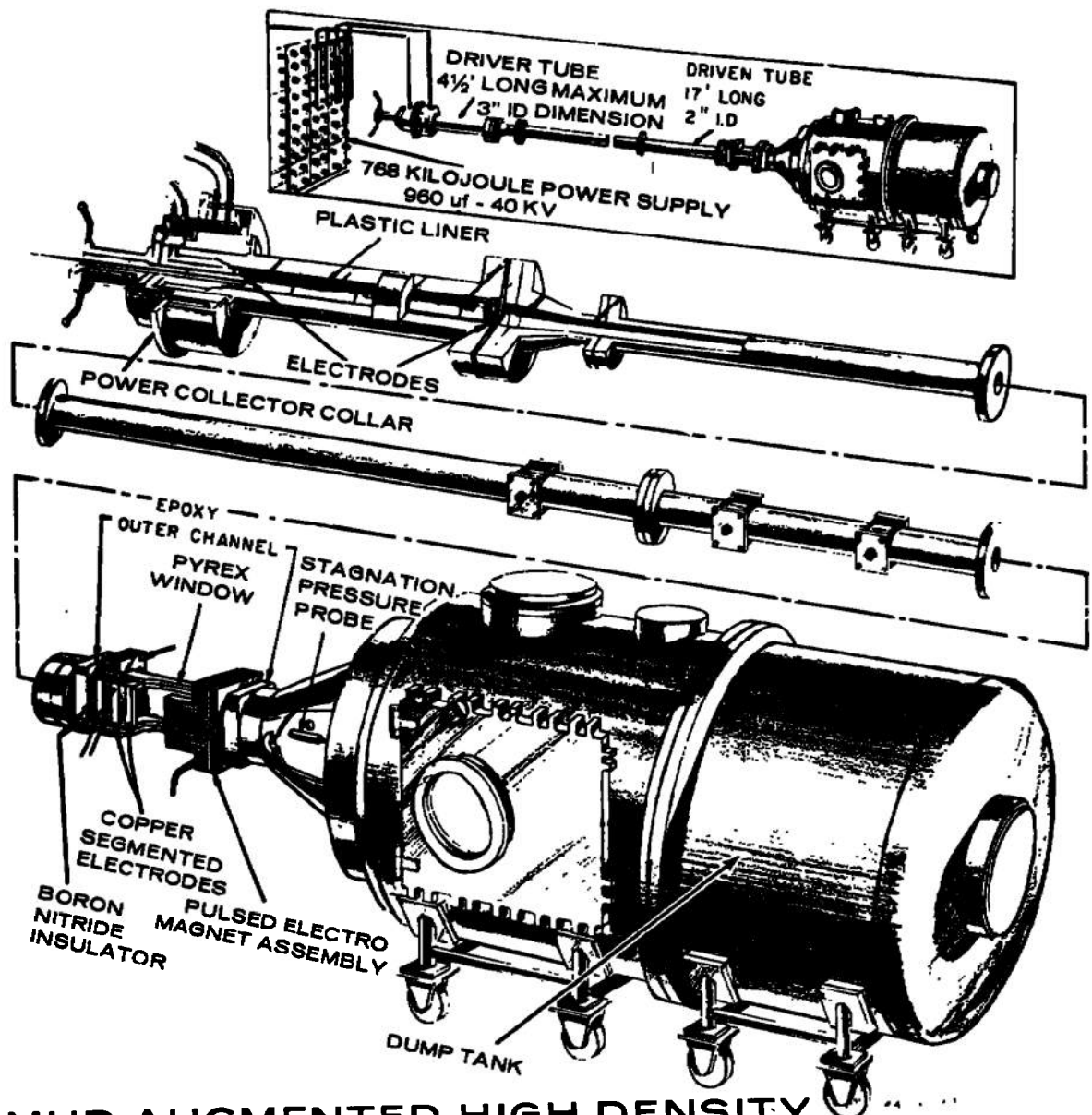
FIGURE 16. PORTION OF FASTAX MOVIES OF ARC JET

TABLE I

Height Above Jet - 12 mm
 Slit Width - 50 μ
 Slit Height - 1 mm

Ballast (Ohms)	0. 52	0. 52	0. 39	0. 39	0. 26	0. 26	0. 195	0. 195	0. 195
Energy (Joules)	0. 49	0. 54	0. 54	0. 52	0. 48	0. 46	0. 48	0. 52	0. 51
Run No.	117	118	119	120	121	122	123	124	125
V ₁ (MV)	505	540	775	425	375	350	400	475	425
V ₂ (MV)	65	95	95	100	115	125	50	50	60
ϕ_1 (14. 5 ϕ /MV)	7, 300	7, 830	11, 240	6, 160	5, 440	5, 080	5, 800	6, 890	6, 160
ϕ_2 (11. 8 ϕ /MV)	770	1, 120	1, 120	1, 180	1, 360	1, 480	590	590	700
($\phi_1 + \phi_2$)	8, 070	8, 950	12, 360	7, 340	6, 800	6, 560	6, 390	7, 480	6, 860
R	0. 105	0. 143	0. 100	0. 192	0. 250	0. 291	0. 102	0. 086	0. 114
Te ($^{\circ}$ K)	3, 000	3, 800	2, 950	5, 400	6, 700	7, 300	2, 950	3000	3, 200
Ne x 10 ⁻¹⁴ (CM ⁻³)	5. 9	6. 0	8. 2	5. 1	5. 1	5. 1	4. 8	5. 2	4. 8
Ne x 10 ⁻¹⁴ (CM ⁻³) [*] eq.	6. 4 x 10 ⁻⁴	. 04	6 x 10 ⁻⁴	0. 9	6. 1	8. 8	6 x 10 ⁻⁴	6 x 10 ⁻⁴	7 x 10 ⁻⁴

*Indicates the electron concentration at the measured temperature for equilibrated air.



MHD AUGMENTED HIGH DENSITY SHOCK TUNNEL

FIGURE 17. MHD AUGMENTED HIGH DENSITY SHOCK TUNNEL SHOWING PRESSURE INSTRUMENTATION STATIONS

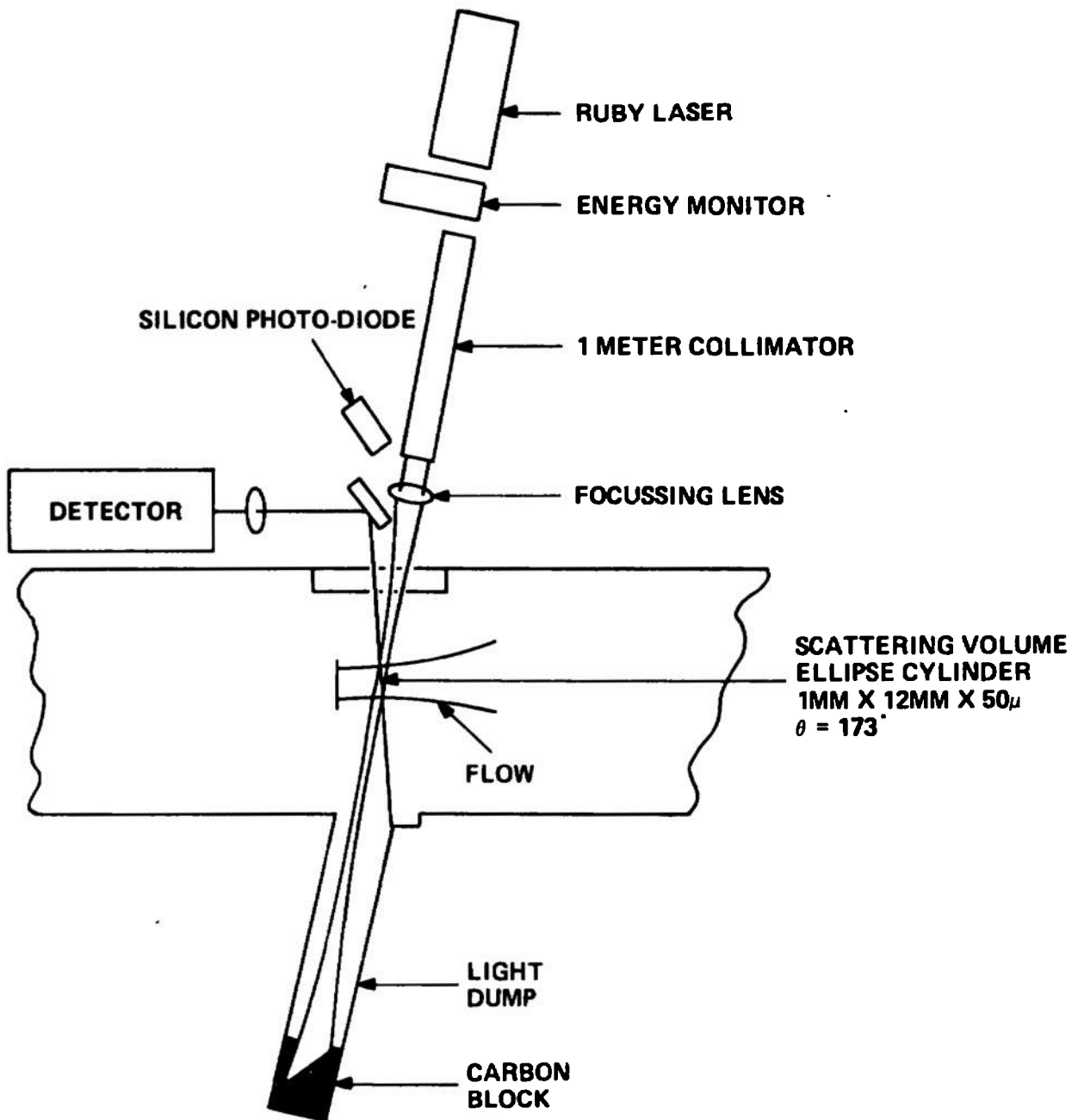


FIGURE 18. EXPERIMENTAL ARRANGEMENT FOR PROBE

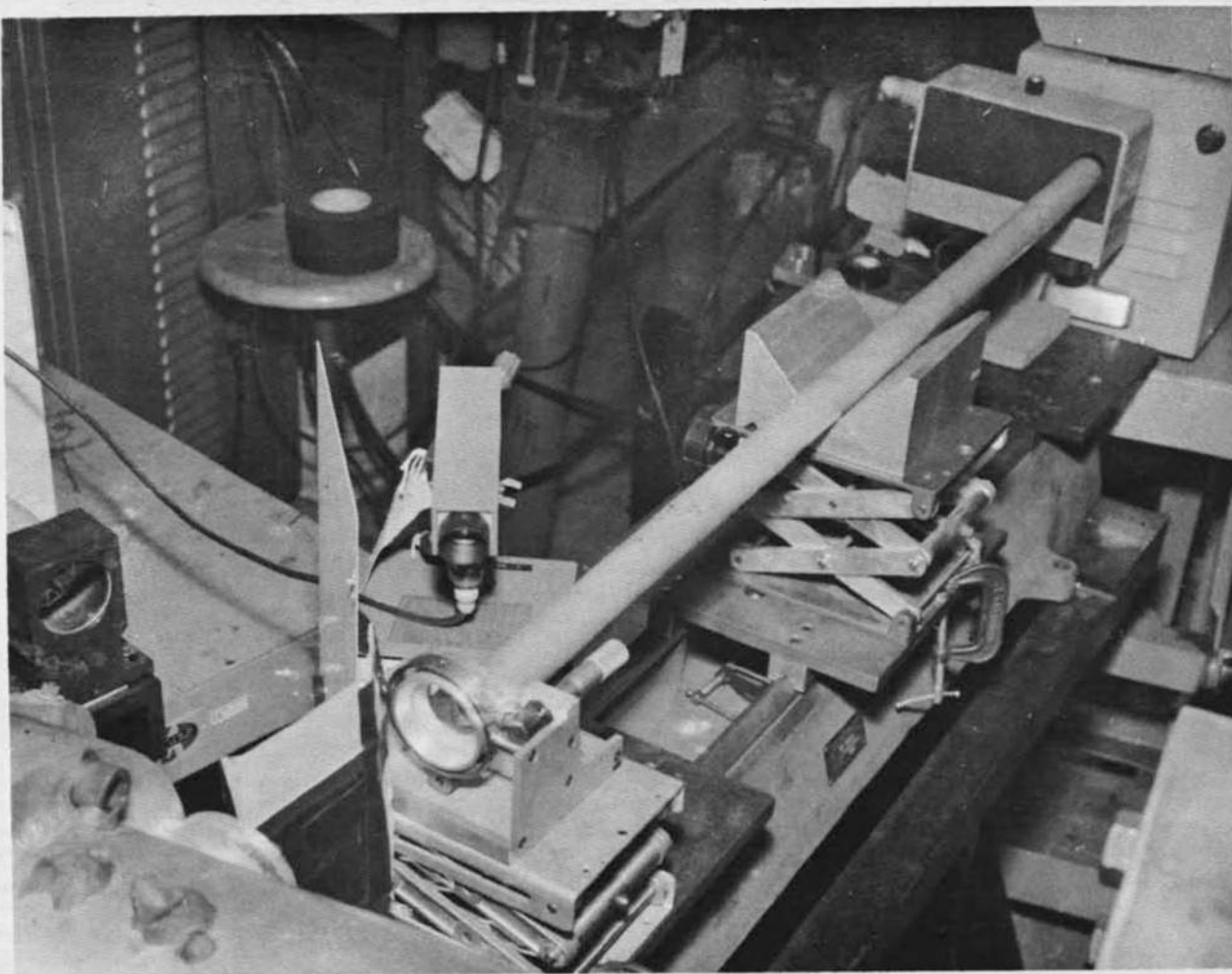


FIGURE 19. PHOTOGRAPH OF LASER PROBE EXPERIMENTAL SET-UP



FIGURE 20. PHOTOGRAPH OF LASER PROBE EXPERIMENTAL SET-UP

FIGURE 21
(PM #1)

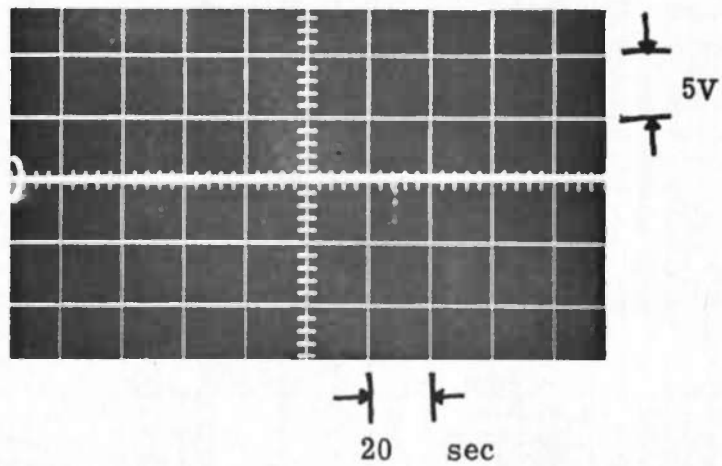


FIGURE 22
(PM #2)

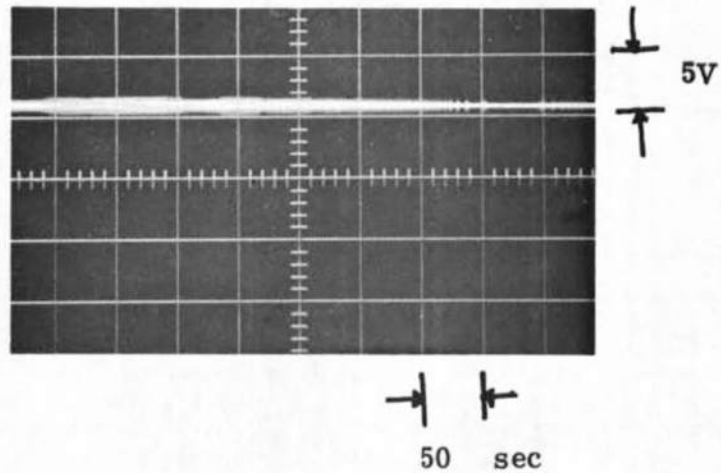
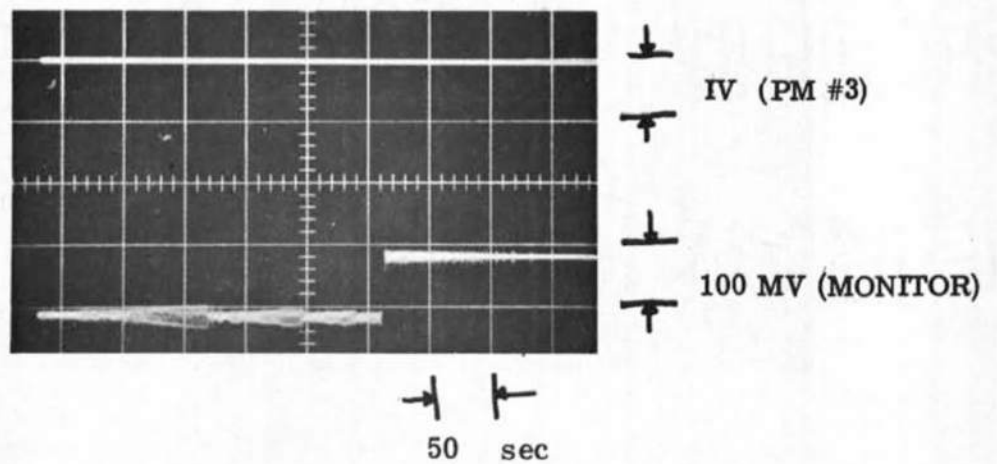


FIGURE 23
(PM #3
AND MONITOR)



TYPICAL OSCILLOGRAMS DURING TUNNEL PRE-TEST

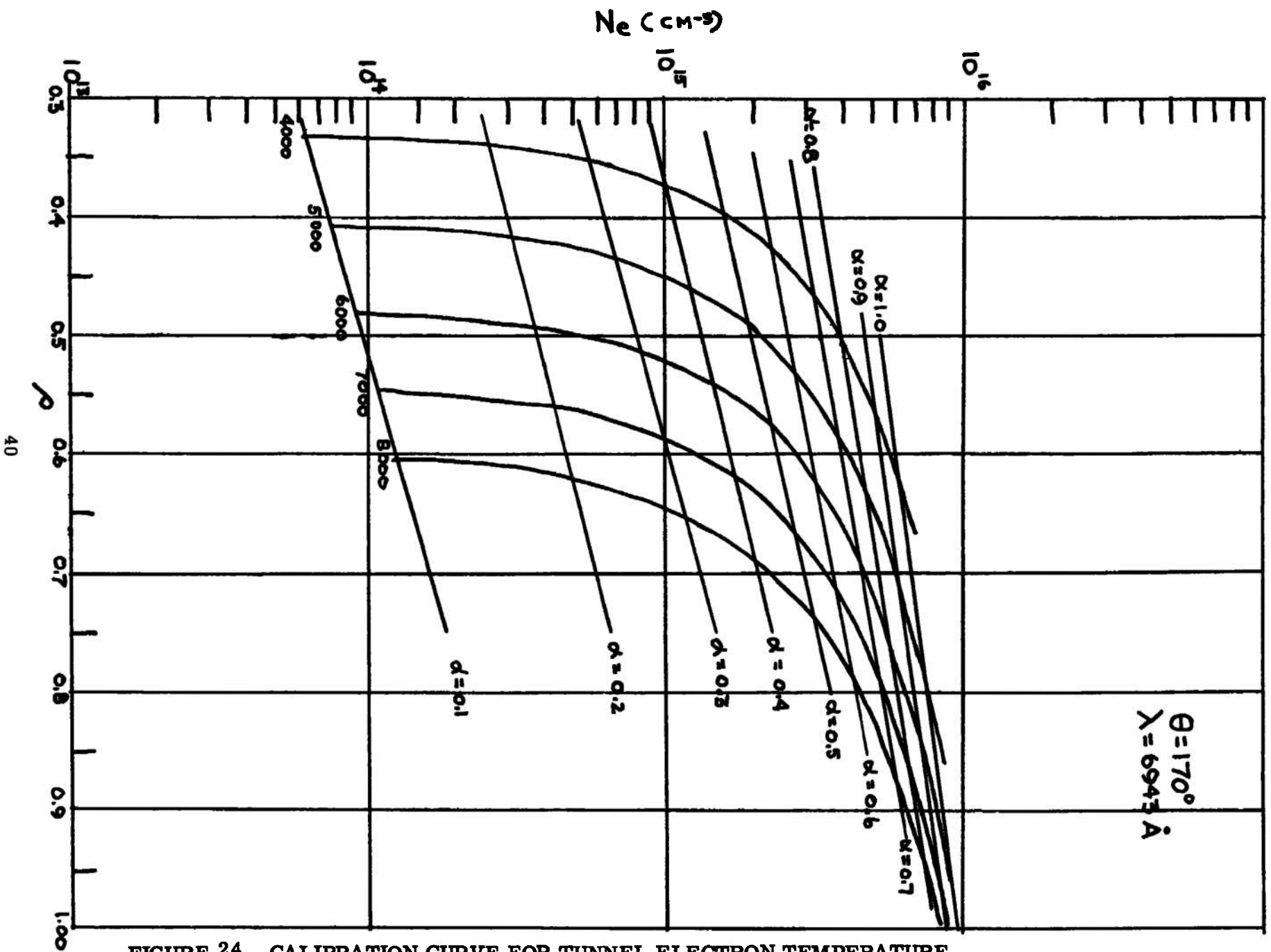


FIGURE 24. CALIBRATION CURVE FOR TUNNEL ELECTRON TEMPERATURE

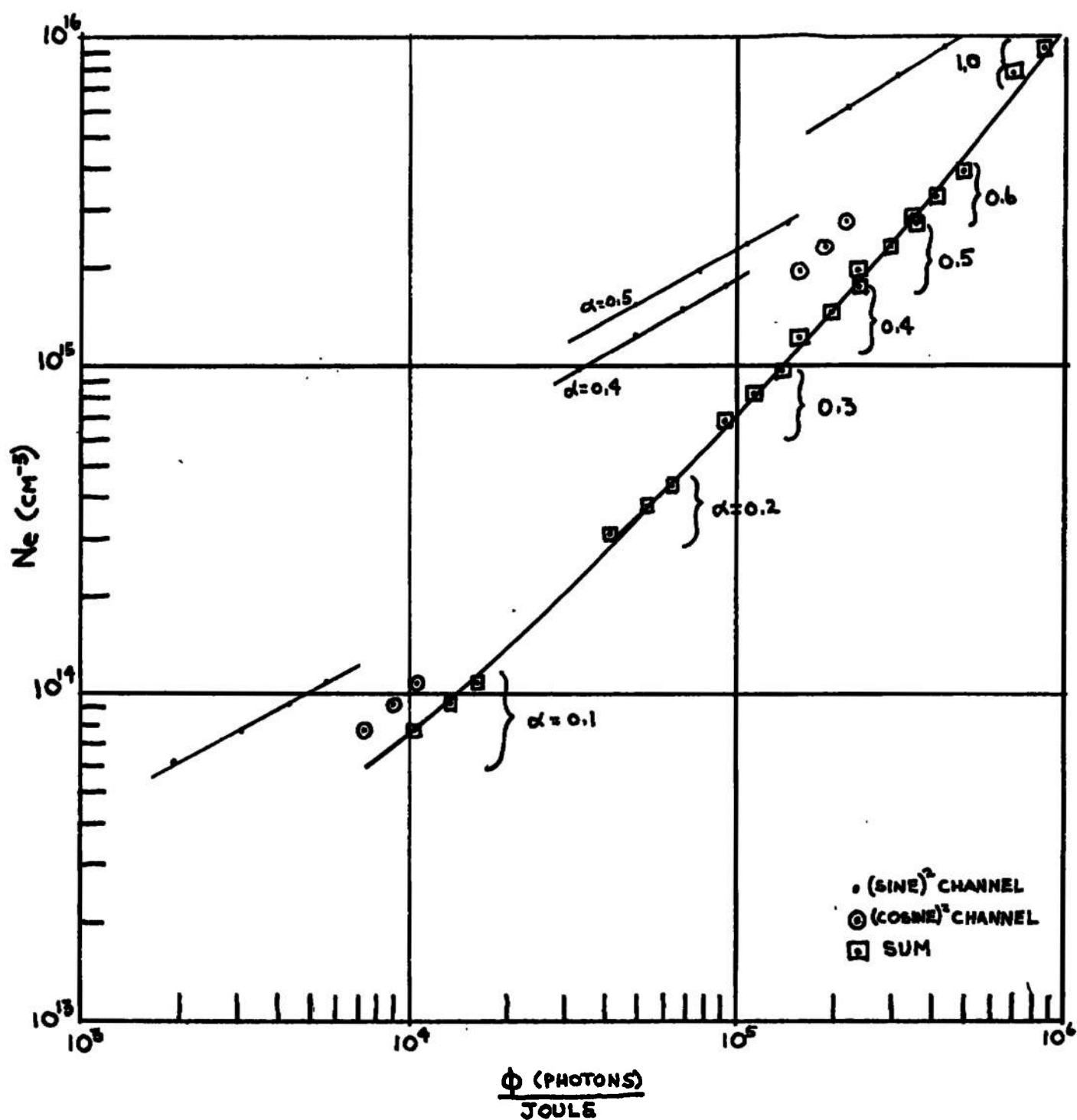
FIGURE 25. CALIBRATION CURVE FOR TUNNEL N_e

FIGURE 26
(PM #3)

(MONITOR)

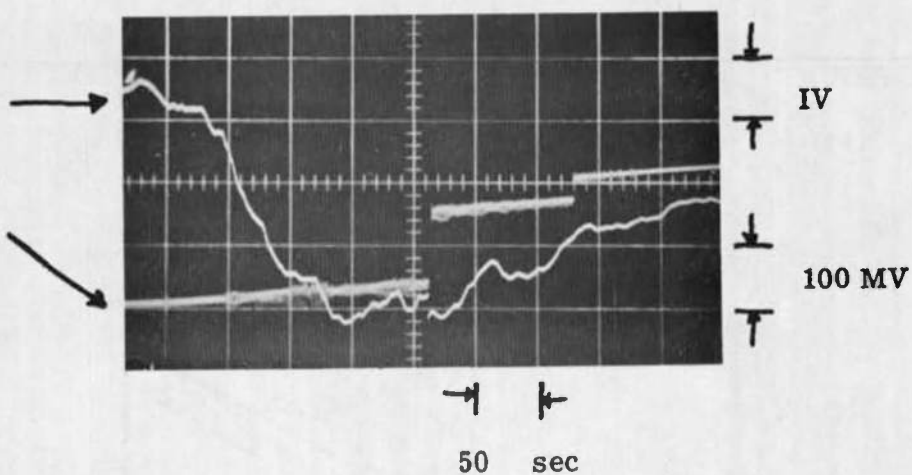


FIGURE 27
(PM #1)

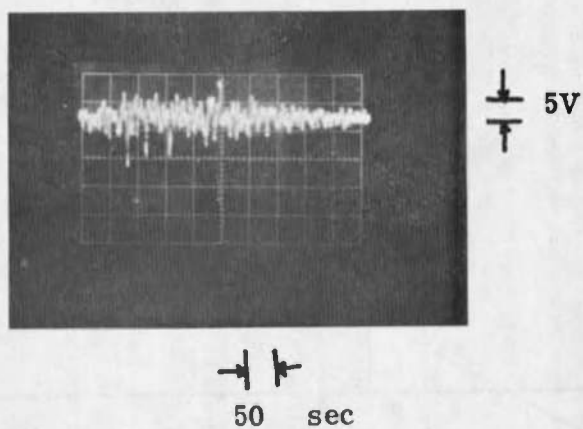
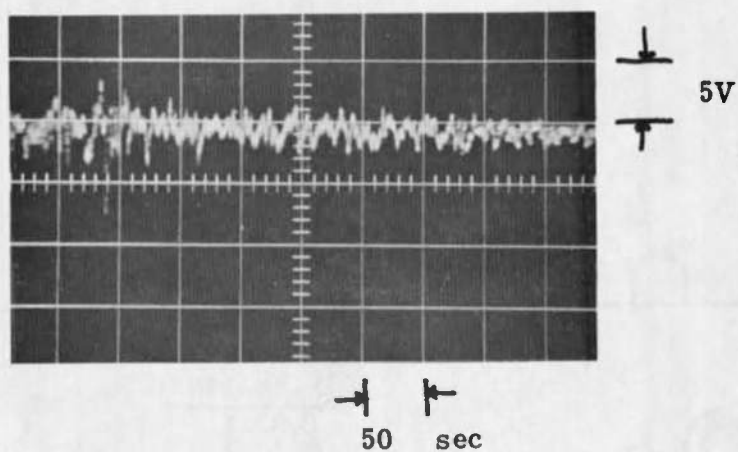


FIGURE 28
(PM #2)



OSCILLOGRAMS FROM TUNNEL TEST #304

FIGURE 29

(PM #3)

(MONITOR)

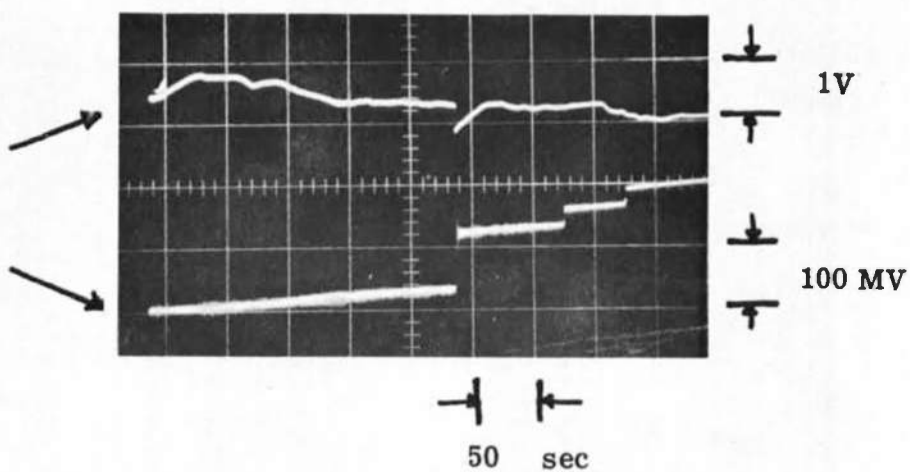


FIGURE 30

(PM #1)

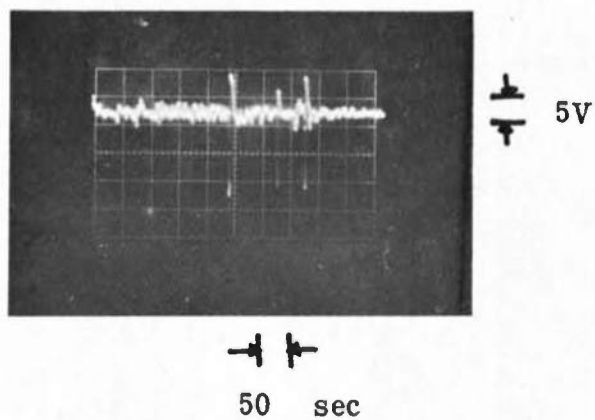
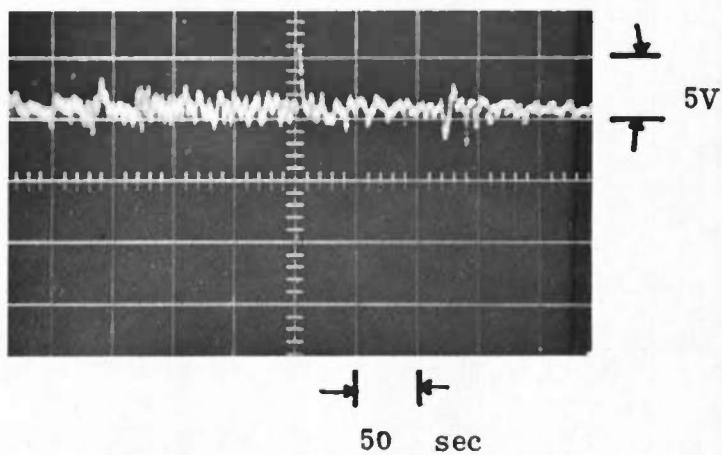


FIGURE 31

(PM #2)



OSCILLOGRAMS FROM TUNNEL TEST #305

APPENDIX I

CALCULATION OF WORKING EQUATIONS

In order to facilitate the determination of the electron concentration from the raw data, it is convenient to write the expression for Ne as,

$$Ne = \frac{\phi/\Omega}{\sigma_{eff} V_{scat} \phi_0/CM^2} \quad (1)$$

where ϕ = number of photons
 Ω = solid angle of detector
 σ_{eff} = effective cross section for Thomson scattering
 V_{scat} = scattering volume as seen by the detector
 ϕ_0/CM^2 = photon density of laser beam at the scattering volume

In order to use equation (1), σ_{eff} was determined by taking appropriate values of Te and Ne and computing the return to channels #1 and #2 over the $(\sin)^2$ and $(\cos)^2$ curve. These were summed and σ_{eff} computed from

$$\sigma_{eff} = \frac{\sum_{computer}}{Ne} \quad (2)$$

This was done for the expected range of temperatures and concentrations and averaged to $\pm 10\%$. The result of these efforts produced a $\sigma_{eff} = 3.25 \times 10^{-26} cm^2$ for both the tunnel and arc experiments. The remaining quantities in equation (1) were then computed separately for the arc and tunnel experiments from the geometry of the experimental arrangement.

For the arc runs, with $\theta = 150^\circ$, the scattering volume is an elliptical cylinder bounded by the diameter of the laser beam and the height and width of the detector slit. For most of the arc runs an entrance slit of $50\mu \times 1.0$ mm was used. Hence the semi-axes of the ellipse are $1/2$ mm by 2 mm, the 2 mm being determined by the size of the laser beam (2 mm) and $\theta = 150^\circ$. The thickness of the ellipse being the slit width. With these values the scattering volume becomes $V_{scat} = 1.56 \times 10^{-4} cm^3$.

The photon density was obtained by computing the area of the laser beam and using the fact that there are 3.47×10^{18} ϕ /joule at 6943 A. The solid angle for the system was 1.23×10^{-2} with the resultant expression,

$$N_e = \frac{\phi \text{ (measured)}}{J \text{ (measured)}} 3.60 \times 10^{10} \text{ (cm}^{-3}\text{)} \quad (3)$$

For the tunnel runs, the procedure was the same except the working angle $\theta = 173^\circ$ with the resultant expression,

$$N_e = \frac{\phi \text{ (measured)}}{J \text{ (measured)}} 6.80 \times 10^9 \text{ (cm}^{-3}\text{)} \quad (4)$$

The J in these equations must be expressed in joules.

The uncertainty in these working equations is in the diverging of the laser energy over the laser beam area. In both cases it was assumed that the measured energy was over a 1.5 mm diameter rather than 2 mm. This was justified on the basis of a modified Gaussian distribution of energy of the laser beam.

APPENDIX II

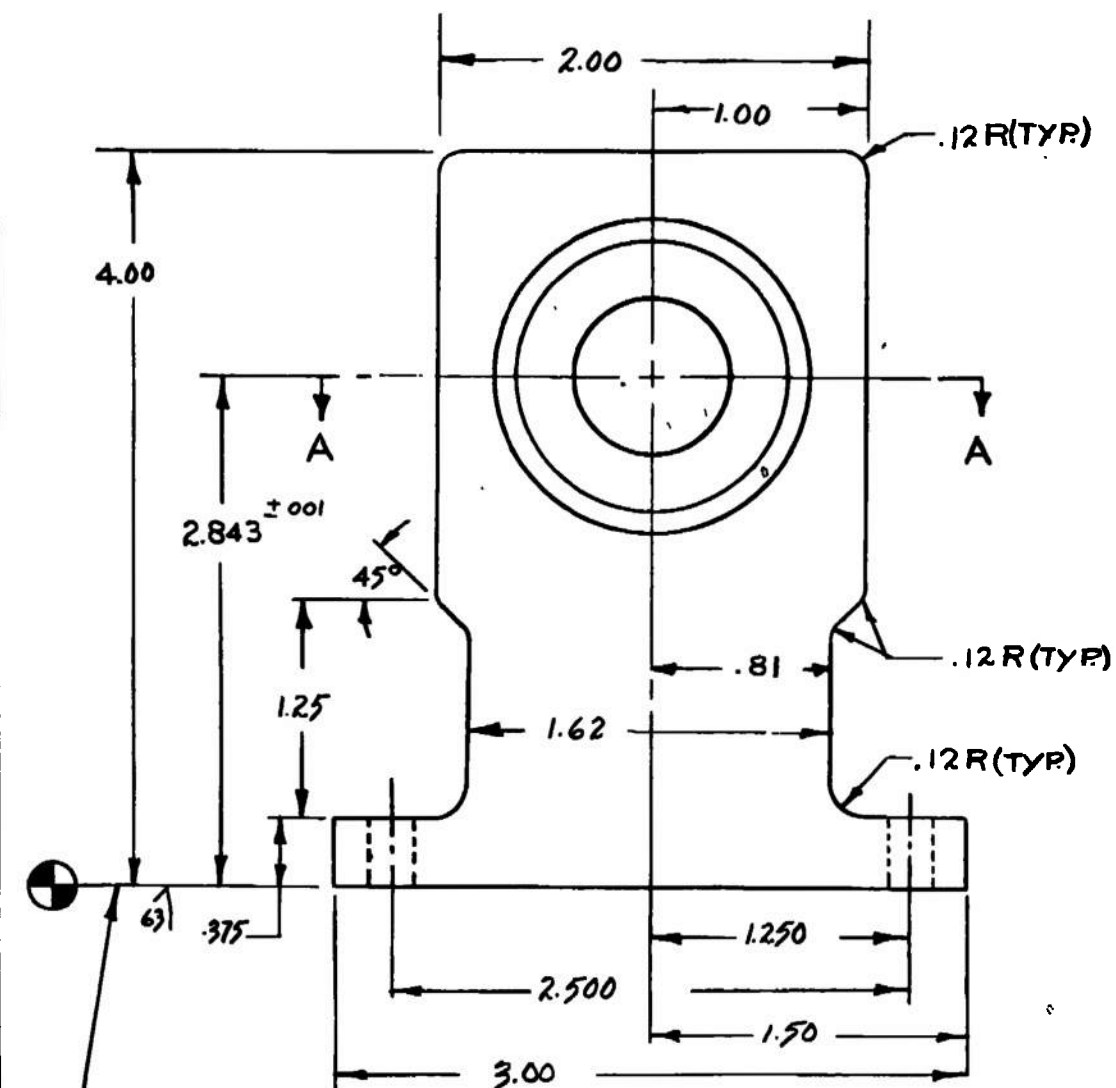
ENGINEERING DESIGN DATA FOR DETECTOR

SIZE B 56160 B 465

SHEET REV

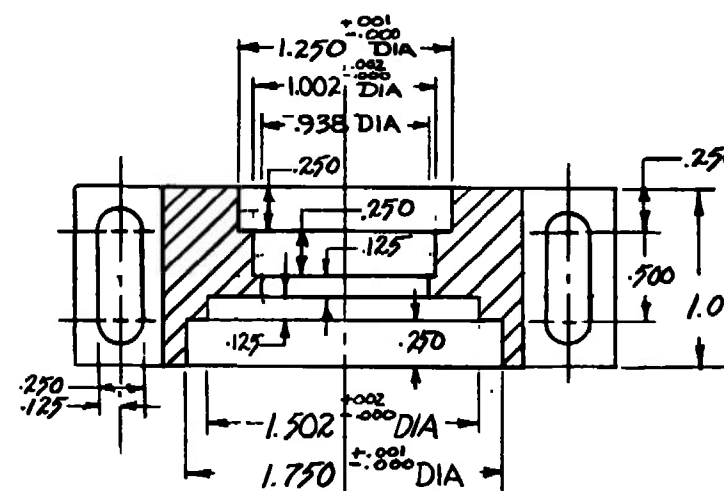
REVISIONS

ZONE	LTR	DESCRIPTION	DATE	APPROVED

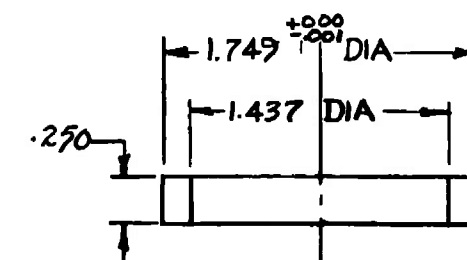


SURFACE PARALLEL TO BORED
HOLES WITHIN .002 TIR

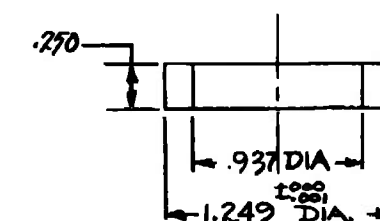
① LENS HOLDER
MAT'L: ALUM ALLOY



SECTION A-A



② RETAINER
MAT'L: TEXTOLITE



③ RETAINER
MAT'L: TEXTOLITE

UNLESS OTHERWISE SPECIFIED
DIMENSIONS ARE IN INCHES.
TOLERANCES ON:

FRACTIONS DECIMALS ANGLES
± .005 ±

2 PL. DEC ±.010 63/

ALL SURFACES

MATL.

SIGNATURES

DRAWN DE DOMINKUS 15 10 68

CHECKED

ISSUED 15 10 68

ENGRG 15 10 68

MFG

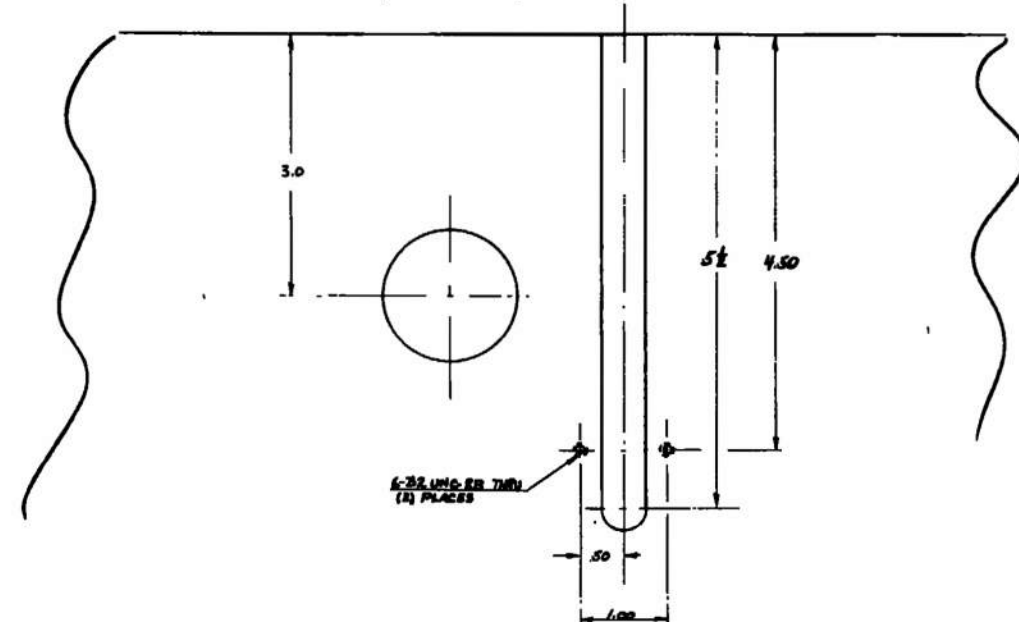
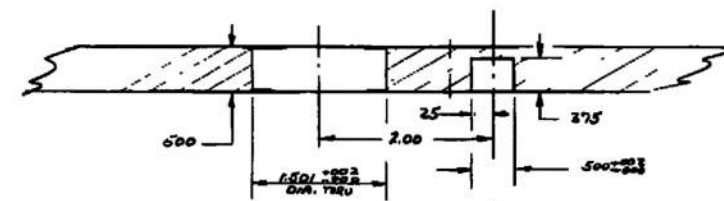
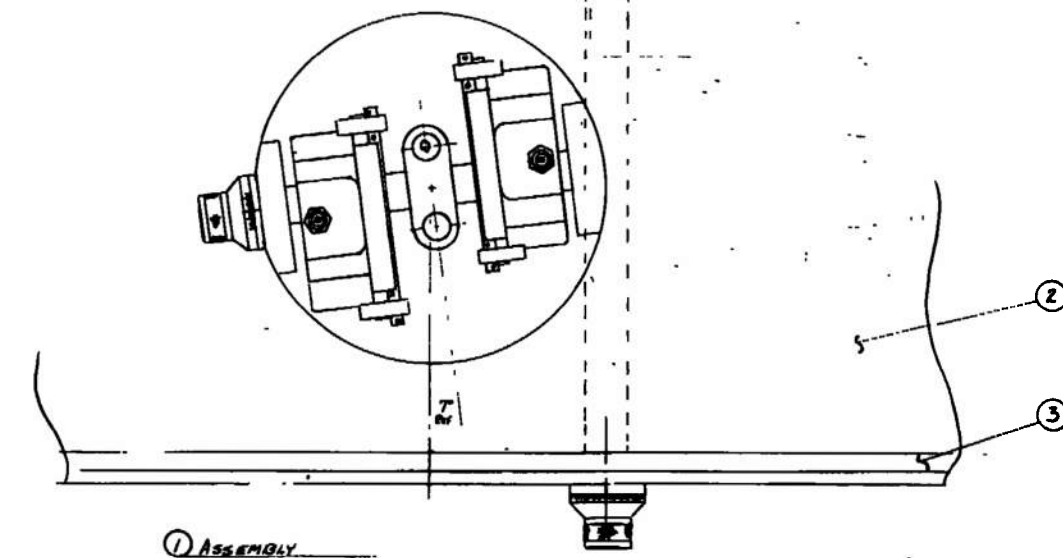
MATLS

LENS HOLDER DETAILS

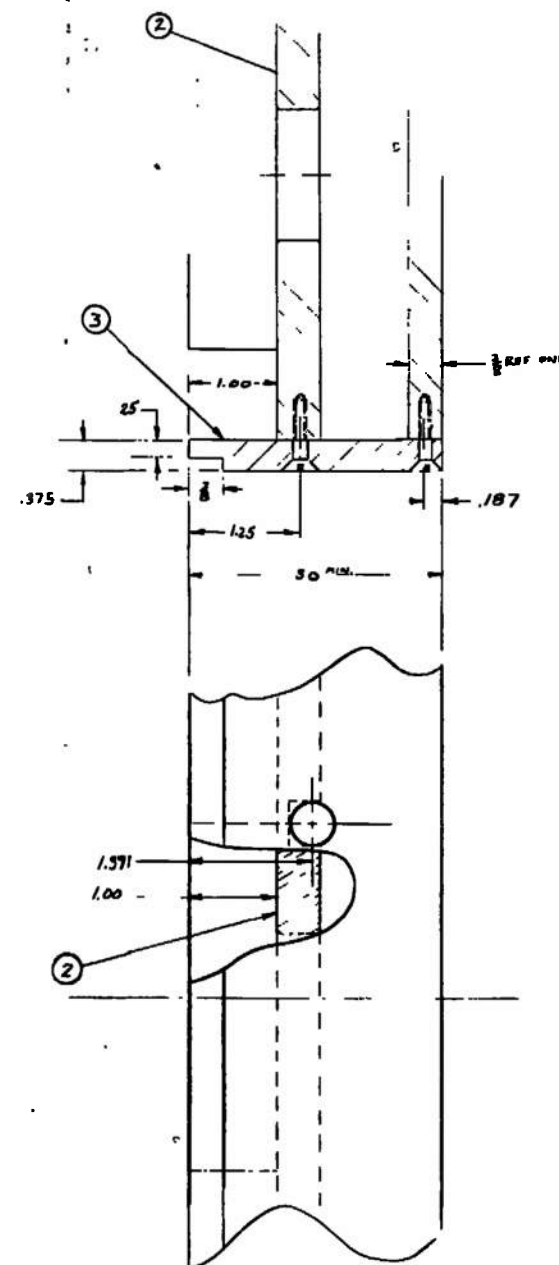
SIZE B CODE IDENT NO. 56160 B 465

SCALE FULL SHEET

REVISIONS			
ZONE	LTR	DESCRIPTION	DATE



② BOTTOM VIEW BASE PLATE
Mtl 2 (6061-T6 ALUM PLATE)



UNLESS OTHERWISE SPECIFIED
DIMENSIONS ARE IN INCHES—
TOLERANCES ON: HOLE & HOLE
2-PLACE DECIMALS $\pm .010$ ALL
3-PLACE DECIMALS $\pm .005$ SURF
ANGLES $\pm 4^\circ$
FRACTIONS $\pm .005$ 63 ✓

MATERIAL—

DESIGNED	2	8	68
ENGINEER	72	4	68
DATE			

SIZE		CODE IDENT NO	
D		56160 D458	
SCALE		SHEET	

BASE PLATE DETAILS
DUAL MIRROR GONIOMETER

4

FOLD
↓

3

2

SIZE
B

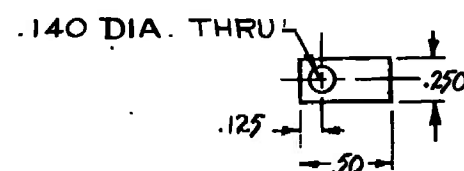
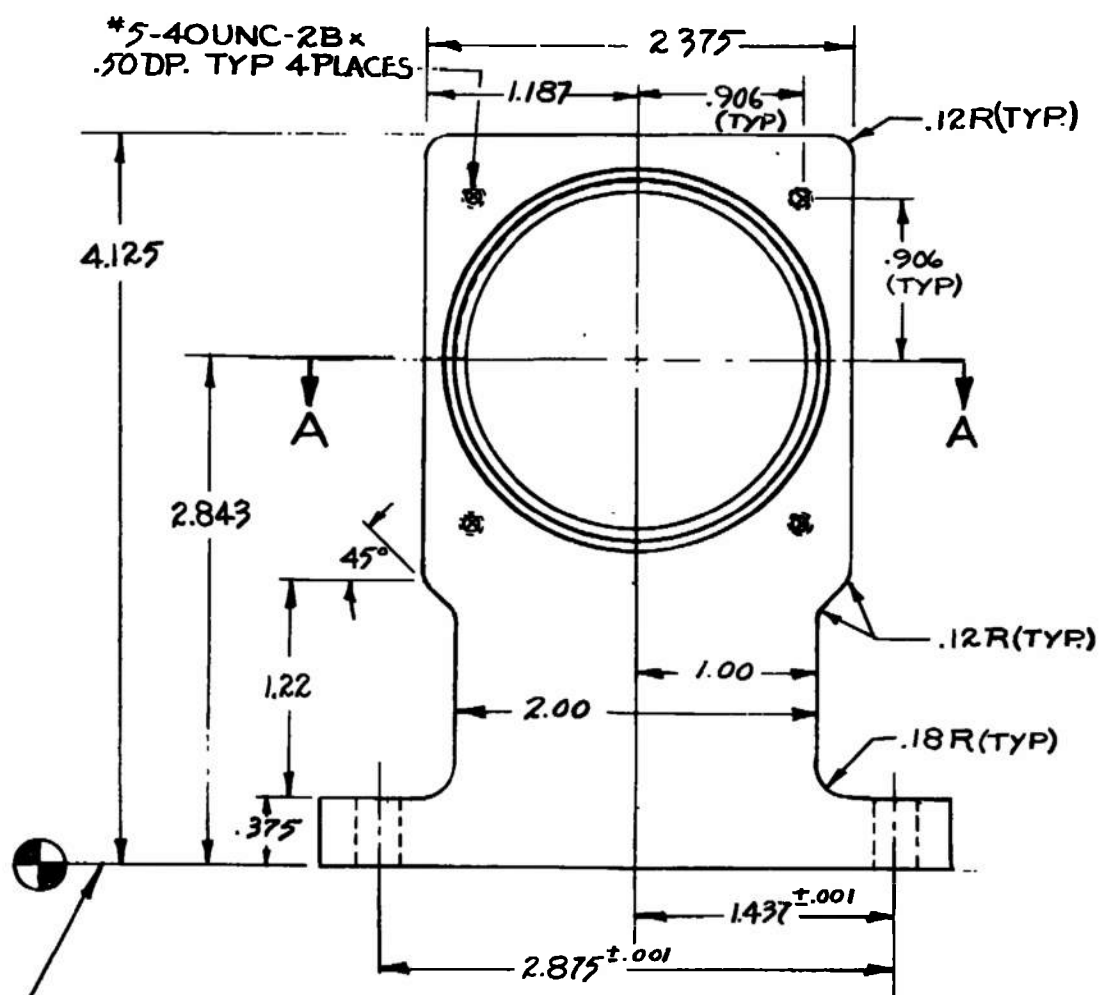
56160B459

SHEET

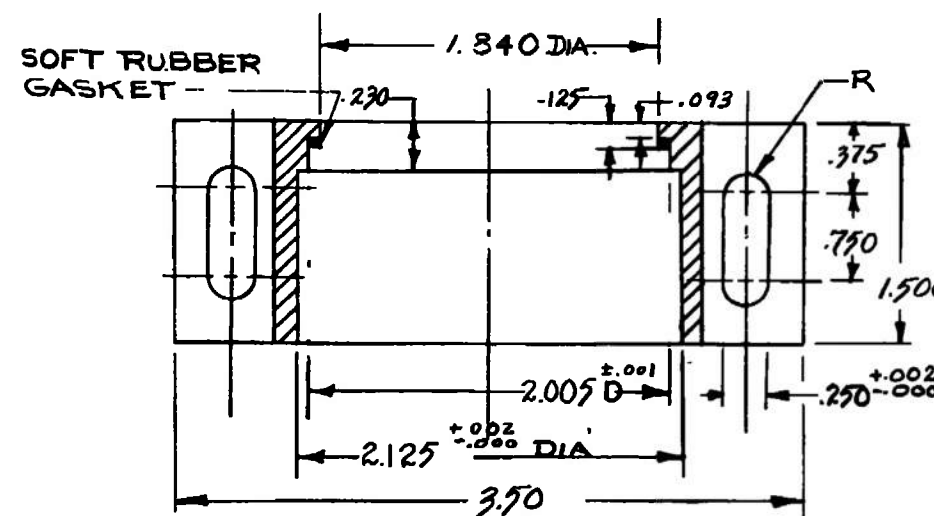
REV

REVISIONS

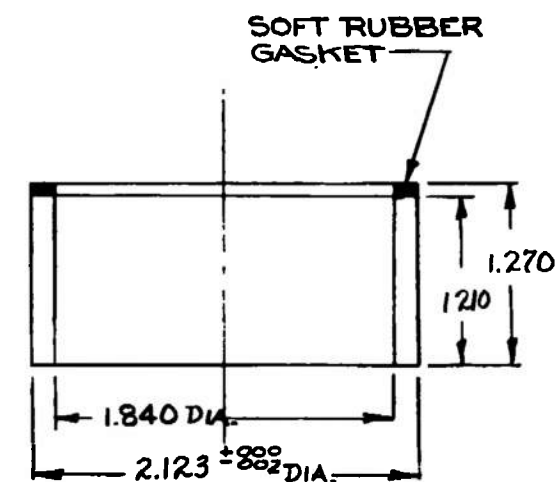
ZONE	LTR	DESCRIPTION	DATE	APPROVED
------	-----	-------------	------	----------

TAB
4 REQ'D - 1/8 THK.

LENS HOLDER



SECTION A-A



SLEEVE ASS'Y

UNLESS OTHERWISE SPECIFIED
DIMENSIONS ARE IN INCHES.
TOLERANCES ON:

FRACTIONS	DECIMALS	ANGLES
±	±.005	±

ALL SURFACES
MATL. ALUM ALLOY
2024-T6

CHECKED

ISSUED

ENGRG

MFG

MATLS

LENS HOLDER DETAILS

SIZE CODE IDENT NO.

B

56160B459

SCALE FULL

SHEET

DIST
TO

5

4

FOLD
↑

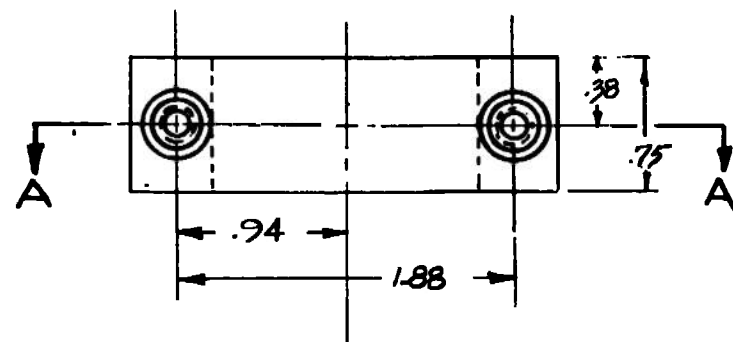
3

2

51

REVISIONS

ZONE	LTR	DESCRIPTION	DATE	APPROVED
------	-----	-------------	------	----------



TAP PT. 1 $\frac{1}{4}$ -20 UNC-2B
x .38 DP; PT. 2 DRILL
THRU .281 DIA, C'BORE
.40 DIA x .38 DP. 2 PL'S.

⑤ $\frac{1}{4}$ -20 UNC-2B $\times \frac{7}{8}$ LG
SOCK HD BOLT (2)

② CLAMP

.25R (TYP)

- #10-24 UNC-2B THRU

④ CYLINDER

③ PRISM HOLDER
ALL DIM. SAME AS PTS 1 & 2
EXCEPT AS NOTED

← SURFACE PARALLEL TO BORED
HOLE WITHIN .002 TIR

SECTION A-A

**UNLESS OTHERWISE SPECIFIED
DIMENSIONS ARE IN INCHES.
TOLERANCES ON:**

FRACTIONS ^{3 FL} DECIMALS ANGLES

FRACTIONS	DECIMALS	ANGLES
†	†	†

1911 Dec 11

2 PL DEC 1.010 63

ALL SURFACES ✓

MATL-

MAT'L: ALUM

MAT L: ALUM

ALLOY 2024-T6

ANODIZE BLACK

ISSUED 82 12/10/11

ISSUED	16	10	6
ENTERED			

ENERG	25	16	10	6
-------	----	----	----	---

NFB			
------------	--	--	--

MATLS			
--------------	--	--	--

[illegible]

LASER HOLDER DETAILS

SIZE	CODE IDENT NO.	56160B466
------	----------------	-----------

B		70100 D-80

SCALE *FULL* | **SHEET**

TO

1
2
3
4
5
6
7
8
9
10
11
12
13
14
15
16
17
18
19
20
21
22
23
24
25
26
27
28
29
30
31
32
33
34
35
36
37
38
39
40
41
42
43
44
45
46
47
48
49
50
51
52
53
54
55
56
57
58
59
60
61
62
63
64
65
66
67
68
69
70
71
72
73
74
75
76
77
78
79
80
81
82
83
84
85
86
87
88
89
90
91
92
93
94
95
96
97
98
99
100
101
102
103
104
105
106
107
108
109
110
111
112
113
114
115
116
117
118
119
120
121
122
123
124
125
126
127
128
129
130
131
132
133
134
135
136
137
138
139
140
141
142
143
144
145
146
147
148
149
150
151
152
153
154
155
156
157
158
159
160
161
162
163
164
165
166
167
168
169
170
171
172
173
174
175
176
177
178
179
180
181
182
183
184
185
186
187
188
189
190
191
192
193
194
195
196
197
198
199
200
201
202
203
204
205
206
207
208
209
210
211
212
213
214
215
216
217
218
219
220
221
222
223
224
225
226
227
228
229
230
231
232
233
234
235
236
237
238
239
240
241
242
243
244
245
246
247
248
249
250
251
252
253
254
255
256
257
258
259
260
261
262
263
264
265
266
267
268
269
270
271
272
273
274
275
276
277
278
279
280
281
282
283
284
285
286
287
288
289
290
291
292
293
294
295
296
297
298
299
300
301
302
303
304
305
306
307
308
309
310
311
312
313
314
315
316
317
318
319
320
321
322
323
324
325
326
327
328
329
330
331
332
333
334
335
336
337
338
339
340
341
342
343
344
345
346
347
348
349
350
351
352
353
354
355
356
357
358
359
360
361
362
363
364
365
366
367
368
369
370
371
372
373
374
375
376
377
378
379
380
381
382
383
384
385
386
387
388
389
390
391
392
393
394
395
396
397
398
399
400
401
402
403
404
405
406
407
408
409
410
411
412
413
414
415
416
417
418
419
420
421
422
423
424
425
426
427
428
429
430
431
432
433
434
435
436
437
438
439
440
441
442
443
444
445
446
447
448
449
450
451
452
453
454
455
456
457
458
459
460
461
462
463
464
465
466
467
468
469
470
471
472
473
474
475
476
477
478
479
480
481
482
483
484
485
486
487
488
489
490
491
492
493
494
495
496
497
498
499
500
501
502
503
504
505
506
507
508
509
510
511
512
513
514
515
516
517
518
519
520
521
522
523
524
525
526
527
528
529
530
531
532
533
534
535
536
537
538
539
540
541
542
543
544
545
546
547
548
549
550
551
552
553
554
555
556
557
558
559
560
561
562
563
564
565
566
567
568
569
570
571
572
573
574
575
576
577
578
579
580
581
582
583
584
585
586
587
588
589
590
591
592
593
594
595
596
597
598
599
600
601
602
603
604
605
606
607
608
609
610
611
612
613
614
615
616
617
618
619
620
621
622
623
624
625
626
627
628
629
630
631
632
633
634
635
636
637
638
639
640
641
642
643
644
645
646
647
648
649
650
651
652
653
654
655
656
657
658
659
660
661
662
663
664
665
666
667
668
669
670
671
672
673
674
675
676
677
678
679
680
681
682
683
684
685
686
687
688
689
690
691
692
693
694
695
696
697
698
699
700
701
702
703
704
705
706
707
708
709
710
711
712
713
714
715
716
717
718
719
720
721
722
723
724
725
726
727
728
729
730
731
732
733
734
735
736
737
738
739
740
741
742
743
744
745
746
747
748
749
750
751
752
753
754
755
756
757
758
759
760
761
762
763
764
765
766
767
768
769
770
771
772
773
774
775
776
777
778
779
780
781
782
783
784
785
786
787
788
789
790
791
792
793
794
795
796
797
798
799
800
801
802
803
804
805
806
807
808
809
810
811
812
813
814
815
816
817
818
819
820
821
822
823
824
825
826
827
828
829
830
831
832
833
834
835
836
837
838
839
840
84

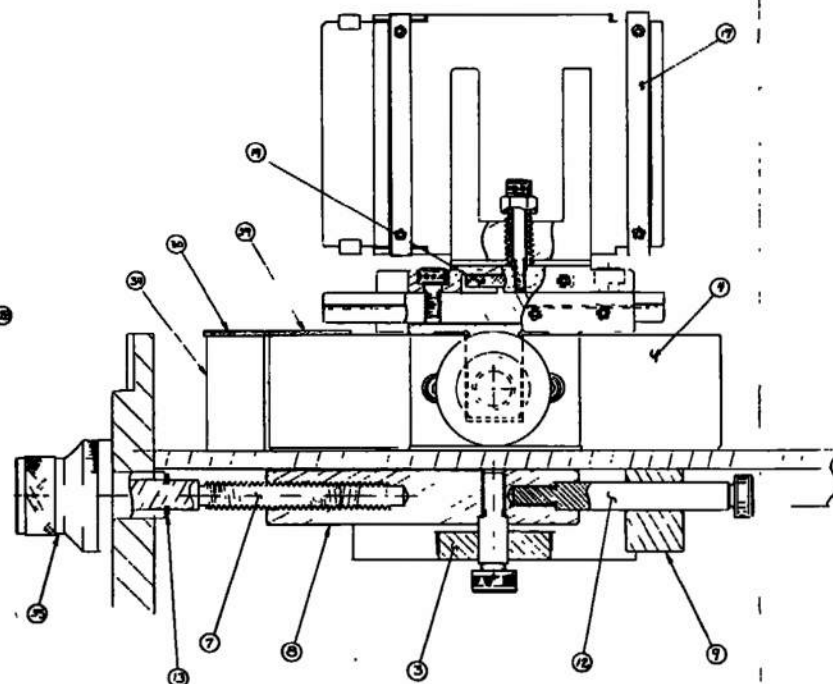
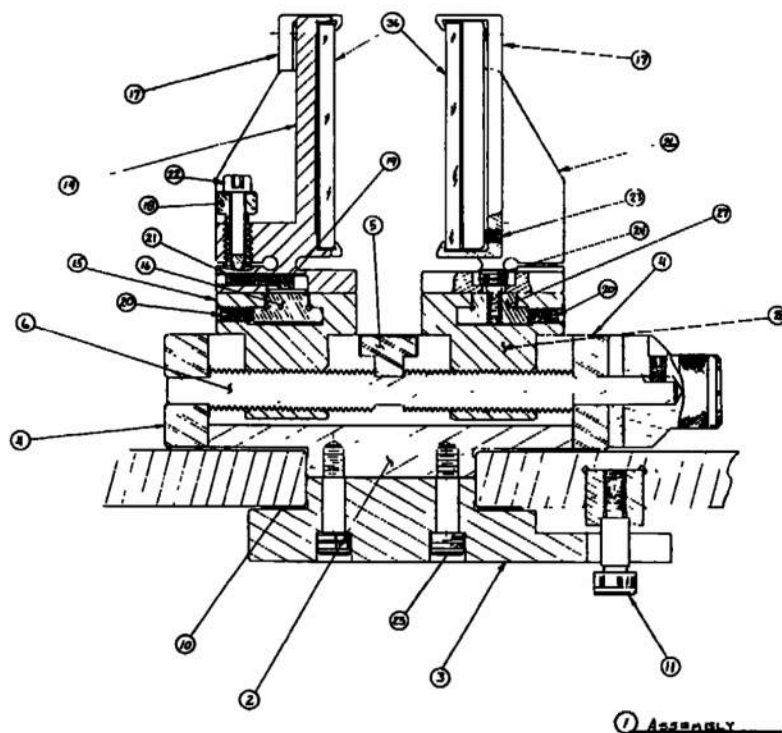
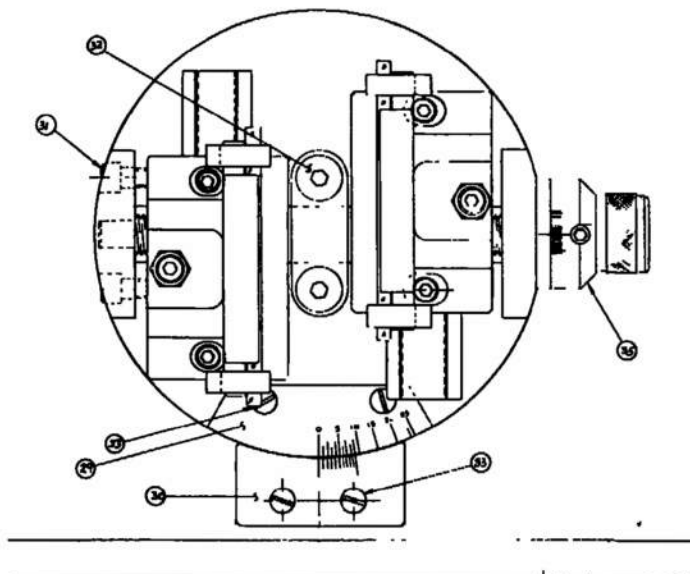


UNLESS OTHERWISE SPECIFIED
DIMENSIONS ARE IN INCHES.
TOLERANCES ON:

FRACTIONS	DECIMALS	ANGLES
\pm	$\pm .005$	\pm
2 PL DEC $\pm .010$		63
ALL SURFACES		∇

MATL- ALUM JIG
PLATE

FRONT PLATE		
LASER PROBE		
SIZE B	CODE IDENT NO.	56160B468
SCALE = 1/2		SHEET



1 Assembly

	37			
	36	FRONT VIEW	MIRROR	PLATE
	35	FRONT VIEW, 1/4" X		

IDENT. NO. NO.		DESCRIPTION		MATERIAL	
56160E 427		DUAL MIRROR GONIOMETER		STEEL	

4

3

2

SIZE

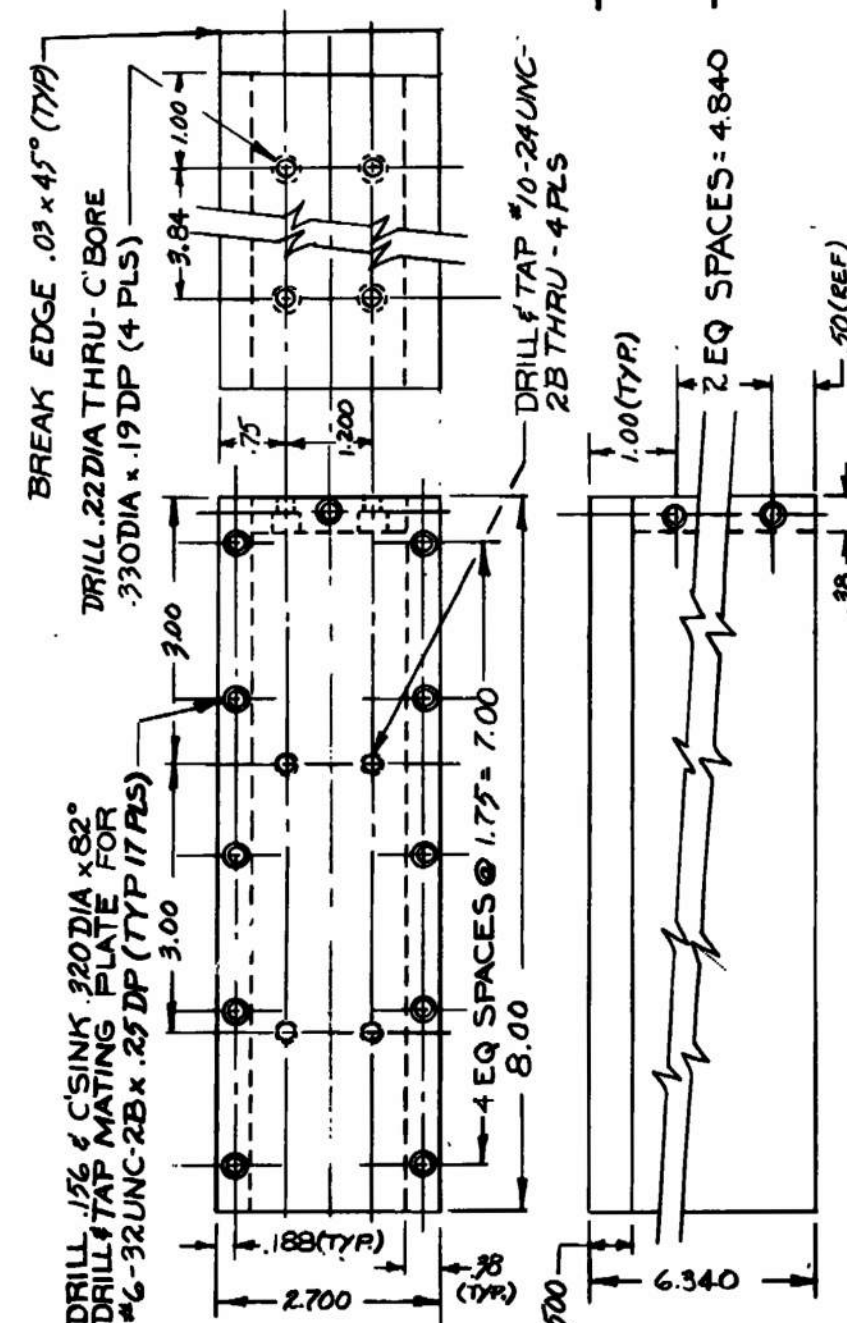
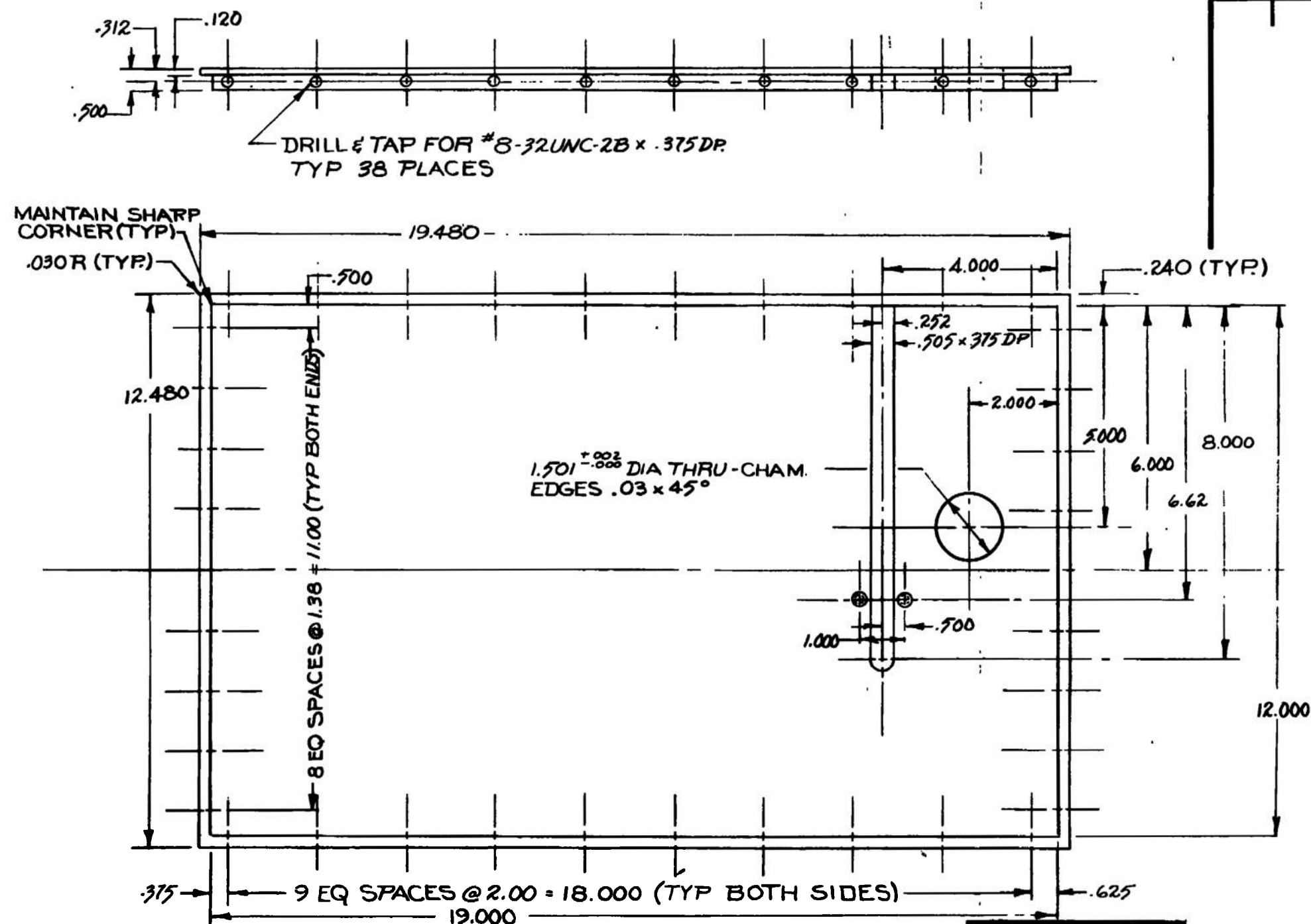
56160B467

SHEET

REV

REVISIONS

ZONE	LTR	DESCRIPTION	DATE	APPROVED



① BASE PLATE
SCALE 1/2 = 1

UNLESS OTHERWISE SPECIFIED
DIMENSIONS ARE IN INCHES.
TOLERANCES ON:

FRACTIONS DECIMALS ANGLES
± ± .005 ± 1/2°

2 PL DEC = ± .010

ALL SURFACES

MATL

ALUM ALLOY

CHECKED

ISSUED

ENGRG

MFG

MATLS

BASE PLATE
LASER PROBE

SIZE CODE IDENT NO.

B

56160B467

SCALE 1/2

SHEET

REVISIONS

DRILL .187 DIA THRU - C SINK .97 DIA
x .82" TYP 14 PLACES

.281 DIA THRU —
PART NO 1 ONLY

- 9 SPACES @ 2.00 = 18.00

312—
(REF)

-12 SPACES @ 2.00 = 24.00

-19.250

- 25.00

-DRILL & TAP #6-32UNC-2B x.31 DP -13
PLACES ON CENTER

-DRILL & TAP FOR
#8-32UNC-2B x .31 DP

- ① SIDE PLATE - LEFT
- ② SIDE PLATE - RIGHT
SAME AS PT 1 BUT OPP HAND
& DELETE .281 DIA HOLE

**UNLESS OTHERWISE SPECIFIED
DIMENSIONS ARE IN INCHES.
TOLERANCES ON:**

FRACTIONS ^{3 PL.} **DECIMALS** **ANGLES**

2 P1 DEC ± 010

ALL SURFACES

MATL.
ALUM. JIG PLATE

ISSUED	5	11	6
ENGRG	5	11	6
MFG			
MATLS			

SIDE PLATE
LASER PROBE

SIZE B	CODE IDENT NO.	56160B472
-----------	----------------	-----------

SCALE 1/2"		SHEET
------------	--	-------

FORM 902-F (8-67) PRINTED IN U. S. A.

TO:

4

FOLD

3

2

SIZE B 56160B480

SHEET

REV

REVISIONS

ZONE	LTR	DESCRIPTION	DATE	APPROVED

D

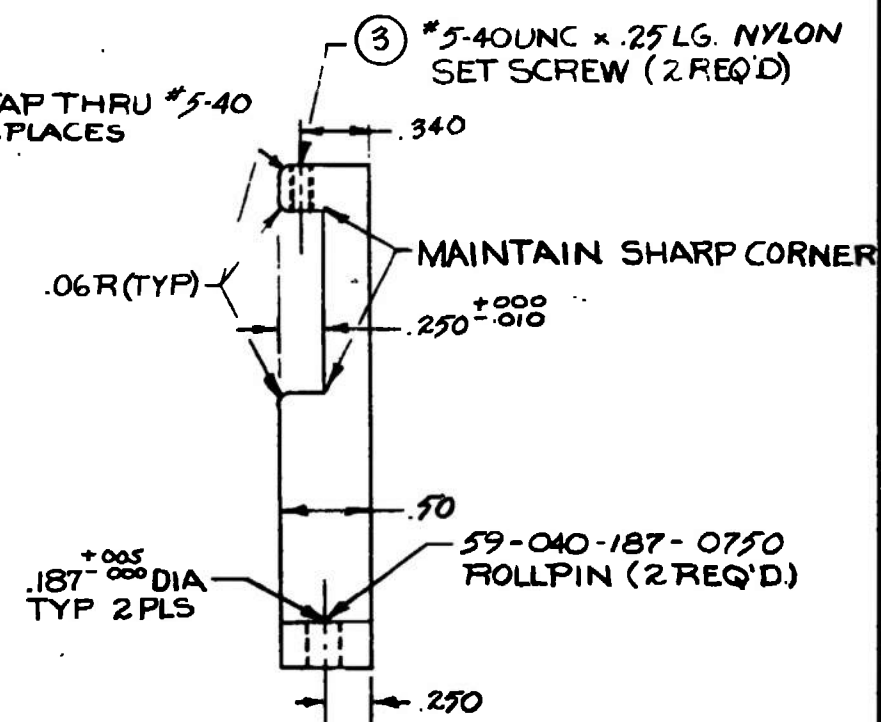
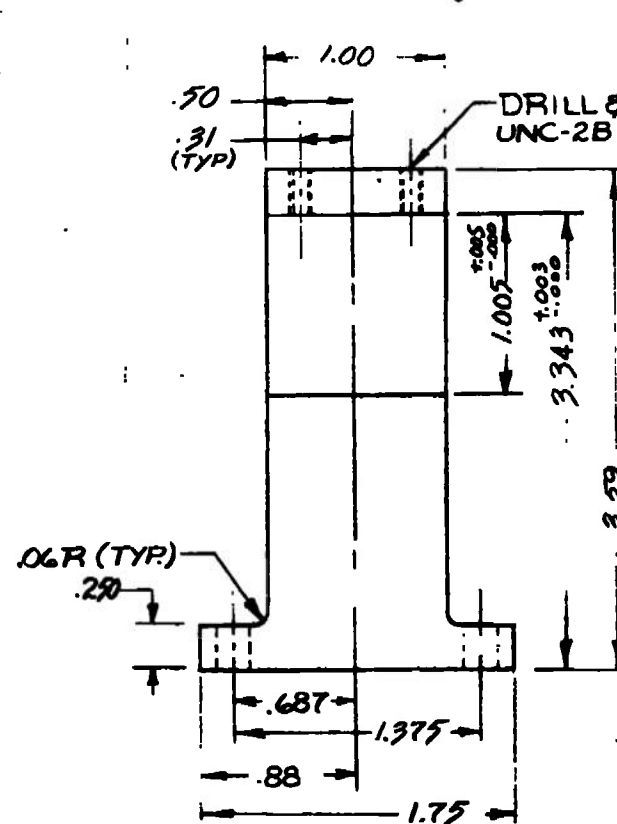
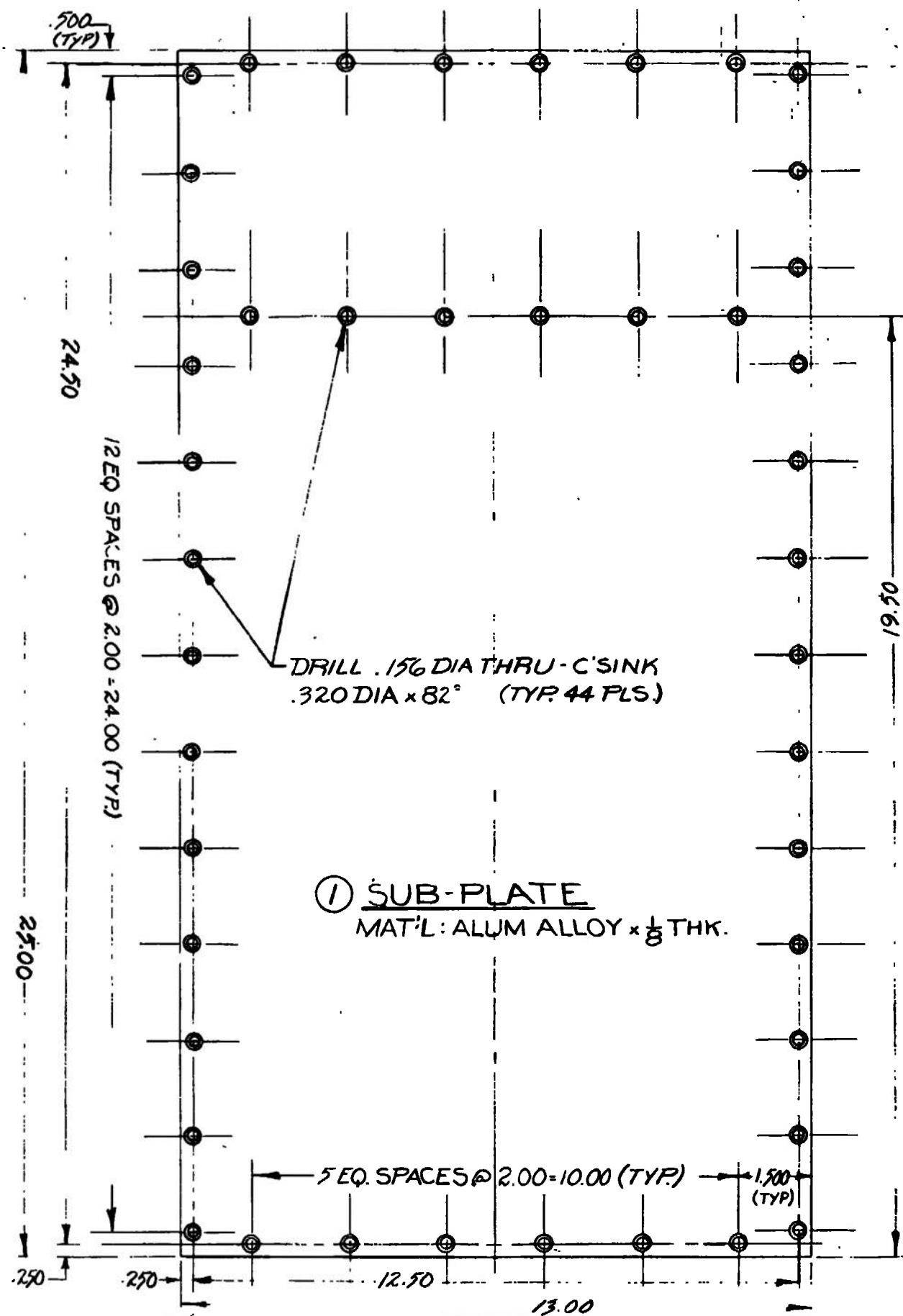
C

B

A

A

FN 902-F (8-67) PRINTED IN U.S.A.

UNLESS OTHERWISE SPECIFIED
DIMENSIONS ARE IN INCHES.
TOLERANCES ON:FRACTIONS DECIMALS ANGLES
± .005 ±

2 PL DEC = ± .010

ALL SURFACES

MAT'L

BLACK ANODIZE

DI
CH

ISSUED

ENGRD

MFG

MATLS

13

11

68

13

11

68

MISC. DETAILS
LASER PROBE

SIZE

B

CODE IDENT NO.

56160B480

SCALE 3/8" = 1"

SHEET

DIST

TO

D

C

B

A

A

4

FOLD

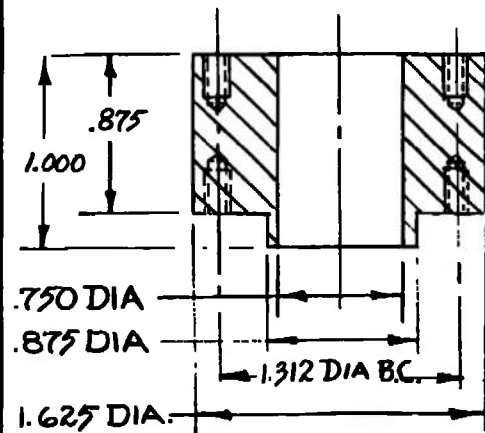
3

2

SIZE
B

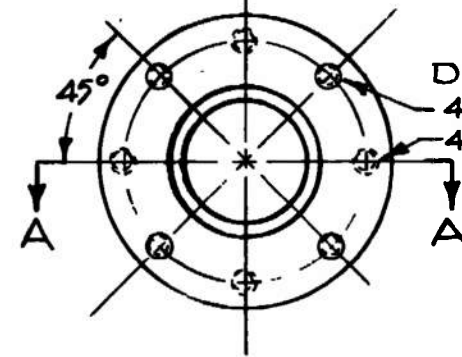
REVISIONS

ZONE	LTR	DESCRIPTION	DATE	APPROVED



SECTION A-A

② CENTER ADAPTOR



DRILL & TAP #5-40UNC-2B x .25 DP
4 HOLES NEAR SIDE
4 HOLES FAR SIDE

NEAR SIDE

④ ADAPTOR

ALL DIM FOR PT 3
APPLY EXCEPT AS NOTED



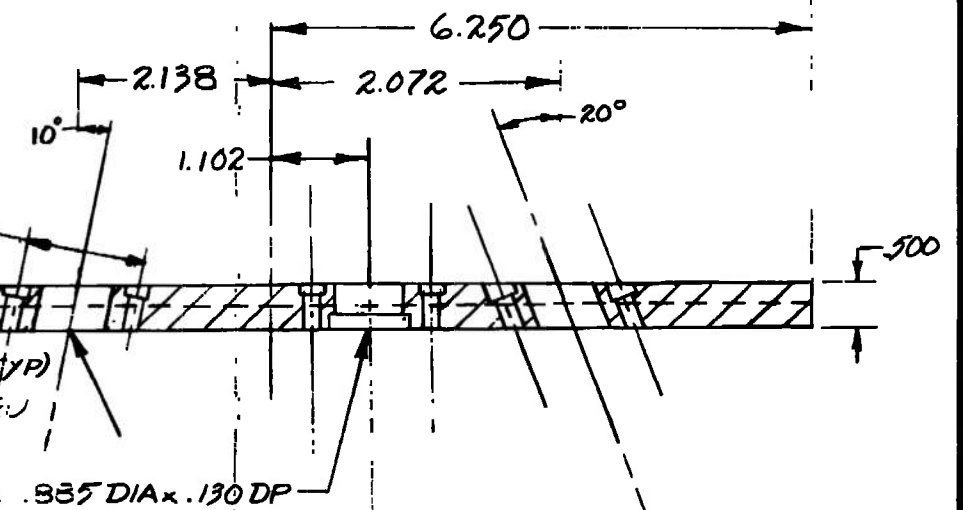
DRILL .156 DIA THRU - C'BORE
.234 DIA x .140 DP - 4 HOLES
ON A 1.312 DIA B.C. (3 PLS)

BREAK EDGE .03 (TYP)
.750 DIA BORE THRU
TYP 3 PLS

C'BORE .885 DIA x .130 DP

SECTION B-B

① REAR PLATE



SEE PT 2 FOR TAPPED HOLE PATTERN

NEAR SIDE

③ ADAPTOR

UNLESS OTHERWISE SPECIFIED
DIMENSIONS ARE IN INCHES.
TOLERANCES ON:

FRACTIONS DECIMALS ANGLES
± .005 ± .005 ± .5°

2 PL DEC ± .010

ALL SURFACES

MATL.

ALUM ALLOY

CHECKED				
ISSUED	7	11	68	
ENGRG	7	11	68	
MFG				
MATLS				

REAR PLATE
LASER PROBE

SIZE CODE IDENT NO.

B

56160B473

SCALE 1/2" = 1"

SHEET

APPENDIX III

COMPUTER PROGRAM LISTING AND RESULTS

PROGRAM NOTES

Four subroutines are called which are not herein listed:

- a. * EPMDE (KODE)
- and b. ** CLCINT (IND, DX, FX, TEMP)
- c. ** TNT1 (X, NTAB, XTAB, YTAB, N, IERR)
- d. *** EXIT

The purpose of (a.) is to suppress printing of error messages of the form:

```

DIV CHECK AT XXXXX      (divide by zero)
EXP OVERFLO AT XXXXX    (number too big)
EXP UNDERFLO AT XXXXX  (number too small)

```

The purpose of (b.) is to perform integrations. Subroutine (FORTRAN function subroutine) uses Simpson's rule.

The purpose of (c.) is to interpolate linearly by Lagrange's formula.

The purpose of (d.) is to terminate execution of the program.

*Reference: GE Space Div. "Programmer's Reference Manual"
RM1001, page VI-16

**Reference: GE Space Div. "Engineering & Scientific Computer
Library" manual

***Reference: GE Information Systems "GE-600 Line FORTRAN IV",
CPB-1006G, Page 70

48224 C1 DB-1C-70 18,082 PROGRAM TO GET INTEGRAL OF R OVER X(LAM)

PAGE 1

```

      FROM A PROGRAM BY ANG
1  CROFX      PROGRAM TO GET INTEGRAL OF R OVER X(LAM)
2  C          FROM A PROGRAM BY ANG
3
4  COMMON X(SDC1), PX(SDC1), PY(S1)
5  COMMON /CURVE/ CLANC(100), RCOB(100), CLAMB(70), RBSIN(70)
6  DIMENSION T1(5), T2(5)
7
8  2 FORMAT ( 2H INTEGRAL CALCULATED TO X=,1PE10.3,2H, OVER COS SARD
9  1 CURVE,1PE15.6,2H, OVER SIN SARD CURVE,1PE15.6,/ 2H RPOF,
10  2 1PE15.6 )
11  5 FORMAT (1H 3(1PE14.7,2X))
12  6 FORMAT (2I4)
13  8 FORMAT (1H 5(1PE14.7,2X))
14  900 FORMAT (9F8.0)
15  901 FORMAT (F8.0,E12.2,F8.0)
16
17  NAMELIST/ROFX/ ANG, TE, ALPHA, BETA
18
19  CALL EPNDE ( 7 )
20  CALL CALC
21
22  SPH1=(3.1415926*0.5
23  THETA = 170.0
24  RTTHETA=.017832*THETA
25
26  READ (5,4) NT, NAL
27  READ(5,500) ALPHA1, DALPH
28
29  DO 110 N=1,NT
30  READ (5,501) TE
31
32  DO 110 NALF = 1, NAL
33  ALPHALPHA1 = FLOAT(NALF-1)*DALPH
34  DE= .2545 *DE*0.5*BSIN(RTHETA/2.)
35  ANG = 2.411E13 * ALPHALPHA1*ALPHA1*DE
36  ALPHALPHA1=2
37  ALPHALPHA1 = 0.003.1415927
38  BETA = ALPHA / SQR(1.0+ALPHA2)
39  BETA2= BETA * BETA
40  BETA4= BETA2* BETA2 * 3.1415927
41  DEL = 0.0
42
43  WRITE ( 6, ROFX )
44
45  DO 10 I = 1, SDC1
46  DL = X(I) * DE
47  IF (-DL .LT. CLANC(1) ) GO TO 11
48  KRX(I)=KX(I)
49  Y = 225.7 * X(I)
50  Y2 = Y * Y

```

48224 C1 CB-1C-7C 18.982 PROGRAM TO GET INTEGRAL OF R OVER X(LAM)

PAGE 2

```

      FROM A PROGRAM BY AMS
31      RA=EXP(-X2)/((1.+ALPH+B-ALPH*EXP(1))**B+ALPH+1)*EXP(-2.*X2) 36
32      RB = C,C 37
33      IF ( 1 .GT. 51 ) GO TO 9 38
34      RB = EXP(-Y2)/((1.+BETAB-BETAB*PY(1))**B+BETA+1)*EXP(-2.*Y2) 41
35      R = (7.941E-2*RA/RPHI) * GRA + BETA*RB 42
36
37      CALL INTERP ( X(1), DE, R, RC, RB ) 43
38      RCI = CLCINT ( 1, DEL, RC, Y1 ) 44
39      RSI = CLCINT ( 1, DEL, RB, Y2 ) 45
40      DEL = C,D1 46
41
42      10 CONTINUE 47
43
44      11 CONTINUE 48
45      RHO = RSI / RCI 49
46      WRITE ( 6, 2 ) X(1), RCI, RSI, RHO 50
47
48      110 CONTINUE 54
49      CALL EXIT 57
50      END 58

```

```

*****
78 DOES NOT APPEAR IN READ, DATA, COMMON OR LEFT OF EQUALS (=)

```

```

*****

```

23820 WORDS OF MEMORY USED BY THIS COMPILATION

42224 G3 08-10-70 16.028 SUBROUTINE CALC FOR ROPE PROG.

PAGE 1

```

      FROM A PROGRAM BY AMS
1  CCALC      SUBROUTINE CALC FOR ROPE PROG.
2  C          FROM A PROGRAM BY AMS
3
4  COMMON X(SCC1), PX(SCC1), PY(S1)
5  DIMENSION XX(S1), PXX(S1)
6  DIMENSION R(8),U(8),UINT(8),F(SCC1),AINT(8)
7  R(1)=.08061427
8  R(2)=.11119082
9  R(3)=.19885333
10 R(4)=.18134188
11 R(5)=.18134188
12 R(6)=.19885333
13 R(7)=.11119082
14 R(8)=.08061427
15 U(1)=-.48014493
16 U(2)=-.38833323
17 U(3)=-.28278821
18 U(4)=-.08171732
19 U(5)=.08171732
20 U(6)=.28278821
21 U(7)=.38833323
22 U(8)=.48014493
23 DO 10 N=1,8
24 10 UINT(N)=.014U(N)
25 X(1)=0.
26 PX(1)=0.
27 F(1)=0.
28 DO 100 I=2,SCC1
29 X(I)=X(I-1)+.01
30 C=(X(I)+X(I-1))/2.
31 DO 30 N=1,8
32 D=(UINT(N)+C)*R
33 AINT(N)=X(N)*EXP(D)
34 SUM=0.
35 DO 30 N=1,8
36 SUM=SUM+AINT(N)
37 F(I)=SUM*.01+F(I-1)
38 100 PX(I)=F(I)*2.*X(I)*EXP(-X(I)*X(I))
39 DO 103 I=802,SCC1
40 X(I)=X(I-1)+.01
41 K2=X(I)*2
42 103 PX(I)=1.+(1.+1.5/X*2+3.75/X(I)*4)/(2.*X(2))
43 XX(1)=0.
44 PXX(1)=0.
45 F(1)=0.
46 PY(1)=0.0
47 Y=0.0
48 DO 110 I=2,81
49 Y=Y+.2257
50 POB=Y/.01+1.0

```

42224 L3 10-10-70 16,028 SUBROUTINE CALL FOR HOFX PROG.

2

	FROM A PROGRAM BY AMB	
51	NPOS = POS	50
52	APOS = NPOS	51
53	ADD = POS - APOS	52
54	IF(NPOS-100) 105, 106, 108	53
55	105 PY(1) = PX(NPOS) + ADD * (PX(NPOS+1) - PX(NPOS))	54
56	GO TO 110	55
57	106 PY(1) = PX(NPOS) - ADD * (PX(NPOS) - PX(NPOS+1))	56
58	110 CONTINUE	57
59	DO 120 I=2, 51	58
60	XX(I) = XX(I-1) + CC1	59
61	C = (XX(I) + XX(I-1)) / 2.	60
62	DO 115 N=1, 8	61
63	D = (U(N) * CC1 + C) * E	62
64	115 AINT(N) = R(N) * EXP(D)	63
65	SUM = C.	64
66	DO 117 N=1, 8	65
67	117 SUM = SUM + AINT(N)	66
68	F(1) = SUM * CC1 + F(1-1)	67
69	XX(2) = XX(1) * XX(1)	68
70	PX(1) = F(1) * E, XX(1) * EXP(-XX(1) * XX(1))	69
71	120 CONTINUE	70
72	RETURN	71
73	END	72

23772 WORDS OF MEMORY USED BY THIS COMPILATION

48884 C6 06-10-70 16,087 INTERPOLATION ON COS AND SIN CHANNEL TRANS

PAGE 1

```

      1      10U  @70
      2      CINTERP  INTERPOLATION ON COS AND SIN CHANNEL TRANS
      3      C      10U  @70
      4
      5      SUBROUTINE INTERP ( X, DE, RME, RC, Rg )
      6
      7      COMMON /CURVE/ BLANC(100), RCOB(100), BLANG(70), RBSIN(70)
      8
      9      IE = G
     10      IM = -X
     11      OLP = X + DE
     12      OLM = IM + DE
     13
     14      R1 = THT1 ( OLP, 100, BLANC, RCOB, 2, IE )
     15      R2 = THT1 ( OLM, 100, BLANC, RCOB, 2, IE )
     16      R3 = THT2 ( OLP, 70, BLANG, RBSIN, 2, IE )
     17      R4 = THT2 ( OLM, 70, BLANG, RBSIN, 2, IE )
     18
     19      RC = RMEB( R1 + R2 )
     20      Rg = RMEB( R3 + R4 )
     21
     22      RETURN
     23      END

```

23784 WORDS OF MEMORY USED BY THIS COMPILATION

42224 G7 10-10-70 10.075 DATA FOR TRANS OF COS AND SIN CHANNELS

PAGE 1

```

1  CURVE      DATA FOR TRANS OF COS AND SIN CHANNELS
2
3  BLOCK DATA
4
5  COMMON /CURVE/ DLANC(100), RCOS(110), DLANS(70), RSIN(70)
6
7  DATA (DLANC(I), I=1, 100)/
8  1-90,0,-90,0,-91,0,-90,0,-87,0,-85,0,-83,0,-81,0,-79,0,-77,0,-75,0,
9  2-75,0,-71,0,-69,0,-67,0,-65,0,-63,0,-61,0,-59,0,-57,0,-55,0,-53,0,
10 3-52,0,-51,0,-50,0,-49,0,-48,0,-46,0,-44,0,-42,0,-40,0,-38,0,-37,0,
11 4-36,0,-35,0,-34,0,-33,0,-31,0,-29,0,-27,0,-25,0,-23,0,-21,0,-19,0,
12 5-17,0,-15,0,-14,0,-13,0,-11,0,- 8,0,- 5,0,- 2,0,- 0,0, 0,0, 0,0,
13 6 8,0, 6,0, 7,0, 9,0, 11,0, 13,0, 15,0, 17,0, 19,0, 21,0, 23,0,
14 7 25,0, 27,0, 29,0, 31,0, 33,0, 35,0, 37,0, 39,0, 41,0, 43,0,
15 8 45,0, 47,0, 49,0, 51,0, 53,0, 55,0, 57,0, 59,0, 61,0, 63,0,
16 9 65,0, 67,0, 69,0, 71,0, 73,0, 75,0, 77,0, 79,0, 81,0,
17 A 83,0, 85,0, 87,0, 89,0, 91,0, 93,0/
18
19  DATA (RCOS(I), I=1, 100)/
20 1  .000, .000, .010, .010, .020, .040, .052, .070, .083, .120, .150,
21 2  .190, .230, .280, .341, .400, .460, .500, .540, .575, .600, .600,
22 3  .600, .575, .540, .500, .460, .400, .341, .280, .230, .190, .150,
23 4  .120, .083, .070, .052, .040, .020, .010, .010, .000, .000, .000,
24 5  .000, .000, .010, .010, .020, .040, .052, .070, .083, .120, .150,
25 6  .190, .230, .280, .341, .400, .460, .500, .540, .575, .600, .600,
26 7  .600, .575, .540, .500, .460, .400, .341, .280, .230, .190, .150,
27 8  .120, .083, .070, .052, .040, .020, .010, .010, .000, .000, .000,
28 9  .000, .000, .000, .000, .000, .000, .000, .000, .000, .000, .000,
29 A  .000, .000, .000, .000, .000, .000, .000, .000, .000, .000/
30
31  DATA (DLANS(I), I=1, 70)/
32 1-60,0,-60,0,-61,0,-60,0,-57,0,-55,0,-53,0,-49,0,-47,0,-45,0,-43,0,-41,0,-39,0,
33 2-37,0,-36,0,-35,0,-34,0,-33,0,-32,0,-31,0,-29,0,-27,0,-25,0,-23,0,
34 3-19,0,-18,0,-17,0,- 8,0,- 6,0,- 7,0,- 8,0,- 9,0,- 9,0,- 8,0,- 7,0,
35 4 8,0, 7,0, 9,0, 9,0, 11,0, 12,0, 13,0, 17,0, 22,0, 24,0, 26,0,
36 5 27,0, 29,0, 31,0, 33,0, 35,0, 37,0, 39,0, 41,0, 43,0, 45,0, 47,0,
37 6 49,0, 51,0, 53,0, 55,0, 57,0, 59,0, 61,0, 63,0, 65,0, 67,0,
38 7 69,0, 71,0, 73,0, 75,0/
39
40  DATA (RSIN(I), I=1, 70)/
41 1 0,0, 0,0, .010, .040, .080, .120, .157, .480, .755, .840, .810,
42 2 .990, .971, .909, .804, 1,00, .990, .875, .738, .565, .370, .160,
43 3 .000, .000, .120, .070, .040, .034, .023, .010, .010, .000, 0,0,
44 4 0,0, 0,0, .010, .040, .070, .120, .220, .420, .600, .800,
45 5 .900, .971, .990, .990, .970, .875, .738, .565, .370, .160,
46 6 .000, .000, .000, .000, .120, .070, .040, .034, .023, .010, .010,
47 7 .000, .010, .000, .000/
48
49 END

```


[illegible]

NO	NAMLIST	ROFX	CI	INTEGRAL CALCULATED TO X=	5.47E CC,	OVER COS SARD CURVE	4.603833E-11,	OVER SIN SARD CURVE	2.272310E-11	RHO=	4.936882E-01
1	NAMLIST	ROFX	CI	ME	2.790128E 18	TE	5.000000E C3	ALPHA	6.000000E-01	BETA	5.1448879E-01C1
NO	NAMLIST	ROFX	CI	INTEGRAL CALCULATED TO X=	5.47E CC,	OVER COS SARD CURVE	6.187893E-11,	OVER SIN SARD CURVE	3.292511E-11	RHO=	5.347538E-01
1	NAMLIST	ROFX	CI	ME	3.797871E 18	TE	5.000000E C3	ALPHA	7.000000E-01	BETA	5.7548234E-01C1
NO	NAMLIST	ROFX	CI	INTEGRAL CALCULATED TO X=	5.47E CC,	OVER COS SARD CURVE	7.893199E-11,	OVER SIN SARD CURVE	4.504787E-11	RHO=	5.535844E-01
1	NAMLIST	ROFX	CI	ME	4.8602843E 18	TE	5.000000E C3	ALPHA	8.000000E-01	BETA	6.2489504E-01C1
NO	NAMLIST	ROFX	CI	INTEGRAL CALCULATED TO X=	5.47E CC,	OVER COS SARD CURVE	9.121879E-11,	OVER SIN SARD CURVE	5.9042C1E-11	RHO=	6.472871E-01
1	NAMLIST	ROFX	CI	ME	6.277784E 18	TE	5.000000E C3	ALPHA	9.000000E-01	BETA	6.8888473E-01C1
NO	NAMLIST	ROFX	CI	INTEGRAL CALCULATED TO X=	5.47E CC,	OVER COS SARD CURVE	1.037090E-10,	OVER SIN SARD CURVE	7.480823E-11	RHO=	7.213888E-01
1	NAMLIST	ROFX	CI	ME	7.790350E 18	TE	5.000000E C3	ALPHA	1.000000E CC	BETA	7.0710678E-01C1
NO	NAMLIST	ROFX	CI	INTEGRAL CALCULATED TO X=	5.47E CC,	OVER COS SARD CURVE	1.138880E-10,	OVER SIN SARD CURVE	9.219402E-11	RHO=	8.088073E-01
1	NAMLIST	ROFX	CI	ME	8.300480E 18	TE	6.000000E C3	ALPHA	1.000000E-01	BETA	8.5503718E-01C1
NO	NAMLIST	ROFX	CI	INTEGRAL CALCULATED TO X=	5.00E CC,	OVER COS SARD CURVE	2.68217E-12,	OVER SIN SARD CURVE	1.288219E-12	RHO=	4.808228E-01
1	NAMLIST	ROFX	CI	ME	3.7801883E 14	TE	6.000000E C3	ALPHA	2.000000E-01	BETA	1.8811813E-01C1
NO	NAMLIST	ROFX	CI	INTEGRAL CALCULATED TO X=	5.00E CC,	OVER COS SARD CURVE	1.028881E-11,	OVER SIN SARD CURVE	5.08801E-12	RHO=	4.830808E-01
1	NAMLIST	ROFX	CI	ME	8.5703787E 14	TE	6.000000E C3	ALPHA	3.000000E-01	BETA	2.8734789E-01C1
NO	NAMLIST	ROFX	CI	INTEGRAL CALCULATED TO X=	5.00E CC,	OVER COS SARD CURVE	2.280288E-11,	OVER SIN SARD CURVE	1.141682E-11	RHO=	5.141788E-01
1	NAMLIST	ROFX	CI	ME	1.4880673E 18	TE	6.000000E C3	ALPHA	4.000000E-01	BETA	5.7138067E-01C1
NO	NAMLIST	ROFX	CI	INTEGRAL CALCULATED TO X=	5.00E CC,	OVER COS SARD CURVE	5.740891E-11,	OVER SIN SARD CURVE	2.08823E-11	RHO=	5.443708E-01
1	NAMLIST	ROFX	CI	ME	2.3881088E 18	TE	6.000000E C3	ALPHA	5.000000E-01	BETA	4.4721358E-01C1
NO	NAMLIST	ROFX	CI	INTEGRAL CALCULATED TO X=	5.00E CC,	OVER COS SARD CURVE	5.481842E-11,	OVER SIN SARD CURVE	5.191588E-11	RHO=	5.843848E-01
1	NAMLIST	ROFX	CI	ME	3.3481818E 18	TE	6.000000E C3	ALPHA	6.000000E-01	BETA	5.1448879E-01C1
NO	NAMLIST	ROFX	CI	INTEGRAL CALCULATED TO X=	5.00E CC,	OVER COS SARD CURVE	7.280127E-11,	OVER SIN SARD CURVE	4.804828E-11	RHO=	5.350888E-01
1	NAMLIST	ROFX	CI	ME	4.8878081E 18	TE	6.000000E C3	ALPHA	7.000000E-01	BETA	5.7548234E-01C1
NO	NAMLIST	ROFX	CI	INTEGRAL CALCULATED TO X=	5.00E CC,	OVER COS SARD CURVE	9.88313E-11,	OVER SIN SARD CURVE	6.288110E-11	RHO=	6.877348E-01
1	NAMLIST	ROFX	CI	ME	5.882888E 18	TE	6.000000E C3	ALPHA	8.000000E-01	BETA	6.2489504E-01C1
NO	NAMLIST	ROFX	CI	INTEGRAL CALCULATED TO X=	5.00E CC,	OVER COS SARD CURVE	1.085878E-10,	OVER SIN SARD CURVE	5.187884E-11	RHO=	7.738847E-01
1	NAMLIST	ROFX	CI	ME	7.833340E 18	TE	6.000000E C3	ALPHA	9.000000E-01	BETA	6.8888473E-01C1
NO	NAMLIST	ROFX	CI	INTEGRAL CALCULATED TO X=	5.00E CC,	OVER COS SARD CURVE	1.188218E-10,	OVER SIN SARD CURVE	1.027881E-10	RHO=	8.844177E-01
1	NAMLIST	ROFX	CI	ME	8.3004807E 18	TE	6.000000E C3	ALPHA	1.000000E CC	BETA	7.0710678E-01C1
NO	NAMLIST	ROFX	CI	INTEGRAL CALCULATED TO X=	5.00E CC,	OVER COS SARD CURVE	1.28431E-10,	OVER SIN SARD CURVE	1.287484E-10	RHO=	9.715278E-01
1	NAMLIST	ROFX	CI	ME	1.088481E 14	TE	7.000000E C3	ALPHA	1.000000E-01	BETA	8.9503718E-01C1

NO	NAMLIST	ROFX	CI	4.680E CC,	OVER COS SERR CURVE	3.06842E-12,	OVER SIN SERR CURVE	1.67233E-12	RHOF	8.46067E-C1
1	NAMLIST	ROFX	CI	4.340180E 14	TE	7.000000E C3	ALPHA	2.000000E-C1	BETA	1.0011012E-C1
NO	NAMLIST	ROFX	CI	4.680E CC,	OVER COS SERR CURVE	1.19420E-11,	OVER SIN SERR CURVE	6.09342E-12	RHOF	8.60897E-C1
1	NAMLIST	ROFX	CI	8.788441E 14	TE	7.000000E C3	ALPHA	8.000000E-C1	BETA	2.073478E-C1
NO	NAMLIST	ROFX	CI	4.680E CC,	OVER COS SERR CURVE	2.67804E-11,	OVER SIN SERR CURVE	1.80113E-11	RHOF	8.83304E-C1
1	NAMLIST	ROFX	CI	1.736078E 18	TE	7.000000E C3	ALPHA	4.000000E-C1	BETA	8.7138067E-C1
NO	NAMLIST	ROFX	CI	4.680E CC,	OVER COS SERR CURVE	4.32338E-11,	OVER SIN SERR CURVE	2.082847E-11	RHOF	8.80874E-C1
1	NAMLIST	ROFX	CI	2.712627E 18	TE	7.000000E C3	ALPHA	8.000000E-C1	BETA	4.472138E-C1
NO	NAMLIST	ROFX	CI	4.680E CC,	OVER COS SERR CURVE	6.28034E-11,	OVER SIN SERR CURVE	4.19048E-11	RHOF	8.67237E-C1
1	NAMLIST	ROFX	CI	3.806178E 18	TE	7.000000E C3	ALPHA	6.000000E-C1	BETA	8.144887E-C1
NO	NAMLIST	ROFX	CI	4.680E CC,	OVER COS SERR CURVE	8.88888E-11,	OVER SIN SERR CURVE	6.08012E-11	RHOF	7.38273E-C1
1	NAMLIST	ROFX	CI	8.316740E 18	TE	7.000000E C3	ALPHA	7.000000E-C1	BETA	8.784823E-C1
NO	NAMLIST	ROFX	CI	4.680E CC,	OVER COS SERR CURVE	1.08012E-10,	OVER SIN SERR CURVE	8.15631E-11	RHOF	7.88823E-C1
1	NAMLIST	ROFX	CI	6.844314E 18	TE	7.000000E C3	ALPHA	8.000000E-C1	BETA	6.848804E-C1
NO	NAMLIST	ROFX	CI	4.680E CC,	OVER COS SERR CURVE	1.18238E-10,	OVER SIN SERR CURVE	1.08648E-10	RHOF	8.86047E-C1
1	NAMLIST	ROFX	CI	8.78887E 18	TE	7.000000E C3	ALPHA	9.000000E-C1	BETA	6.88887E-C1
NO	NAMLIST	ROFX	CI	4.680E CC,	OVER COS SERR CURVE	1.33647E-10,	OVER SIN SERR CURVE	1.38081E-10	RHOF	8.8887E-C1
1	NAMLIST	ROFX	CI	1.080481E 18	TE	7.000000E C3	ALPHA	1.000000E CC	BETA	7.071067E-C1
NO	NAMLIST	ROFX	CI	4.680E CC,	OVER COS SERR CURVE	1.44734E-10,	OVER SIN SERR CURVE	1.60373E-10	RHOF	1.10803E CC
1	NAMLIST	ROFX	CI	1.84008E 14	TE	8.000000E C3	ALPHA	1.000000E-C1	BETA	8.80371E-C1
NO	NAMLIST	ROFX	CI	4.330E CC,	OVER COS SERR CURVE	3.48844E-12,	OVER SIN SERR CURVE	2.11150E-12	RHOF	6.05112E-C1
1	NAMLIST	ROFX	CI	4.88084E 14	TE	8.000000E C3	ALPHA	2.000000E-C1	BETA	1.8811012E-C1
NO	NAMLIST	ROFX	CI	4.330E CC,	OVER COS SERR CURVE	1.38870E-11,	OVER SIN SERR CURVE	6.444387E-12	RHOF	6.21801E-C1
1	NAMLIST	ROFX	CI	1.116080E 18	TE	8.000000E C3	ALPHA	3.000000E-C1	BETA	2.873478E-C1
NO	NAMLIST	ROFX	CI	4.330E CC,	OVER COS SERR CURVE	2.88480E-11,	OVER SIN SERR CURVE	1.88856E-11	RHOF	6.48187E-C1
1	NAMLIST	ROFX	CI	1.884088E 18	TE	8.000000E C3	ALPHA	4.000000E-C1	BETA	8.7138067E-C1
NO	NAMLIST	ROFX	CI	4.330E CC,	OVER COS SERR CURVE	4.88147E-11,	OVER SIN SERR CURVE	8.38822E-11	RHOF	6.88718E-C1
1	NAMLIST	ROFX	CI	3.100140E 18	TE	8.000000E C3	ALPHA	8.000000E-C1	BETA	4.472138E-C1
NO	NAMLIST	ROFX	CI	4.330E CC,	OVER COS SERR CURVE	7.07801E-11,	OVER SIN SERR CURVE	8.84438E-11	RHOF	7.40804E-C1
1	NAMLIST	ROFX	CI	4.48808E 18	TE	8.000000E C3	ALPHA	6.000000E-C1	BETA	8.144887E-C1
NO	NAMLIST	ROFX	CI	4.330E CC,	OVER COS SERR CURVE	9.30884E-11,	OVER SIN SERR CURVE	7.80348E-11	RHOF	8.68008E-C1
1	NAMLIST	ROFX	CI	6.07878E 18	TE	8.000000E C3	ALPHA	7.000000E-C1	BETA	8.784823E-C1

NO NAMELIST ROPX C1
 INTERNAL CALCULATED TO X= 4.330E 00, OVER COS 88RD CURVE 1.141448E-10, OVER SIN 88RD CURVE 1.011330E-10 RHO= 0.840000E-01
 1 NAMELIST ROPX C1
 ME 7.034889E 18 TE 0.000000E 03 ALPHA 0.000000E-01 BETA 0.048850E-01
 NO NAMELIST ROPX C1
 INTERNAL CALCULATED TO X= 4.330E 00, OVER COS 88RD CURVE 1.088838E-10, OVER SIN 88RD CURVE 1.302880E-10 RHO= 0.804830E-01
 1 NAMELIST ROPX C1
 ME 1.004448E 18 TE 0.000000E 03 ALPHA 0.000000E-01 BETA 0.088847E-01
 NO NAMELIST ROPX C1
 INTERNAL CALCULATED TO X= 4.330E 00, OVER COS 88RD CURVE 1.484888E-10, OVER SIN 88RD CURVE 1.817880E-10 RHO= 1.088480E 00
 1 NAMELIST ROPX C1
 ME 1.840088E 18 TE 0.000000E 03 ALPHA 1.000000E 00 BETA 7.071067E-01
 NO NAMELIST ROPX C1
 INTERNAL CALCULATED TO X= 4.330E 00, OVER COS 88RD CURVE 1.004800E-10, OVER SIN 88RD CURVE 1.048330E-10 RHO= 1.211080E 00

APPENDIX IV

ERROR STATEMENT

Although it is difficult to evaluate these test results unless compared to results obtained from a different technique, it is instructive to compute the error obtained in reading the data and measurement of the laser energy. We evaluate this for one measurement (Test #304 of the tunnel experiments) to obtain an indication of the error. The initial computation is the summation error resulting in a photon error $\pm 250 \phi$ on PM #1 and $\pm 590 \phi$ on PM #2. It is noted that these values are greater than the statistical error. Hence PM #1 is $27,500 \pm 250$ and PM #2 is $16,500 \pm 590$. The summation of these two channels results on an error,

$$\sum_{1,2} = 44,000 \pm \sqrt{(250)^2 + (590)^2} \quad (1)$$

$$\text{or } \sum_{1,2} \approx 44,000 \pm 650 \phi \quad (2)$$

To obtain N_e , we divide this value by the energy of the laser beam assumed to be accurate to $\pm 10\%$ or $0.11 \pm .01$. The probable error can be obtained from,

$$P.E. = \pm \frac{1}{A} \sqrt{b^2 + \frac{B^2 a^2}{A^2}} \quad \text{for } B/A$$

where a is error in A and b is the error in B . Substituting we obtain,

$$P.E. = \pm \frac{1}{0.11} \sqrt{(650)^2 + \frac{(4.4 \times 10^4)^2 \cdot 10^{-4}}{(0.1 \times 10^{-1})^2}} \quad (3)$$

Evaluating we obtain,

$$P.E. = \pm 3.6 \times 10^4 \phi/\text{joule} \quad (4)$$

Since the total signal is $(4.4 \times 10^4)/0.11$ or 4.0×10^5 ϕ /joule and Ne is proportional to this value we conclude that the summation process yields a measurement of $\pm 10\%$.

To obtain the electron temperature, we ratio PM #2 output to PM #1 output or

$$\rho = \frac{16,500 \pm 590}{27,500 \pm 250} \quad (5)$$

Evaluating this expression in the same way, we obtain

$$\rho = 0.600 \pm 0.02$$

Referring to FIG 19, at 6000°K and with $\text{Ne} = 2.8 \times 10^{15}$ this corresponds to an error in temperature of $\pm 200^\circ\text{K}$. A more accurate measurement of temperature can probably be obtained by more careful measurement of the voltage. However, the measurement of electron concentration is set by the accuracy of the laser energy monitor.

APPENDIX V

REPRODUCTION OF PAPER BY C. J. HARRIS

CORRELATION OF INVISCID AIR NONEQUILIBRIUM SHOCK LAYER PROPERTIES*

Clarence J. Harris, Staff Scientist
General Electric Company
Valley Forge, Pa.

Abstract

It has already been shown that the entropy value defined under equilibrium stagnation conditions in the plenum or reservoir region of a nozzle readily correlates and permits the prediction of the quantitative nonequilibrium chemical and electron composition of the downstream converging-diverging nozzle expanding airflow. This correlation based on plenum entropy also can be applied to define the axial station in a given nozzle where transition from equilibrium to "frozen" nonequilibrium flow occurs. In this paper an analog is developed relating this "entropy correlation" for the axisymmetric nozzle situation to the shock layer flow situation about a conical body with nose bluntness. The analog as initially developed was limited to considering the innermost stream tube of an inviscid nonequilibrium shock layer airflow. The earlier nozzle entropy correlation was used to predict the frozen nonequilibrium properties in this stream tube and these predicted properties then compared to shock layer values derived from a detailed nonequilibrium flow field numerical calculation. The resulting comparison indicates that the "nozzle-shock layer analog" and entropy correlation are useful in predicting shock layer properties thus reducing the need for extensive numerical calculations. Additional applications and limitations of the newly developed "analog" technique are evaluated, particularly as they aid in quickly defining, as a function of vehicle altitude and flight velocity, the properties at the inviscid shock layer flow-viscous boundary layer edge. Preliminary experimental laser plasma probe measurements also are presented of electron density/temperature in a high enthalpy shock tunnel nozzle air flow. These results suggest an entropy correlation for predicting nonequilibrium electron temperatures in frozen heavy particle flows.

Nomenclature

$A_{(b)}$	- Annular stream tube area at Station b (see Fig. 4)
$A_{(*)}$	- Annular stream tube area at sonic point
A/A_*	- Area ratio
B	- Bluntness ratio, r_n/r_b
h	- Altitude
H/RT_0	- Enthalpy ratio
l	- Nozzle scale parameter
M_∞	- Free stream Mach number
N_{es}	- Electron concentration at stagnation point
P_5	- Plenum or reservoir stagnation pressure
r_1	- Centerbody radius at sonic point
r_b	- Centerbody radius at Station b
r_n	- Nose radius

S/R	- Entropy ratio
T_5	- Plenum or reservoir stagnation temperature
v_∞	- Free stream velocity
x	- Thickness of innermost inviscid stream tube
ξ	- x/r_n

I. Introduction

The phenomena associated with the expansion of air in a nozzle to hypersonic velocities have been studied by several authors. Early analytical work on flow expansions and nonequilibrium effects was carried out by Bray⁽¹⁾⁽²⁾ on monoatomic gases. More recently Lordi and Mates⁽³⁾ did a detailed computer program study for high enthalpy air flows with nonequilibrium effects present. Harris⁽⁴⁾ utilized the results of Reference 3 and similar computer calculations by Boyer⁽⁵⁾ and Eschenroeder et al⁽⁶⁾ to show that the nonequilibrium chemical composition in the expanding nozzle airflow could be readily correlated as a function of plenum or reservoir entropy. Harris et al⁽⁷⁾ also showed that a similar "entropy correlation" was valid for specifying the nonequilibrium electron concentration values in an expanding air flow. Both Harney⁽⁸⁾ and Ring and Johnson⁽⁹⁾ have made extensions to the entropy correlation concept offered in References 4 and 10. This simplified entropy correlation for handling energetic nozzle air flows has had direct application in understanding and defining hypersonic and hypervelocity test facilities performance⁽¹⁰⁾⁽¹¹⁾⁽¹²⁾⁽¹³⁾. In this paper the nozzle nonequilibrium entropy correlation approach is adapted to the case of hypersonic shock layer flow around a blunt, slender axisymmetric body and accordingly used to predict certain pertinent properties in the shock layer. This work is discussed in greater detail in Reference 20.

II. Analysis"Nozzle-Shock Layer Analog"A. Nozzle

The general conditions required for the valid application of the entropy correlation⁽⁴⁾⁽¹⁰⁾ are:

1. The plenum or stagnated reservoir reacting gas (air) is in equilibrium.
2. The reacting flow stays in equilibrium in expanding from the plenum to the nozzle throat (sonic point).
3. Viscous effects are ignored.

This is illustrated using the air Mollier Diagram in Figure 1. The "departure from equilibrium" boundary (Figure 1) was defined in Reference 3 and the "frozen flow" limit on the Air Mollier Diagram is as defined in References 10 and 11. The entropy correlation has meaningful application only when the plenum operating points (such as A, B, C, D, E and F in Figure 1) are above the departure from equilibrium boundary on the Mollier Diagram. Should the plenum operating point fall below this boundary or the frozen flow limit, the entropy correlation is not applicable.

The Air Mollier Diagram accurately defines equilibrium thermodynamic and kinetic properties (temperature, pressure, density, velocity, and Z) above the departure from equilibrium boundary. Below this boundary and the frozen flow line, finite rate chemistry occurs and the equilibrium thermodynamic and kinetic properties are no longer valid. However, it has been shown⁽³⁾⁽⁶⁾⁽¹⁰⁾ that for an expanding flow the equilibrium and nonequilibrium particle velocity and density differ very little.

With this kind of a Mollier Diagram representation of the nozzle flow process it is also possible to define the area ratio (A/A_*) value at which "freezing" occurs. The performance limit line for the GE High Enthalpy Shock Tunnel⁽¹⁴⁾⁽¹⁵⁾ is also included in Figure 1 and provides performance equal to or in excess of similar facilities⁽²⁵⁾. So, it may be expected that in most currently operating test facilities nonequilibrium freezing occurs at small area ratio values or just downstream of the nozzle throat. The original entropy correlation of frozen nonequilibrium chemical (Figure 2) and electron (Figure 3)* composition data (References 4, 10, and 7) was carried out at and presented for $A/A_* = 10^3$. Nonetheless, these correlations are still valid for the much smaller A/A_* values such as defined under the conditions in Figure 1. This area ratio concept for defining the station where nonequilibrium frozen air flow occurs is applied to the shock layer flow situation.

B. Shock Layer

This section deals with establishing an analog between nozzle flow and shock layer flow and, accordingly, applies to the shock layer flow situation and nozzle prediction techniques discussed. A rigorous mathematical solution to the equilibrium shock layer flow field problem was derived quite early by Gravalos and his fellow workers⁽¹⁶⁾. Gravalos⁽¹⁷⁾ has recently summarized the analytical work in this field for the flow of inviscid, reacting gas mixtures about axisymmetric bodies.

The typical shock layer flow situation to be considered is given in Figure 4. The center body is a cone with a hemispherical nose. Thus the stream tube crossing the bow shock wave at (a) is eventually stagnated at (s) and then expands to sonic velocity at (*) and becomes supersonic downstream of this point. Thus, region (s) in the shock layer flow is analogous to the plenum region in the nozzle flow situation (see Figure 4a)

and (*) in the shock layer situation is analogous to the throat in the nozzle flow case (see Figure 4b.). Further, the supersonic expansion of the center body stream tube downstream of the sonic point is analogous to the supersonic expansion in the nozzle case. Therefore, the present analysis is restricted to an evaluation of the center body stream tube and regions such as (s), (*), and later on (b), in the shock layer flow. It is necessary to require that the reacting stagnated air in region (s) be in equilibrium and that it undergo an equilibrium expansion to the sonic point (*). It is next desirable to define an equivalent area ratio $A(b)/A(*)$ for the center body stream tube at and beyond which the chemistry should be "frozen" in its nonequilibrium state. This equivalent area ratio is defined using the following assumptions:

1. The total shock layer is inviscid
2. The whole reacting airflow region between the bow shock and body and from the stagnation line to the sonic line is in equilibrium and
3. The center body stream tube thickness, $x \ll r_n$ (Figure 4).

Under these first two conditions, Edsall⁽¹⁸⁾ showed for a wide range of free stream Mach numbers ($M_\infty = 3.5$ to 35) that

$$r_1 \approx (0.6 \text{ to } 0.7) r_n \quad (1)$$

Therefore, the annular stream tube area at (*) and (b) will be

$$A_{(*)} = \pi (x + r_1)^2 - \pi r_1^2 \quad (2)$$

$$A_{(b)} = \pi (x + r_b)^2 - \pi r_b^2 \quad (3)$$

then

$$A_{(b)}/A_{(*)} = x^2 + 2xr_b/(x^2 + 2xr_1) \quad (4)$$

since

$$B \text{ (bluntness ratio)} = r_n/r_b \quad (5)$$

and

$$r_1 \approx 0.65 r_n \quad (6)$$

then

$$A_{(b)}/A_{(*)} \approx \frac{x + 2r_n/B}{x + 1.3r_n} \quad (7)$$

let

$$\xi = x/r_n = f(M_\infty, h) \quad (8)$$

*Note that these results supercede those offered in Reference 7 where the data had been mistakenly miss-plotted.

then

$$A_{(b)}/A_{(*)} \approx \frac{\xi + 2/B}{\xi + 1.3} \quad (9)$$

for $\xi \ll 1$ and $B < 1$

$$A_{(b)}/A_{(*)} \approx 2/1.3 B \quad (10)$$

Assumption No. 2 was necessary for arriving at a general definition as to the location of the sonic point on the center body (i.e., Eq. 6). The next step is to determine the stagnation enthalpy and entropy values at (s) for the flight conditions under consideration. If this operating point falls above the departure from equilibrium boundary on the Air Mollier Diagram (Figure 1), then the equivalent area ratio or bluntness ratio (B) at which freezing will occur may be determined. Once this center body station (or area ratio) is defined, the chemical composition and electron concentration in the center body stream tube at points downstream of this station may be predicted (from Figure 2 and Figure 3, respectively) based on the stagnation point entropy value.

Comparison with Numerical Calculations

Inviscid, nonequilibrium sphere-cone body shock layer calculations have recently been performed by McMenamin and O'Brien⁽¹⁹⁾. The results from these calculations were compared to the results based on the prediction techniques discussed above. While the results of the calculations⁽¹⁹⁾ are quite extensive, covering the full shock layer flow field and also considering the problem of inviscid flow-viscous boundary layer interaction, attention here is again restricted only to the center body stream tube for the case of purely inviscid flow; i.e., where no boundary layer is present (although the center-body shape may have been altered to account for the boundary layer displacement thickness, δ^*).

The center body configuration selected was one which had a cone angle of $<10^\circ$ and slight cone bluntness. Inviscid flow field results were chosen for four flight conditions. The prediction techniques proposed herein were compared to the results from these flight conditions. The four flight conditions are:

	h (ft)	v_∞ (ft/sec)
1.	50×10^3	19,200
2.	100×10^3	21,500
3.	150×10^3	21,950
4.	200×10^3	22,000

Detailed flow field calculations⁽¹⁹⁾ were available for three normals along the center body surface for each of these flight conditions. The most downstream of these normals is at a body station yielding an equivalent area ratio value of approximately 50, thus well into the "frozen" nonequilibrium flow regime⁽²⁰⁾ on the body. The numerically calculated⁽¹⁹⁾ shock layer chemical

composition for the center body stream tube at this body station is compared for the four flight conditions (in Figure 5) with the composition based on the nozzle entropy correlation⁽⁴⁾⁽¹⁰⁾. The species considered are O_2 , N_2 , O, and N. The symbols are for the numerically calculated shock layer values and the solid lines are from the nozzle correlation⁽⁴⁾⁽¹⁰⁾.

With the exception of the order of magnitude disagreement between the calculated value of N and the value for N predicted by the correlation at the 50K feet condition, the overall agreement is quite good and the correlation appears to predict the chemical properties in the frozen nonequilibrium portion of the inviscid center body stream tube quite well. A similar comparison is offered in Figure 6 for the electron concentration. While the general quantitative level of the numerically calculated shock layer results follows that of nozzle correlation, the trend and agreement between the two is not clear. Since the prediction of shock layer electron concentration as a function of flight trajectory is of importance to many investigators, the results of Figure 6 are evaluated in more detail in the next section.

III. Applications and Limitations

Flight Trajectory and Vehicle Size

The foregoing analysis has been restricted to the case of a fully inviscid shock layer flow and the prediction techniques have been compared only to one particular body shape and size. The first restriction requires that the prediction techniques should only be applicable in the flight regime where the inviscid shock layer flow situation is approximated. Probst⁽²¹⁾ has defined seven regimes that develop during atmospheric re-entry for the flow field environment about a body having a spherical stagnation regime. For a nose radius of 0.5 inch, the regime of interest, the viscous boundary layer-inviscid shock layer regime, occurs at altitudes of 175K feet and below. For a nose radius of 1 foot the maximum altitude would be adjusted to 240K feet.

The variation in nozzle size or "time-rate-of-expansion" and its effect on the entropy correlation is considered in detail in References 8 and 9. In the correlation of References 4, 7, and 10 limited consideration was given to the physical scale of the nozzle and its effect on the entropy correlation. Figure 2 shows that a scale factor (L) variation of 4.7 does not greatly affect the nozzle entropy correlation as applied to chemical composition. Ring and Johnson⁽⁹⁾ looked at a wide range of values of the nozzle size and shape similarity parameter (τ_c) and their influence on the entropy correlation. Figures 3 and 6 indicate that the dimensional scale factor does have a pronounced effect on the nozzle entropy correlation as regards electron concentrations.

Further, Eschenroeder⁽²²⁾ contends that ionization freezing in a nozzle takes place upstream of neutral chemical freezing. So while the entropy correlation and nozzle-shock layer analog may have direct application in the case of neutral chemical composition, more detailed consideration must be given to the electron concentration situation. This will be discussed further when the

experimental laser probe measurements are presented of electron density/temperature. Reference 22 also points up the differences in electron concentration values that result from considering a "simple kinetic" model as compared to a "complex kinetic" model. The simple kinetic model allows for only nitric oxide ionization. The complex kinetic model allows for the additional species of O^+ , N^+ , and N_2^+ . For this reason the comparison of the nozzle entropy correlation of electron concentration to the shock layer numerical calculations (Figure 6) is replotted in Figure 7 to account for this.

Reference 20 showed that for both the nozzle and shock layer cases the ionized species are determined using the nitric oxide dissociative-recombination reaction only. Eschenroeder(22) argues that the model involving this reaction and the three body NO reaction is correct for nozzle flows where plenum pressures are usually quite high. But, for shock layer flow where the stagnation pressure is much lower, the complex kinetic model is applicable. The pressure argument may in fact really be an entropy argument. That is, below a certain plenum entropy value the simple kinetic model is valid and above that entropy value the complex kinetic model holds. This can be argued from Figures 2 or 5. That is, for entropy values up to $S/R = 38$, the NO concentration exceeds the N atom concentration and electron production might be expected to be controlled mainly by the three body, $M + NO^+ + e^- \rightleftharpoons NO + M$ reactions and partially by the dissociative-recombination reaction $NO^+ + e^- \rightleftharpoons N + O$ (28). Above $S/R = 38$ the latter reaction should be a major electron production contributor and the N^+ reaction becoming quite an effective contributor, along with the O^+ and N_2^+ reactions.

Thus, the complex kinetic model appears to be valid at the higher entropy values and the simple kinetic model valid at the lower S/R values. This is a postulation and requires further investigation. Nevertheless, the information in Figure 7 was replotted without modifying the nozzle results and the two shock layer values at the lower entropy conditions (50K feet and 100K feet altitude). The 150K feet altitude shock layer value was replaced by its equilibrium value since it is closer to the complex kinetic model nonequilibrium value(22) and the nonequilibrium complex kinetic model value obtained in Reference 22 was included.

Using these values for the shock layer flow where the stagnation point entropy value is large causes the data to lie on a relatively smooth curve. Also presented in Figure 7 are experimental data by Dunn and Lordi(23, 28) obtained in recent shock tunnel nozzle studies. The data are from an experiment in which $L \approx 3.26$ cm. These experimental results indicate that the chemical kinetic-thermodynamic model of References 3, 5, and 6 slightly overpredicts the measured frozen nonequilibrium electron concentration in the nozzle. These data and electron density/temperature data obtained in this study are discussed later in this paper.

The present nozzle-shock layer analog specifies no particular restrictions on center body cone half angle. Figure 1 and the Equations (1) to (10) imply only a bluntness ratio dependence. Therefore, the analog should

hold for a range of center body cone half angles. However, the restrictions on this argument need to be more thoroughly developed and investigated.

Application to Flight

An additional specification discussed earlier was the requirement that the stagnation enthalpy-entropy value of the air be such as to place the equivalent plenum operating point ((s) Figure 4) above the "departure from equilibrium" boundary and the "frozen flow" line on the Air Mollier Diagram (Figure 1). The frozen flow line and the maximum flight altitude at which an inviscid shock layer-viscous boundary layer flow situation(21) is approximated may be used jointly to define the limits of applicability of the entropy correlation in predicting shock layer properties. These limits are shown in Figures 8 and 9. Figure 8 presents the entropy correlation of shock layer flow properties as a function of vehicle flight conditions. Flight velocity (v_∞) and center body stream tube stagnation point enthalpy (H_g/RT_0) are presented versus entropy (S/R). Lines of constant flight altitude (h) and stagnation point electron density ($Ne_{s(equil.)}$) are also included. The four flight conditions that were used are shown (filled circles) as well as the flight point from Reference 22 (open circle). The altitude boundaries for achieving a viscous boundary layer-inviscid shock layer flow are presented for both a 0.5 inch and 1.0 foot nose radius center body.

The other limit line is the frozen flow line. In References 4 and 10 this line was defined based upon the degree of oxygen dissociation (in upper Figure 8 denoted by hatching directed towards the left on the frozen flow limit line). The percentage of undissociated oxygen derivable from the entropy correlation is tabulated along the entropy (S/R) axis of upper Figure 8. The frozen flow limit line was extended by considering the total degree of air dissociation and accounting for the nitrogen dissociation (in upper Figure 8 denoted by hatching directed towards the right on the frozen flow limit line). Therefore, in the region in Figure 8 that is below 175K feet for a 0.5 inch nose radius and which is above the frozen flow line, it is possible to apply the entropy correlation in predicting the center body stream-tube shock layer flow properties. This can be done in the acceptable regime at any point along the flight trajectory of a slightly blunted vehicle since the stagnation point entropy is specified by altitude and velocity. Other limits are those in which the chemical model is valid. The model(19)(24) is taken to be valid below 200K feet and for M_∞ less than 30(17).

Presented below the flight condition plot in Figure 8 is a replot of the entropy correlation of neutral species and electron concentration. One need only to use the top half of Figure 8 to determine the stagnation point entropy value at any given point on a flight trajectory (v_∞ and h). Then, by projecting straight down along this entropy value to the curves below, an estimate of the electron concentration is obtained as well as fairly accurate quantitative values of the neutral chemical species concentration. Thus, for example a vehicle at 100K feet altitude and flying at 25,000 ft/sec is predicted to have

a downstream center body stream tube electron density value of 3×10^{-6} (mol/gm mix.) and the neutral chemical species composition specified at the entropy (S/R) value of 46. The stagnation point equilibrium electron density value will be 10^{16} electrons/cm³.

Boundary Layer Effects

The assumption made so far of a fully inviscid shock layer flow is only an approximation of the real shock layer flow situation which involves not only an inviscid flow regime but also a viscous boundary layer. It was the need to treat this realistic flow situation that led to the analytical study and numerical calculations of Reference 19. In that study detailed consideration was given to the mixing or "swallowing" that takes place between the inviscid flow and the viscous boundary layer and the resulting effect on the properties in the full shock layer. In this investigation consideration was given to the influence on electron concentration of catalytic wall - noncatalytic wall effects, laminar boundary layer, and impurities in the boundary layer. This discussion is given in Reference 20.

In general, the inviscid solutions yield N_e values an order of magnitude greater than those obtained with a pure air laminar boundary layer and a catalytic wall. However, the measurements discussed in the next section indicate that adjustments need to be made in the inviscid theoretical model that accordingly lead to a factor of three or four reduction in the predicted electron concentration.

Since the analog is based on the entropy correlation that in turn assumes negligible changes in entropy during the expansion process (29), the shock layer predictions are only good along the body from the upstream "freeze" station to the downstream station where pronounced entropy changes begin to occur. Downstream of this station the prediction techniques are only good for making estimates.

IV. Experimental Study

Laser Plasma Probe-Shock Tunnel Electron Density/Temperature Measurements

Limited data were obtained of the electron density and temperature in the expanding air flow of the GE High Enthalpy Shock Tunnel (14)(15). A recently developed Laser Plasma Probe (27) was used to obtain these data at a A/A^* value of 3.6 where the flow is predicted to be in equilibrium and of high density ($\rho/\rho_0 \sim 1$). The measured temperature values agreed within 10% with the theoretical equilibrium heavy particle gas temperature values. The measured electron density values were within 20% of the theoretical equilibrium values. These preliminary results imply that the electrons and heavy particles are in "equilibrium" with each other in the theoretically predicted equilibrium expanded flow regime. From the entropy correlation, these experimental results, and the only other experimental work of this type available, that of Dunn and Lordi (23)(28), a model for the "nonequilibrium" electron temperature

characteristics was postulated. It is postulated that the electron temperature and heavy particle temperature are the same in the equilibrium expanding flow regime. When the flow expands to its "freeze" point the electron and heavy particle temperatures uncouple. For an example look at the plenum or reservoir point E in Figure 1. The flow expands in equilibrium from this point to an area ratio, A/A^* , of 4. At this expansion value, frozen, nonequilibrium flow exists. Further, the decay in electron temperature with increasing expansion lags the heavy particle temperature decay. This is illustrated in Figure 10, using the results of References 23, 27, 28. The postulated "electron initial lag temperature" is uniquely defined by the entropy correlation and would be as presented in Figure 11. Verification of this postulation may be accomplished by an experimental study in which the electron density and temperatures are measured both in the equilibrium and nonequilibrium expanded flow regimes. At present the laser plasma probe appears to be the better technique for accomplishing this. Other techniques such as Langmuir probes, time-of-flight mass spectrography, and microwave probes are severely limited as to the nozzle flow regimes in which they are applicable.

V. Conclusions

Within the appropriate flight regime as defined in Figures 8 and 9, the entropy correlation and nozzle-shock layer analog may be used to predict the frozen nonequilibrium properties in the inviscid inner shock layer stream tube. Comparison to an analysis where the viscous boundary layer is accounted for shows that this inviscid assumption when corrected on the basis of recent experimental data closely predicts the electron concentration value in the body stream tube (20).

Many facets of the proposed shock layer prediction technique need to be more critically evaluated. These include the effect of center body physical scale, the effect of center body cone angle, and the correctness of the thermodynamic-kinetic air model presently being used. Dunn and Lordi's experimental results (23) and the results of the preliminary laser plasma probe study reported herein imply a need to modify the ionized species model. The present prediction study also implies that the influence of the various reactions suggested in the ionized species model may be more directly dependent upon entropy than upon pressure as previously suggested by Eschenroeder (22) and that the nonequilibrium electron temperature characteristics may be specified by an entropy correlation.

The entropy correlation and nozzle-shock layer analog prediction technique offers several worthwhile advantages. It provides a great reduction in the machine computation required in carrying out point-by-point flight trajectory studies to define or estimate important properties such as electron concentration and neutral chemical composition in the shock layer. And it also implies the possibility of using nozzle flows in experimental studies to simulate some of the important phenomena taking place in certain important portions of center body shock layer flow (26). Also see Ref. 30.

The applicability of the shock layer prediction techniques offered is as shown in Figure 9. The $M_\infty = 30$ and 200K ft altitude limits define the regime below which the chemical model is applicable (17) (24). In addition, the maximum altitude limit is further defined by the need for a boundary layer-inviscid shock layer flow situation and thus is a function of centerbody nose radius, r_n (21). The other limit is that below which equilibrium reacting chemistry is no longer achieved at the stagnation point. Therefore, the prediction technique is generally applicable from 200K ft for v_∞ between 22 to 33K ft/sec to $h = 50K$ ft and below for v_∞ between 12K ft/sec to 30K ft/second.

VI. References

1. Bray, K.N.C., "Atomic Recombination in a Hypersonic Wind Tunnel Nozzle", J. of Fluid Mech. 6, 1959.
2. Bray, K.N.C., "Sudden-Freezing Analysis for Nonequilibrium Nozzle Flows", ARS Journal, June 1961.
3. Lordi, J.A. and Mates, R.E., "Nonequilibrium Expansion of High Enthalpy Air Flows", CAL Report No. AD1716-A-3, March 1964.
4. Harris, C.J., "Comment on Nonequilibrium Effects on High-Enthalpy Expansion of Air", AIAA Journal, June 1966.
5. Boyer, D.W., "Nonequilibrium Nozzle Expansion Calculations for the Space Sciences Lab., GE Co.", CAL Order No. 640, July 1962.
6. Eschenroeder, A.Q., Boyer, D.W. and Hall, G., "Exact Solutions for Nonequilibrium Expansions of Air with Coupled Chemical Reactions", CAL Report AF-1413-A-1, May 1961.
7. Harris, C.J., Marston, C. and Warren, W.R., "MHD Generator and Accelerator Experiments in Seeded and Unseeded Air Flows", R66SD50, Sept. 1966.
8. Harney, D.J., "Similarity of Nonequilibrium Expansions in Hypersonic Nozzles", FDM-TM-67-1, May 1967.
9. Ring, L.E. and Johnson, P.W., "Correlation and Prediction of Air Nonequilibrium in Nozzles", AIAA Paper 68-378, 3rd Aero. Testing Conference, April 1968.
10. Harris, C.J. and Warren, W.R., "Correlation of Nonequilibrium Chemical Properties of Expanding Air Flows", GE R64SD92, Dec. 1964.
11. Marston, C.H. and Warren, W.R., "Study of a Continuous Discharge Driver/Non-Reflected/Free Piston Shock Tunnel", GE R68SD1, Jan. 1968, also AIAA Jour. Vol. 7, No. 5, 1969.
12. Dunn, M.G., "Experimental Study of High-Enthalpy Shock Tunnel Flow." AIAA Journal, August 1969
13. Leonard, R.L. and Rose, P.H., "Feasibility of a High Performance Aerodynamic Impulse Facility", AIAA Journal, March 1968.
14. Harris, C.J., "Experimental Identification of Shock Tunnel Flow Regimes", AIAA Journal, Feb. 1969
15. Harris, C.J., Marston, C.H., Rogers, D.A., Mallin, J.R., and Warren, W.R., "A High Density Shock Tunnel Augmented by a Faraday MHD Accelerator", GE R65SD62, Dec. 1965; also 4th Hypervelocity Techniques Symposium Proceedings, Nov. 1965.
16. Gravalos, F.G., Edelfelt, I. and Emmons, H.W., "The Supersonic Flow about a Blunt Body of Revolution for Gases at Chemical Equilibrium", 9th Transactions of the Annual Congress of the International Astronautical Fed., Amsterdam, 1950.
17. Gravalos, F.G., "Analytical Foundations of Aero-thermochemistry", Journal of Applied Math and Physics, Vol. 17, Fasc. 6 (1966).
18. Edsall, R.H., "Calculation of Flow Fields about Blunt Bodies of Revolution Travelling at Escape Velocity", GE 63SD186, July 1962.
19. McMenamin, D. and O'Brien, M., "The Finite Difference Solution of Multicomponent Nonequilibrium Steady Inviscid Stream Tube Flows Using a Novel Stepping Technique", GE 67SD241, April 1967.
20. Harris, C.J., "Correlation of Inviscid Air Nonequilibrium Shock Layer Properties", GE Report R68SD333, Dec. 1968.
21. Probst, R.E., "Shock Wave and Flow Field Development in Hypersonic Re-entry", ARS Journal, Vol. 31, No. 2, Feb. 1961.
22. Eschenroeder, A.Q., "Ionization Nonequilibrium in Expanding Flows", ARS Journal, p. 196-203, Feb. 1961.
23. Dunn, M.G. and Lordi, J.A., "Measurement of $\text{NO}^+ + e^-$ Dissociative Recombination in Expanding Air Flows", CAL A1-2187-A-10, Sept. 1968.
24. Langan, W.T., Cresswell, J.D., and Browne, W.G., "Effects of Ablation Products on Ionization in Hypersonic Wakes", AIAA Journal, Vol. 3, No. 12 Dec. 1965.
25. Warren, W.R. and Harris, C.J., "A Critique of High-Performance Shock Tube Driving Techniques," Aerospace Report TR-0066 (5240-10)-6, Sept. 1969, also Internat. Shock Tube Sympos., Toronto, June, 1969.

26. Harris, C. J., "Experimental Studies on Nose Cooling by Fluid Ejection", GE Technical Brief, RESD, May, 1969.
27. SADJIAN, H., "Dev. of a Laser Plasma Probe for Electron Temperature Meas.", Final Report to AEDC, in preparation.
28. Dunn, M.G. and Lordi, J.A., "Measurement of Electron Temperature and Number Density in Shock Tunnel Flows", AIAA Journal, Nov. 1969
29. Egchenroeder, A.Q., "Entropy Changes in Non-equilibrium Flows," Physics of Fluids, Vol. 6, No. 10, Oct. 1963.
30. Harris, C. J., "Aerospace-Developed Entropy Correlation Applied in Improving Incinerator Design", AAS-AIAA Technology Utilization Paper, 1970.

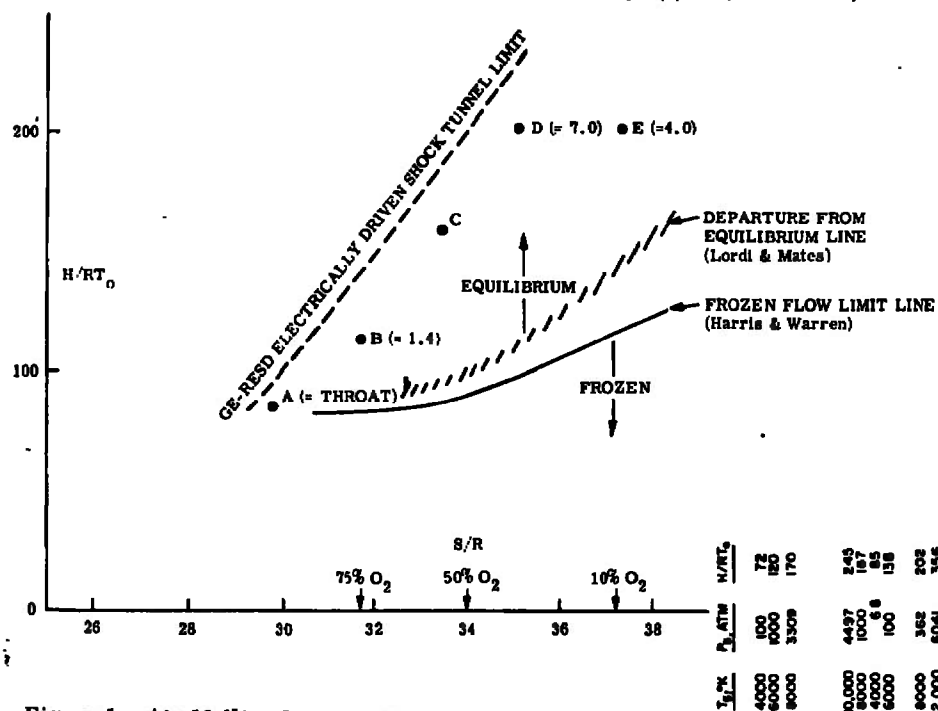


Figure 1. Air Mollier Diagram Showing
Equilibrium and Nonequilibrium Regions

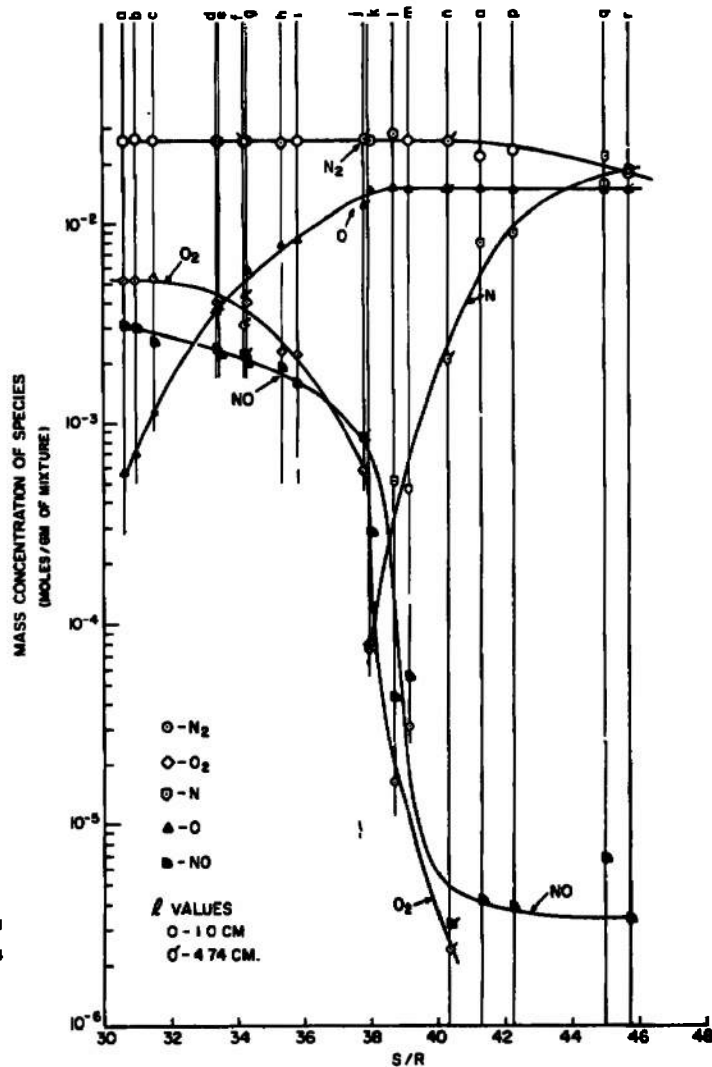


Figure 2. Nonequilibrium Chemical Concentrations vs
Entropy for Expanding High Enthalpy Air Flows
(A/A* = 10³)

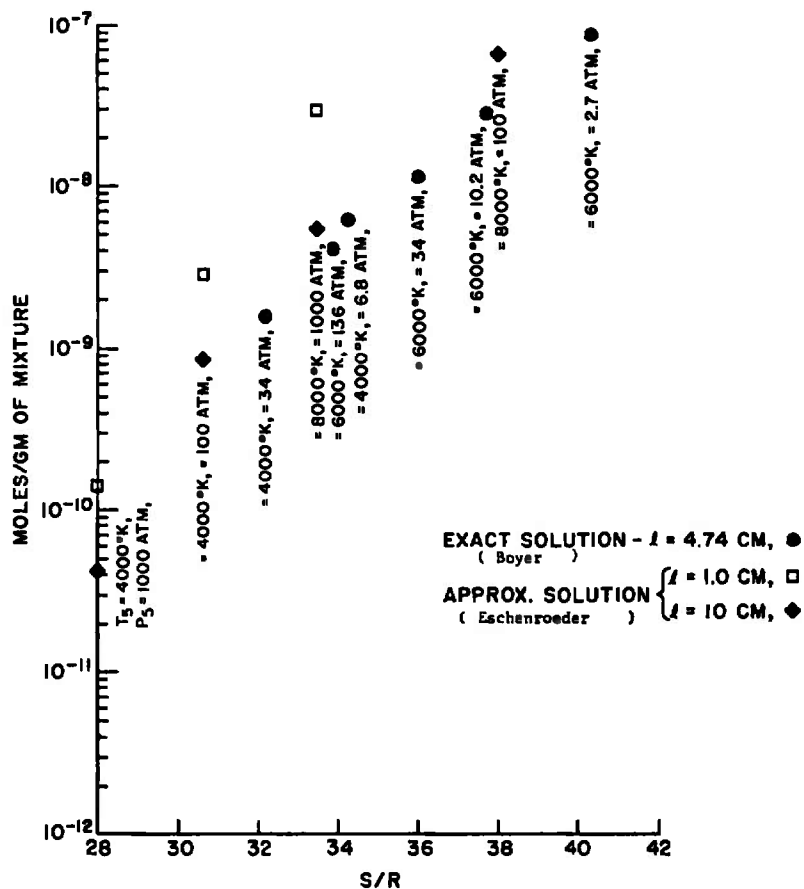
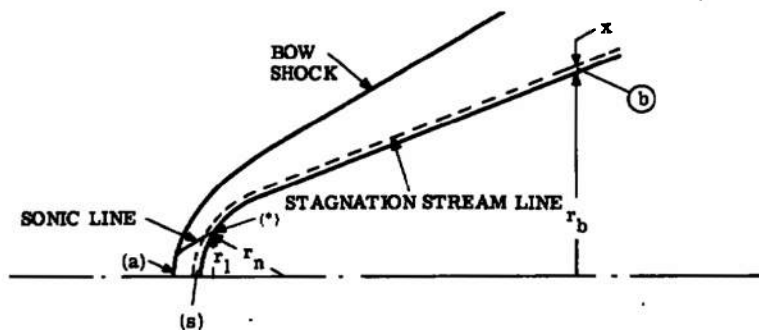
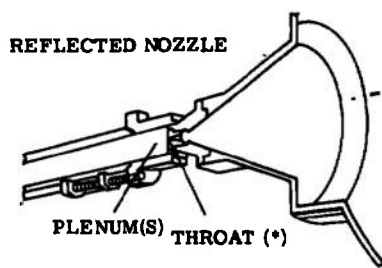


Figure 3. Nonequilibrium Electron Concentration Correlation with Reservoir Entropy at $A/A^* = 10^3$



a. SHOCK LAYER FLOW SITUATION (INVISCID)



b. COMPARABLE NOZZLE SITUATION

Figure 4. Nozzle Flow-Shock Layer Analog

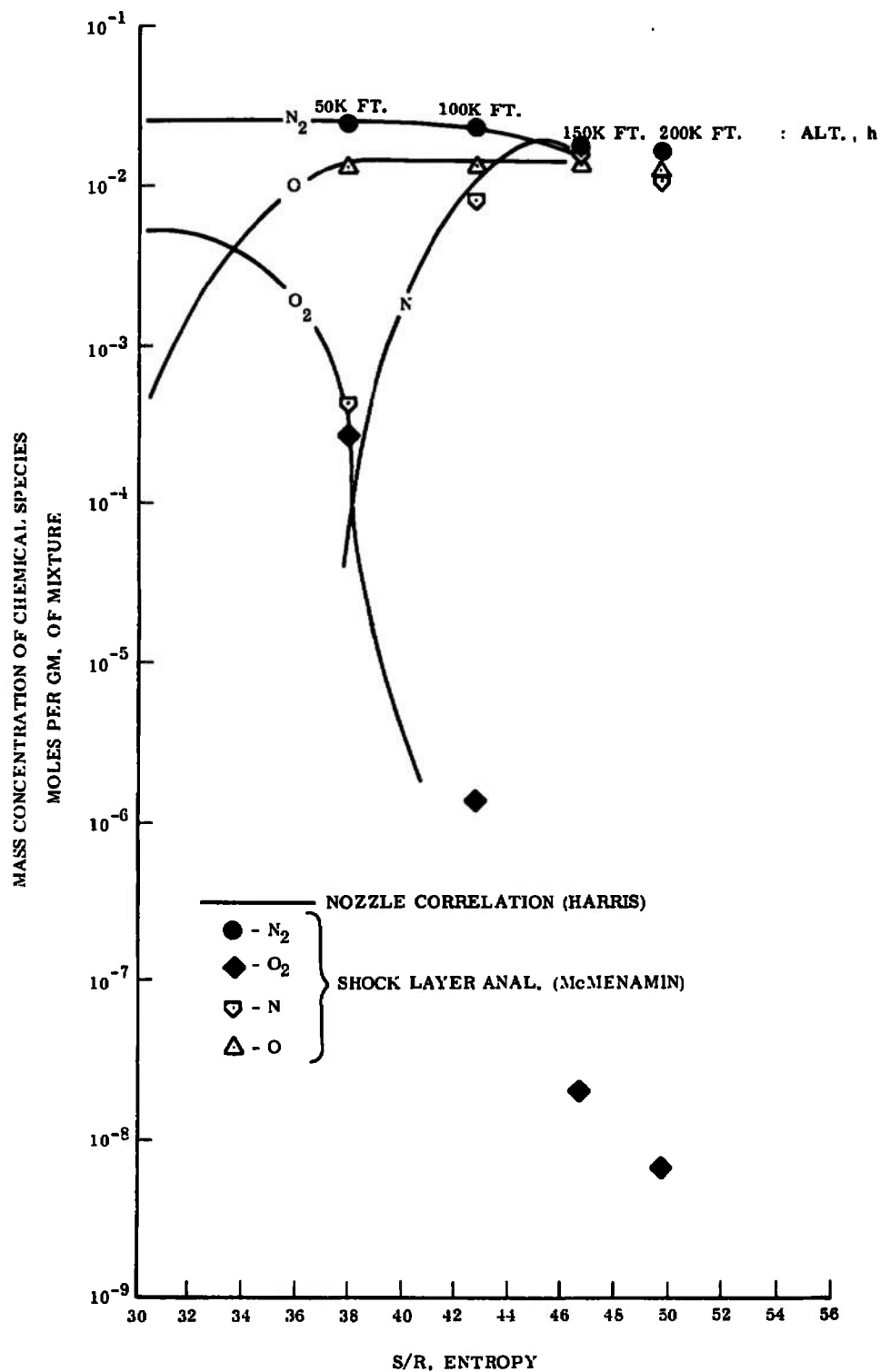


Figure 5. Comparison of Nonequilibrium Shock Layer Chemical Composition to Nonequilibrium Nozzle Correlation

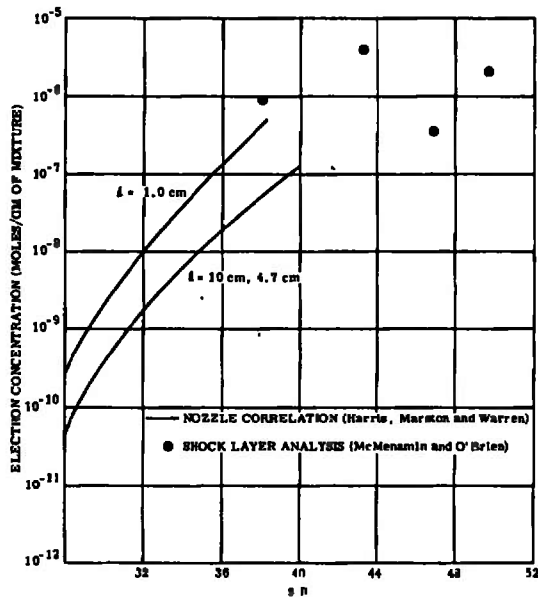


Figure 6. Comparison of Nonequilibrium Shock Layer Electron Concentration to Nonequilibrium Electron Concentration from Nozzle Correlation

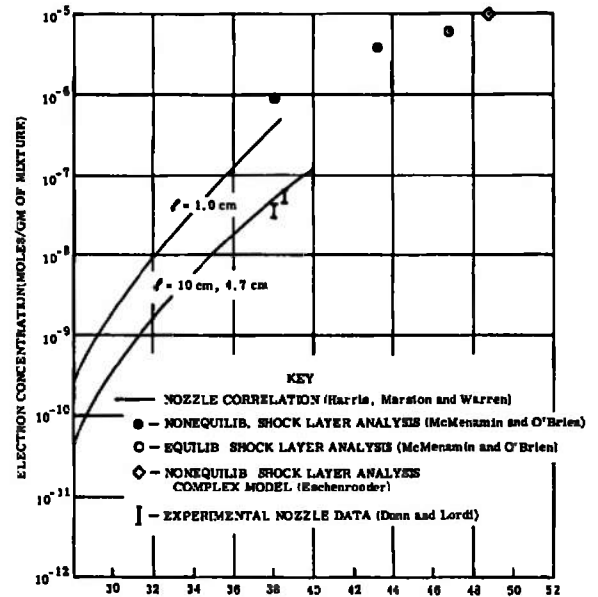


Figure 7. Comparison of Nozzle Correlation to "Adjusted" Shock Layer Calculations and Nozzle Experimental Data

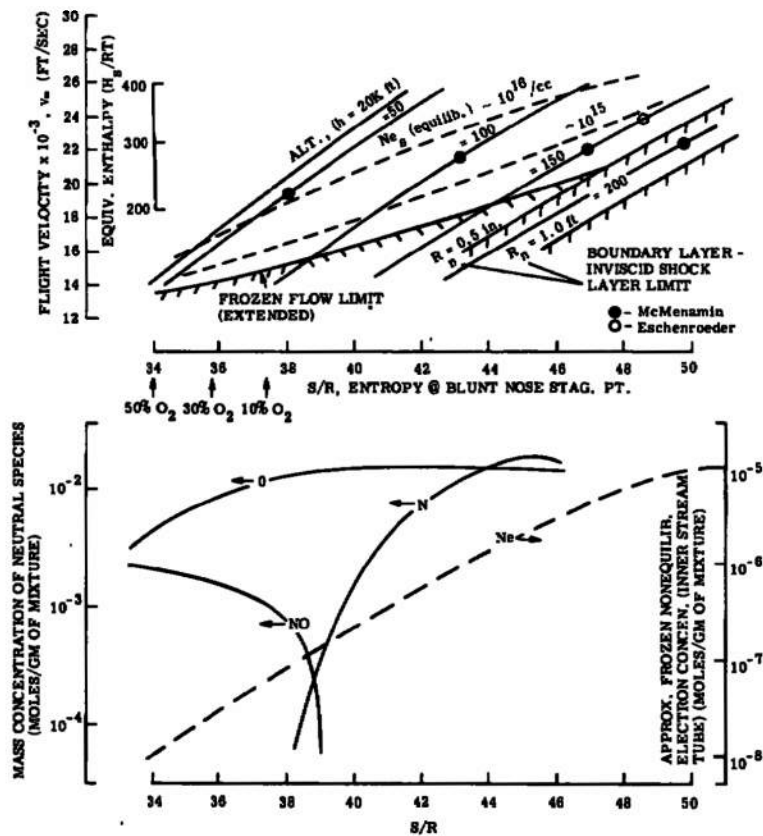


Figure 8. Correlation and Prediction of Shock Layer Properties as a Function of Flight Conditions

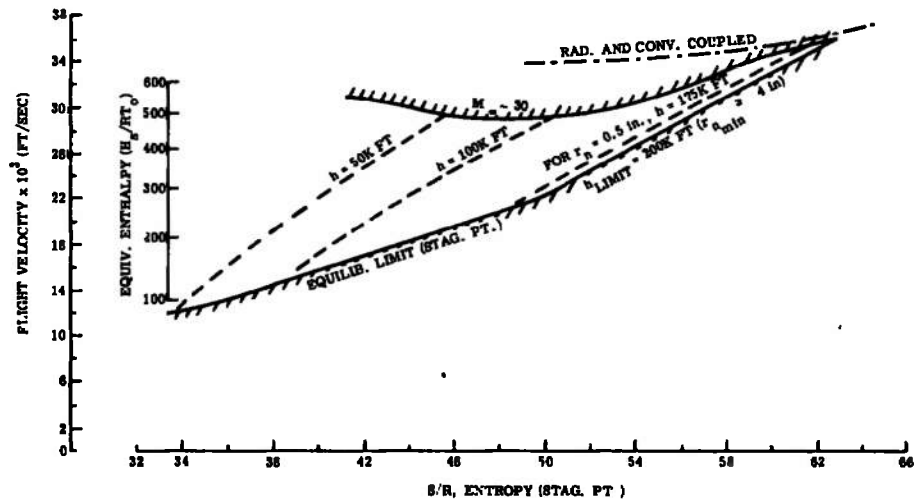


Figure 9. Flight Regime in which Prediction Technique is Applicable

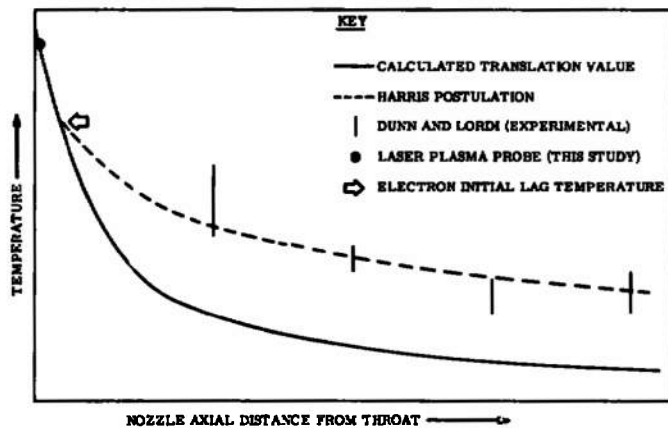


Figure 10. Composite of Electron Temperature Data in Shock Tunnels

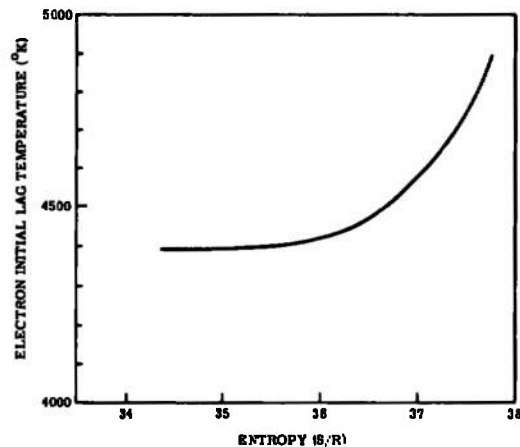


Figure 11. Postulated Conditions at which Electron Temperature and Heavy Particle Temperature Begin to Differ

REFERENCES

1. Dickerman, J. et al, "Optical Spectrometric Measurements of High Temperature", p. 125; the University of Chicago Press, 1961.

UNCLASSIFIED

Security Classification

DOCUMENT CONTROL DATA - R & D

(Security classification of title, body of abstract and indexing annotation must be entered when the overall report is classified)

1. ORIGINATING ACTIVITY (Corporate author) Environmental Sciences Laboratory General Electric Company Philadelphia, Pennsylvania 19101		2a. REPORT SECURITY CLASSIFICATION UNCLASSIFIED
		2b. GROUP N/A
3. REPORT TITLE DEVELOPMENT OF A LASER PROBE FOR ELECTRON TEMPERATURE		
4. DESCRIPTIVE NOTES (Type of report and inclusive dates) Final Report		
5. AUTHOR(S) (First name, middle initial, last name) H. Sadjian and D. A. Rogers		
6. REPORT DATE April 1971	7a. TOTAL NO. OF PAGES 95	7b. NO. OF REFS 1
8a. CONTRACT OR GRANT NO. F40600-68-C-0003	9a. ORIGINATOR'S REPORT NUMBER(S) AEDC-TR-71-69	
b. PROJECT NO. 8952		
c. Program Element 8952	9b. OTHER REPORT NO(S) (Any other numbers that may be assigned this report)	
d. Task 01	N/A	
10. DISTRIBUTION STATEMENT Approved for public release; distribution unlimited.		
11. SUPPLEMENTARY NOTES Available in DDC	12. SPONSORING MILITARY ACTIVITY Arnold Engineering Development Center, Air Force Systems Command, Arnold Air Force Station, Tennessee	

13. ABSTRACT

Thomson scattering radiation has been measured in terms of electron concentration and temperature in a free jet facility and a shock tunnel using a 1/2 joule, Q-switched ruby laser. A detector system is described which attenuates the primary ruby wavelength by 10^5 , discriminates between orthogonal polarization states, analyzes the radiation spectrally and provides a measure of radiation background. The scattering volume was approximately $3 \times 10^{-4} \text{ cm}^3$ for the jet facility and approximately $2 \times 10^{-3} \text{ cm}^3$ for the shock tunnel. A temperature range of 3000 to 8000°K and an electron concentration range 5×10^{14} to $5 \times 10^{15} \text{ cm}^{-3}$ was measured. A unique method of measuring electron temperature is described using a passive system utilizing a retardation plate.

UNCLASSIFIED

Security Classification

14.	KEY WORDS	LINK A		LINK B		LINK C	
		ROLE	WT	ROLE	WT	ROLE	WT
	lasers probes temperature measuring instruments radiation measuring instruments detectors						

UNCLASSIFIED

Security Classification